

Carnegie Mellon University

CARNEGIE INSTITUTE OF TECHNOLOGY

THESIS

SUBMITTED IN PARTIAL FULFILLMENT OF THE REQUIREMENTS

FOR THE DEGREE OF Doctor of Philosophy

TITLE Vibrational Mode Properties of Disordered Solids from High-Performance Atomistic Simulations and Calculations

PRESENTED BY Jason Michael Larkin

ACCEPTED BY THE DEPARTMENT OF

Mechanical Engineering

ADVISOR, MAJOR PROFESSOR

DATE

DEPARTMENT HEAD

DATE

APPROVED BY THE COLLEGE COUNCIL

DEAN

DATE

Vibrational Mode Properties of Disordered Solids from High-Performance Atomistic Simulations and Calculations

Jason M. Larkin

August 2013

*Submitted in partial fulfillment of the requirements
for the degree of Doctor of Philosophy in Mechanical Engineering.*

Carnegie Institute of Technology

Carnegie Mellon University

Pittsburgh, PA 15213

Thesis Committee:

Alan J. H. McGaughey (Chair), Mechanical Engineering

Jonathan A. Malen, Mechanical Engineering

Craig E. Maloney, Civil and Environmental Engineering

Michael Widom, Physics

Copyright © 2013 Jason M. Larkin.

Abstract

Vibrational Mode Properties of Disordered Solids from High-Performance Atomistic Simulations and Calculations

by

Jason Michael Larkin

Chair: Alan McGaughey

The vibrational mode properties of crystalline, alloyed, and amorphous materials are predicted using methods based in molecular dynamics simulations and lattice dynamics calculations. The mode properties allow for an understanding of the nature of thermal transport at the atomic scale not accessible from system-level thermal conductivity prediction.

Thermal transport in crystalline materials is well-understood in terms of the phonon gas model. Disordering a crystal (i.e., by alloying or amorphization) breaks down the applicability of the phonon gas model and additional theoretical formulation is necessary. Typical formulations (e.g., the virtual crystal approximation) begin with perturbation theory, which is only valid for weakly-disordered systems, and lead to simple models whose predictive capabilities are unknown. Predictive methods that explicitly include the disorder (e.g., normal mode decomposition and Allen-Feldman theory) are still under development. Because disordering complicates the theory of thermal transport, each method provides complementary information that must often be integrated together.

To assess the predictive capabilities of theoretical models for thermal transport in disordered materials, Lennard-Jones argon, crystalline and amorphous silicon, carbon nanotubes, and amorphous silica are studied. The theoretical and computational framework for performing the predictive analyses is first presented and discussed. Important assumptions about the nature of thermal transport in disordered materials

are then investigated using perturbative approaches and fully atomistic models where the disorder is included explicitly. The relative contributions of propagating (i.e., phonon-like) and non-propagating vibrational modes are quantified. The predicted mode properties are compared to experimental measurements and phenomenological/empirical models, leading to an understanding of the variation in the system-level thermal conductivity for all the materials. The results provide a theoretical and computational framework for the study of emerging disordered and nanostructured materials.

Acknowledgments

I would like to thank ICES for financial assistance through the Northrop-Grumman fellowship during the 2011-2012 year. I would like to thank the Carnegie Mellon Graduate Student Assembly and the conference travel fund for funding during the 2012 year.

This work was supported by AFOSR award FA95501010098 and by a grant of computer time from the DOD High Performance Computing Modernization Program at the US Army Engineer Research and Development Center.

For technical advice and discussion, I would like to thank Davide Donadio, Joseph Feldman, Jivtesh Garg, Asad Hasan, Ankit Jain, Jonathan Malen, Craig Maloney, Normand Mousseau, Keith Regner, John A. Thomas, Zhiting Tian, and Michael Widom.

And special thanks to all my girls: Jodi, Charlotte, Fiona, Jamie, and especially my mom...

Contents

Abstract	iii
Acknowledgments	v
List of Figures	xiii
List of Tables	xxi
Nomenclature	xxiii
1 Introduction	1
1.1 Motivation	1
1.2 Vibrational Modes: Phonons, Propagons, Diffusons, and Locons	3
1.3 System-level versus Mode-level Predictions	5
1.3.1 System-level Prediction	5
1.3.2 Mode-level Prediction	5
1.3.3 Computational Cost versus Predictive Ability	9
1.4 Overview and Scope	11
2 Vibrational Lifetimes from Molecular Dynamics	13
2.1 Introduction	14
2.2 Phonon Spectral Energy Density	16

2.2.1	As Derived from Normal Mode Coordinates, Φ	16
2.2.2	Formulation in the Time-Domain	17
2.2.3	Alternative Formulation, Φ'	18
2.3	Computational Details	19
2.3.1	Allowed Wavevectors	19
2.3.2	Phonon Lifetimes and Frequencies	20
2.3.3	Thermal Conductivity	21
2.3.4	Computational Cost and Work Flow Optimization	23
2.4	Case Studies	25
2.4.1	Lennard-Jones Argon	25
2.4.2	Stillinger-Weber Silicon	29
2.4.3	Carbon Nanotube	31
2.5	Summary	32
3	Predicting Alloy Vibrational Mode Properties using Lattice Dynamics Calculations, Molecular Dynamics Simulations, and the Virtual Crystal Approximation	35
3.1	Introduction	36
3.2	Theoretical and Computational Framework	38
3.2.1	Thermal Conductivity Prediction	38
3.2.2	Virtual Crystal Approximation	40
3.2.3	Calculation and Simulation Details	42
3.3	Vibrational Mode Properties in Alloys	44
3.3.1	Density of States	44
3.3.2	Dispersion and Group Velocity	45
3.3.3	Lifetimes	48
3.3.3.1	From VC-NMD and Gamma-NMD	48
3.3.3.2	From VC-ALD	52

3.3.4	Diffusivities	55
3.3.5	Discussion	58
3.4	Thermal Conductivity Prediction	60
3.5	SW silicon	64
3.6	Summary	67
4	Thermal Conductivity Accumulation in Amorphous Materials	71
4.1	Introduction	72
4.2	Theoretical Formulation of Vibrational Thermal Conductivity	74
4.3	Calculation Details	77
4.3.1	Sample Preparation	77
4.3.2	Simulation Details	78
4.4	Vibrational Mode Properties	80
4.4.1	Density of States	80
4.4.2	Structure Factor	80
4.4.3	Sound Speed	84
4.4.4	Lifetimes	88
4.4.5	Diffusivities	90
4.5	Thermal Conductivity	96
4.5.1	Bulk	96
4.5.2	Accumulation Function	99
4.6	Summary	102
5	Conclusion	105
5.1	Overview and Contributions	105
5.1.1	Molecular Dynamics-based Methods for Predicting Lifetimes	105
5.1.2	Thermal Transport in Alloys and the High-scatter Limit	106

5.1.3	Mean Free Paths of Propagating Modes in Amorphous Materials	108
5.1.4	Predictive Ability versus Computational Cost	109
5.2	Future Work	111
5.2.1	Large Unit Cell Materials	111
5.2.2	Lifetimes from Larger MD Simulations	113
5.2.2.1	Exact Normal Modes	113
5.2.2.2	Dynamic Structure Factor	113
5.2.3	Comprehensive Package for Thermal Transport Calculations	114
A	Computational Details	115
A.1	Derivation of Phonon Spectral Energy Density, Φ	115
A.2	Interpretation of Φ'	120
A.3	Unit Cell and Supercell Representations	121
A.3.1	Unit Cell Choice	121
A.3.2	Crystal Symmetries	123
A.3.3	Unit Cell Representations using Normal Mode Decomposition	124
A.4	Normal Mode Decomposition using Non-Exact Normal Modes	129
A.5	Effect of Metastability on Normal Mode Decomposition	132
A.6	Finite Simulation-Size Scaling for Thermal Conductivity	134
A.7	Allen-Feldman Theory Calculations	138
A.8	Spectral Density of Disordered Modes	142
A.9	Accumulation Functions in Alloys	144
B	Research using High Performance Computing	147
B.1	Setting Up Computing Environment	147
B.1.1	Hardware and Operating System Choice	147
B.1.2	Terminal, Commands, and Environment Variables	148

B.1.3	Working on Remote Resources	149
B.2	Installing, Writing and Executing Programs	150
B.2.1	Installing Available Packages	150
B.2.2	Available Packages for Thermal Transport Modeling	151
B.2.3	Writing Programs: Compiled versus Interpreted	152
B.2.3.1	Case-study (a): Optimizing Compiled Codes	154
B.2.3.2	Case-study (b): Computational Cost of Interpreted Code . . .	156
B.2.3.3	Case-study (c): Optimizing Interpreted Code	158
B.2.4	Scaling Calculations	159
B.3	Preparing Journal Articles and Thesis	160
B.4	Technical Advice	160
Bibliography		163

List of Figures

1.1	Density of vibrational states for a model of amorphous silicon and classification of vibrational modes (vibrons). Figure is reproduced from Ref. 73.	4
2.1	Raw data and fits for normal mode decomposition in (a) time-, and (b) frequency-domain analysis for two of the [100] phonon modes from the conventional unit cell for $N_0 = 10$ [see Fig. A.1(b)] The inset in (a) shows the convergence of the lifetime according to Eq. (2.7). In (b), the vertical lines denote the frequency predicted from harmonic lattice dynamics calculations.	22
2.2	The phonon spectral energy density (Φ) is plotted as larger blue circles. The proposed alternative expression for the phonon spectral energy density (Φ') is plotted as smaller green points. The wavevector is $(\pi/2a, 0, 0)$. Note that peak broadening at higher temperatures and frequencies above 10 rads/ps can force peaks close in frequency for Φ' to be fit as a single Lorentzian function. Φ does not suffer from this issue since the broadened peaks can be fit individually. . . .	27
2.3	Comparison of the phonon frequencies and lifetimes predicted using Φ (ω and τ) and Φ' (ω' and τ') for LJ argon at temperatures of (a) 5 K, (b) 20 K, and (c) 40 K. The phonon frequencies agree well at all three temperatures, while the phonon lifetimes show large scatter.	28

2.4	Comparison of the phonon frequencies and lifetimes predicted using $\Phi(\omega)$ and τ and $\Phi'(\omega')$ and τ') for SW silicon. The phonon frequencies agree well, while the phonon lifetimes show large scatter.	31
2.5	Comparison of the phonon frequencies and lifetimes predicted using $\Phi(\omega, \tau)$ and $\Phi'(\omega', \tau')$ for a (8,8) CNT modeled using the REBO potential. The phonon frequencies agree well, while the phonon lifetimes show large scatter.	32
3.1	(a) Explicitly disordered alloy supercell of silicon and “heavy” silicon ([100] direction into the page). [146] (b) Equivalent VC supercell with one averaged mass. The sphere size represents increasing mass only, no bond disorder is considered. The 8-atom conventional cubic unit cell is shown in (b).	42
3.2	Vibrational DOS for LJ alloys calculated using the VC approximation and an explicitly disordered supercell (labeled Gamma) for concentrations of (a) 0.05, (b) 0.15, and (c) 0.5. VC and Gamma show similar low-frequency behavior for all concentrations. For increasing concentrations, the frequencies of both VC and Gamma decrease, while the high frequency DOS for Gamma spreads and reaches to a higher maximum frequency because of the explicit disorder. The supercells are of size $N_0 = 12$ (6,912 atoms).	46
3.3	Left and right panels: The structure factor for longitudinal (S_L) and transverse (S_T) polarizations along high-symmetry directions of the mass disordered LJ argon supercells ($N_0 = 10$, $c = 0.05, 0.5$). Center panels: The VC predicted dispersion curves (solid lines) agree well with the locations of the peaks in S_L and S_T (data points). The wavenumber axis in the center panel is normalized by the maximum value of the wavenumber in the given direction.	49

3.4	Lifetimes predicted using VC-NMD and Gamma-NMD from MD simulations of (a) perfect LJ argon and (b),(c),(d) mass-disordered LJ alloys for $N_0 = 10$. ω^{-2} and ω^{-4} scalings are observed at low to mid frequencies. For both VC-NMD and Gamma-NMD, most mode lifetimes are greater than the Ioffe-Regel limit of $2\pi/\omega$. [75] While there is more scatter in the Gamma-NMD data (see Section 3.3.3.1), the lifetime magnitudes and trends agree well, an important consideration when comparing the VC-NMD and VC-ALD lifetimes in Fig. 3.5(a).	53
3.5	(a) Predicted lifetimes using VC-NMD and VC-ALD for LJ argon ($T = 10$ K, $N_0 = 10$, and $c = 0.05$). (b) Mode diffusivities compared to the high-scatter limit, D_{HS} [Eq. (3.18)], and IR limit, D_{IR} [Eq. (3.19)]. VC-NMD and VC-ALD predict a large number of high-frequency modes with $D_{ph} < D_{HS}$. (c) Thermal conductivity frequency spectrum, which peaks at high frequency, in contrast to SW silicon [(Fig. 3.8(c))].	56
3.6	AF theory predictions of disordered mode diffusivities for LJ argon alloy and amorphous phases. The amorphous phase is well-described by a mode-independent diffusivity D_{HS} [Eq. (3.18)]. The system size for the alloy is $N_0 = 10$ (6,912 atoms), and the amorphous phase has 6,912 atoms.	59
3.7	Thermal conductivity predictions for LJ argon and alloys at $T=10$ K using the VC-NMD, VC-ALD, and GK methods. The high-scatter thermal conductivity prediction k_{HS} [Eq. (3.3)] and the high-scatter adjusted VC-NMD* and VC-ALD* are also plotted.	63

3.8	(a) Predicted lifetimes using VC-NMD and VC-ALD for SW silicon ($T = 300$ K, $N_0 = 8$, and $c = 0.05$). (b) Mode diffusivities compared to the high-scatter limit, D_{HS} [Eq. (3.18)], and the IR limit, D_{IR} [Eq. (3.19)]. VC-NMD and VC-ALD predict a large number of high-frequency modes with $D_{ph} < D_{HS}$, as seen in the LJ argon alloys [Fig. 3.5(b)]. (c) Thermal conductivity frequency spectra, which peak at low frequency, in contrast to LJ argon [Fig. 3.5(c)].	66
3.9	Thermal conductivity predictions for SW silicon and alloys at a temperature of 300 K using the VC-ALD and GK methods. The high-scatter thermal conductivity prediction k_{HS} is also plotted. The adjusted VC-ALD* is not shown since it differs by less than one percent compared to VC-ALD.	67
4.1	(a) Small sample of an a-SiO ₂ structure created from a melt-quench technique showing the Si-O tetrahedral bond network. Bond lengths range between 1.6 and 1.8 Å. (b) Small sample of an a-Si structure created by the modified WWW algorithm. Bond lengths range between 2.3 and 2.7 Å. Visualizations using the VESTA package with blue silicon atoms and red oxygen atoms.[146]	79
4.2	Vibrational DOS of a-SiO ₂ and a-Si plotted on a log-log scale. Both models show an ω^2 scaling at low frequency. The DOS for a-Si has two peaks similar to the DOS of the crystalline phase.[121] The DOS for a-SiO ₂ is flat over most of the spectrum, with a high frequency gap that separates the Si-O interactions.[82]	81
4.3	Longitudinal (left panel) and transverse (right panel) structure factors [Eq. (4.12)] for (a) a-SiO ₂ and (b) a-Si. The wavevectors are normalized by $\kappa_{max} = 2\pi/a$, where a is 4.8 (a-SiO ₂) and 5.43 (a-Si) Å, based on the lattice constants of the crystalline phases. [131, 199]	85

4.4	Vibrational mode lifetimes predicted by NMD [Eq. (4.22)] and the structure factors [Eq. (4.15)] for (a) a-SiO ₂ and (b) a-Si. The NMD-predicted lifetimes are larger than the IR limit. The lifetimes predicted from the structure factors fall below the IR limit at high-frequency for a-Si and for all frequencies for a-SiO ₂ . For a-Si, a clear ω^{-2} scaling is observed at low frequencies, while the lifetimes plateau at higher frequencies, over a wider range of frequencies than for a-SiO ₂ , with two peaks corresponding to the peaks in the DOS (Fig. 4.2). The transition from the low-frequency scaling to the plateau region for a-Si occurs near 10^{13} rads/s, which corresponds to where the DOS first peaks in Fig. 4.2.	91
4.5	Vibrational mode diffusivities predicted from NMD [using Eqs. (4.5) and (4.22) with the DOS sound speed from Table 4.1] and the AF theory [Eq. (4.10)]. Also shown are extrapolations based on an ω^{-2} scaling with Eqs. (4.5) and (4.8) for a-SiO ₂ and a-Si, and an additional ω^{-4} scaling for a-Si. For both systems, the diffusivities are larger than the high-scatter limit [Eq. (4.23)] except at high frequencies, where the modes are localized.	94
4.6	(a) Diffuson MFPs predicted from Eqs. (4.7) and (4.24) and velocities (inset) predicted from Eq. (4.25) for a-SiO ₂ . (b) Diffuson MFPs and velocities predicted for a-Si. The majority of MFPs in the mid- to high-frequency range are between the simulation box size L and the bond distance a . The high-scatter MFP is defined as $\Lambda_{HS} = a$. The MFPs and velocities approach zero only at the highest frequencies, which is an indication that the modes are localized.	95
4.7	Thermal conductivities of a-SiO ₂ and a-Si predicted using the GK method and Eq. (4.1). For a-SiO ₂ , the GK-predicted thermal conductivity is size-independent, indicating that there is not an important contribution from propagating modes. For a-Si, there is a clear size dependence, indicating the importance of propagating modes.	98

4.8 (a) Predicted thermal conductivity accumulation function [Eq. (4.27)] for a-SiO ₂ compared with experimental broadband frequency domain reflectance measurements by Regner et al.[15] and thin film measurements from Refs. 70 and 71. The predicted thermal conductivity accumulation demonstrates that the propagating contribution is negligible in our model, which is in accord with the experimental measurements. (b) Predicted thermal conductivity accumulation function for a-Si compared with experimental measurements by Regner et al. and thin films fabricated by sputtering (Expt. A) [51, 65, 66] and chemical vapor deposition (Expt. B). [54, 55, 64, 67] The predicted thermal conductivity accumulation demonstrates that the propagating contribution is significant for a-Si. We note that thermal conductivities as high as 6 W/m-K (not plotted) have been measured for a-Si thin films deposited using hot-wire chemical vapor deposition. [55]	101
A.1 Dispersion curves and full Brillouin zone density of states for a LJ crystal at a temperature of 10 K. (a) [100] and [111] dispersion curves and density of states based on the primitive (i.e., one atom) unit cell. (b) [100] and [111] dispersion curves and density of states based on the conventional (i.e., four atom) unit cell. The harmonic lattice dynamics calculations are performed using a resolution of sixteen wave vectors along the reciprocal lattice vectors of the conventional unit cell. The red and blue dots in (b) are the modes considered in Fig. A.3.	127
A.2 Lennard-Jones lifetimes from a $N_0 = 10$ system at a temperature of 10 K predicted from the NMD method on (a) the primitive and conventional unit cells, and (b) treating the simulation cell as the unit cell (i.e., Gamma-point analysis). All lifetimes extracted from frequency-domain analysis (Φ).	128

A.3	Virtual crystal (a) frequency-domain and (b) time-domain NMD analysis for two modes in LJ alloys with concentrations of 0.05 and 0.5 at a temperature of 10 K. For modes that are not well-approximated by the virtual crystal modes, the lifetime can be approximated using Eq. (2.7), as shown in (d).	131
A.4	(a) Time-domain and (b) frequency domain NMD analysis for two modes in an amorphous LJ solid at a temperature of 10 K.	133
A.5	Lifetimes predicted by normal mode decomposition for an amorphous LJ phase at a temperature of 5 K. The lifetimes for the crystal at a temperature of 10 K are provided for comparison.	133
A.6	Stillinger-Weber silicon thermal conductivities for varying system sizes (N_0) predicted by the VC-NMD, VC-ALD, and GK methods. There is a strong system-size dependence up to $N_0 = 38$ for the VC-ALD and GK methods.	136
A.7	(a) Lifetimes predicted by the VC-ALD method for Stillinger-Weber silicon and alloys for a system size $N_0 = 38$. The mid-range lifetimes scale as $\tau \propto \omega^{-4}$, which leads to a diverging thermal conductivity. (b) Predicted thermal conductivity as a function of frequency, which demonstrates the saturation at low frequency when the lifetimes transition to a scaling $\tau \propto \omega^{-\alpha}$ with $\alpha \leq 2$.	137
A.8	Two-dimensional spatial components of the eigenvectors of the two highest frequency modes in a LJ alloy with $c = 0.5$. Both modes are locons as evidenced by their spatial localization.	139
A.9	The frequency spacing as a function of frequency for (a) the LJ alloy with a concentration of 0.5 and (b) the amorphous phase. For both systems there is a large variation of the frequency spacing, particularly at low and high frequencies where the spacings are up to two order of magnitude larger than the average frequency spacing $\delta\omega_{avg}$.	140

A.10 The AF-predicted total thermal conductivity of LJ alloys and the amorphous phase as a function of the average broadening factor, given in increments of the average frequency spacing.	141
A.11 Mode spectral densities E^L [Eq. (4.13)] for the LJ alloy with a concentration of $c = 0.5$. The wavevector is in the [100] direction (Fig. 3.3). The frequencies are in LJ units.	143
A.12 Thermal conductivity accumulation functions for LJ argon and its alloys.	145
A.13 Thermal conductivity accumulation functions for SW silicon and its alloys.	145

List of Tables

1.1	Comparison of theoretical techniques for predicting vibrational mode properties and thermal conductivity for disordered systems.	8
1.2	Ranking of computational costs for theoretical techniques for predicting vibrational mode properties and thermal conductivity, starting with the least expensive on the left.	10
2.1	Thermal conductivity values in W/m-K predicted using the Φ , Φ' , and Green-Kubo methods. The predictions for Φ and Green-Kubo for the LJ system are in good agreement with those from other atomistic simulation methods [12] while those from Φ' differ and show no consistent behavior. The uncertainties in the predicted thermal conductivities for Φ and Φ' come predominantly from the finite simulation-size scaling procedure (see Ref. [12, 85]), where the phonon properties and thermal conductivity are predicted for increasing system sizes ($N_1 = N_2 = N_3$) to extrapolate a bulk thermal conductivity. For SW silicon and the CNT, the extrapolation procedure is not performed.	30

3.1	Thermal conductivity predictions using the VC-NMD, VC-ALD, and GK methods. For LJ argon alloys, the bulk extrapolation is used for all three methods. For SW silicon alloys, only VC-ALD and GK can be used to extrapolate a bulk thermal conductivity (see Section 3.4). For VC-NMD and GK, the uncertainties are estimated by omitting independent simulations from the ensemble averaging (see Section 4.3). For VC-ALD, the uncertainties are estimated by omitting extrapolation points used for Eq. (3.21).	63
4.1	Longitudinal and transverse sound speeds in m/s estimated from the elastic moduli [Eqs. (4.17) and (4.18)], structure factors [Eq. (4.16)], and DOS [Eq. (4.3)]. The pre-annealed group velocities predicted by the elastic constants are labeled as Moduli*.	87
4.2	Thermal conductivities for bulk a-SiO ₂ and a-Si predicted by the GK method (k_{GK}) and Eqs. (4.1) (k_{vib}), (4.2) (k_{pr}), and (4.9) (k_{AF}). For the non-propagating contribution, classical and quantum specific heats are considered.	99
5.1	Ranking of the predictive ability from low to high (left to right) of theoretical techniques for mode-level and system-level thermal properties for disordered systems.	111
A.1	The unit cell for a face-centered cubic crystal with 256 atoms can be chosen in different ways.	123

Nomenclature

Abbreviations

H system Hamiltonian

NPT constant number of atoms, pressure, and temperature ensemble

NVE constant number of atoms, system volume, and total system energy ensemble

NVT constant number of atoms, system volume, and temperature ensemble

AF Allen-Feldman

ALD anharmonic lattice dynamics

BKS Beest-Kramer-van Santen

BLAS Basic Linear Algebra Subprograms

BTE Boltzmann transport equation

BZ Brillouin zone

CH Callaway-Holland

CNT carbon nanotube

CPU central processing unit

DFT Density Functional Theory

DOS density of states

Gamma analysis at the Gamma point (i.e., $\kappa = 0$)

Gamma-NMD normal mode decomposition performed at the Gamma point (i.e., $\kappa = 0$)

GK Green-Kubo

GULP General Utility Lattice Program

HS high scatter

IR Ioffe-Regel

LAMMPS Large-scale Atomic/Molecular Massively Parallel Simulator

LAPACK Linear Algebra PACkage

LJ Lennard-Jones

LUC large unit cell

MFP mean free path

NMD normal mode decomposition

PCBM Phenyl-C61-butyric acid methyl ester

REBO reactive empirical bond order

SED spectral energy density

SUC small unit cell

SW Stillinger-Weber

VC virtual crystal

VC-ALD anharmonic lattice dynamics performed using the virtual crystal approximation

VC-NMD normal mode decomposition performed using the virtual crystal approximation

VESTA Visualization for Electronic and Structural Analysis

WWW Wooten-Winer-Weaire

Greek Symbols

α cartesian component label

δ	dirac delta function
$\delta_{\omega,avg}$	average frequency spacing
$\Gamma(\kappa_\nu)$	phonon linewidth
$\hat{\kappa}_{VC}$	unit vector of the allowed wavevector of the virtual crystal
κ_{max}	maximum wavevector for structure factor analysis
Λ	propagating mode mean free path
Λ^*	maximum mean free path considered in the thermal conductivity accumulation
Λ_{AF}	diffuson mean free path
Λ_{cut}	mean free path at the cut-off frequency
Λ_{HS}	high scatter mean free path
ν	polarization
ω	frequency
$\omega_0(\kappa_\nu)$	anharmonic phonon frequency
ω_i	frequency of the i th diffuson
ω_{cut}	propagating to non-propagating cut-off frequency
Φ	normal mode spectral energy density
Φ'	proposed alternative spectral energy density
κ	wavevector
κ_{VC}	allowed wavevector of the virtual crystal
$\tau(\kappa_\nu)$	phonon lifetime
τ_0	time integration limit
τ_{eff}	effective vibrational lifetime
$\tau_{p-d}(\kappa_\nu)$	phonon-defect scattering lifetime

$\tau_{p-p}(\kappa)$ phonon-phonon scattering lifetime

Θ spatial and temporal phase factor

Variables

\bar{m}^μ average mass of the μ -th species

$\dot{q}(\kappa; t)$ normal mode coordinate time derivative

\dot{u}_α α -component of the atomic velocity

\mathbf{a}_α lattice vector

\mathbf{b}_α reciprocal lattice vector

$\mathbf{r}_0(b)$ equilibrium position of the b^{th} atom in the unit cell relative to $\mathbf{r}_0(0)$

$\mathbf{r}_0(l)$ equilibrium position vector of the l^{th} unit cell

a lattice constant

b atom in the unit cell label

c alloy concentration

$C(\omega)$ vibrational mode specific heat

c^μ concentration of the μ -th species

$C_0(\kappa)$ mode-dependent Lorentzian constants

c_0 bulk thermal conductivity constant

$C_0(\kappa)$ structure factor peak constant

c_{ph} phonon volumetric specific heat

$cost_{total}$ total computational cost

D number of spatial dimensions

$D_{AF,i}$ mode diffusivity of the i^{th} diffuson

D_{HS} high scatter diffusivity

D_{IR}	Ioffe-Regel diffusivity
$D_{ph,\mathbf{n}}(\kappa_\nu)$	phonon diffusivity in the direction \mathbf{n}
D_{pr}	propagating mode diffusivity
$e(\kappa_\nu^b)_\alpha$	normal mode eigenvector
$E(\kappa_\nu; t)$	normal mode total energy
$E^L(\kappa_{VC}^\nu)$	longitudinal and transverse mode spectra
G	bulk modulus
g_n	disorder strength of the n^{th} order process of the Tamura theory
K	shear modulus
$k(\Lambda)$	thermal conductivity as a function of mean free path
$k(\Lambda^*)$	thermal conductivity accumulation function
$k(N_0)$	system size-dependent thermal conductivity
$k_{\mathbf{n}}$	thermal conductivity in direction \mathbf{n}
k_B	Boltzmann's constant
k_{AF}	diffuson thermal conductivity
k_{bulk}	bulk thermal conductivity
k_{GK}	Green-Kubo predicted thermal conductivity
k_{HS}	high scatter thermal conductivity
$k_{ph,\mathbf{n}}$	phonon thermal conductivity in the direction \mathbf{n}
k_{pr}	propagating component of total vibrational thermal conductivity
k_{vib}	total vibrational thermal conductivity
l	unit cell label
m^μ	mass of the μ -th species

m^i	mass of the i^{th} species
m_b	mass of the b^{th} atom in the unit cell
N	number of unit cells
n	number of atoms in the unit cell
N_a	total number of atoms
N_α	lattice vector integer
n_α	reciprocal lattice vector integer
P	pressure
$q(\kappa_\nu; t)$	normal mode coordinate
$S^{L,T}(\kappa_\omega^{VC})$	longitudinal and transverse structure factor
$S_D(\kappa, \omega)$	displacement structure factor
S_{ij}	heat current operator
T	temperature
t	time
$T(\kappa_\nu; t)$	normal mode kinetic energy
t^*	upper limit of time integration
T_{melt}	melting temperature
u_α	α -component of the atomic displacement from equilibrium
V	system volume
$V(\kappa_\nu; t)$	normal mode potential energy
V_b	volume of the unit cell
v_s	sound speed
v_{AF}	diffusion velocity scale

$v_{s,DOS}$ sound speed extracted from the DOS

$v_{g,n}$ component of the group velocity vector in direction n

Chapter 1

Introduction

1.1 Motivation

Due to their potentially low thermal conductivities, disordered materials (e.g., alloys, amorphous solids, aerogels) are used in applications such a photoelectric energy conversion, thermoelectric energy conversion, and thermally insulating barriers [1, 2, 3, 4, 5, 6, 7, 8, 9, 10, 11]. The focus of this work is on dielectric or semiconducting solids, where the heat is conducted by the atomic vibrational modes. Thermal management engineering (i.e., heat spreaders and thermal insulators) depends critically on accurate predictions of the vibrational mode properties. The mode properties allow for a deeper understanding of the nature of thermal transport at the atomistic scale, which can be used to understand the effects of vibrational scattering mechanisms in bulk and nanostructured materials, which is an area of active research [4, 6, 7, 8, 9, 12, 13, 14, 15].

Thermal transport in ordered (crystalline) materials is well understood in terms of the phonon gas model [16, 17, 18, 19, 20]. Predicting the thermal conductivity requires the properties of the full spectrum of vibrational modes. Theoretical formulations for phonon properties date back to the work of Callaway [21], Holland [22], Klemens [23], and Slack [24]. Their theory derived and/or postulated analytical models for the phonon dispersion and lifetimes (typically based on

low-frequency limits) to be used in a solution of the Boltzmann transport equation (BTE) for predicting thermal conductivity. By fitting the BTE solution to experimental bulk thermal conductivity data, expressions for the lifetimes are obtained. While good fits to the experimental data can be found, this agreement may be due to the numerous fitting parameters and not due to the correctness of the phonon lifetime models [25]. Atomistic techniques, which can predict the properties of individual phonon modes without any assumptions about the dispersion or scattering, are thus required. Newly-developed computational methods based on density functional theory (DFT) calculations can make experimentally-accurate predictions of the phonon properties and thermal conductivity of bulk crystals, whose structures are based on a unit cell with a small number of atoms [26, 27, 28, 29, 30, 31, 32, 33].

Disordering a crystal (i.e., alloying, amorphization) breaks down the phonon gas theory and a new theoretical formulation is necessary. Theoretical formulations for disordered crystals begin with perturbation theory [16, 17, 23, 34, 35], which is only valid for weakly disordered systems (i.e., isotopically disordered crystals) and bases the calculations on a unit cell with a small number of atoms. The study of disordered lattices (i.e., alloys) has become increasingly quantitative as researchers seek lower thermal conductivity thermoelectric materials [4, 6, 8, 9, 36, 37, 38]. Modeling can be experimentally accurate using DFT calculations together with perturbative methods [26, 27, 28, 30, 33, 38, 39]. Because DFT calculations are computationally expensive, they rely on the perturbative methods. The comparison of the perturbative DFT predictions to experiments is only qualitative for some disordered materials, particularly for those with lower thermal conductivities [36, 37, 40, 41]. Thus, there is a need to assess the applicability of the perturbative methods used in DFT calculations for disordered crystals with a range of disorder [32, 36, 37, 40, 41].

Amorphous materials have been well-studied in the literature for their interesting properties such as the Boson peak [42, 43, 44], excess modes [45, 46], and, most relevant to the current study, phonon-like thermal transport [1, 2, 15, 46, 47, 48, 49, 50, 51, 52, 53, 54, 55, 56, 57, 58,

59, 60, 61, 62, 63, 64, 65, 66, 67, 68, 69, 70, 71]. Theoretical modeling of amorphous materials has previously relied on phenomenological models, which have limited predictive capability [1, 2, 24, 49, 69, 72]. The theoretical formulation for the mode properties in amorphous materials has only been recently developed. [47, 48, 73] Like a disordered crystal, an amorphous material has a unit cell with an infinite number of atoms, by definition. However, modeling of amorphous materials is difficult because the topological disorder prohibits the use of perturbative methods. Instead, the disordered material must be modeled explicitly. A finite unit cell can be used to model an amorphous material, but the required size of these models is typically large [48, 52], which limits the use of DFT calculations. As with disordered crystals, modeling of amorphous materials is becoming increasingly quantitative as new experimental techniques for measuring thermal properties reach higher levels of resolution [15, 53, 54, 55, 58, 59, 60, 61, 74]. Thus, there is a need to asses the predictive capabilities of the theoretical models for predicting vibrational mode properties in amorphous materials.

1.2 Vibrational Modes: Phonons, Propagons, Diffusons, and Locons

For a perfect lattice, all vibrational modes are phonon modes, which by definition are delocalized, propagating plane waves [20]. For disordered materials, all vibrational modes are not phonons because there is no translational order. Allen and Feldman define all disordered vibrational modes to be vibrons because they are all bosons and follow Bose-Einstein statistics [73]. The vibrons are propagons, diffusons, or locons. Propagons are propagating and delocalized (i.e., phonon-like) and are typically found in the low-frequency range of the vibrational spectrum [73]. Diffusons are non-propagating and delocalized modes that couple harmonically due to the disorder and spatial delocalization [47]. While diffusons are non-propagating, they can contribute a significant amount to thermal transport [48, 52]. Locons are non-propagating and

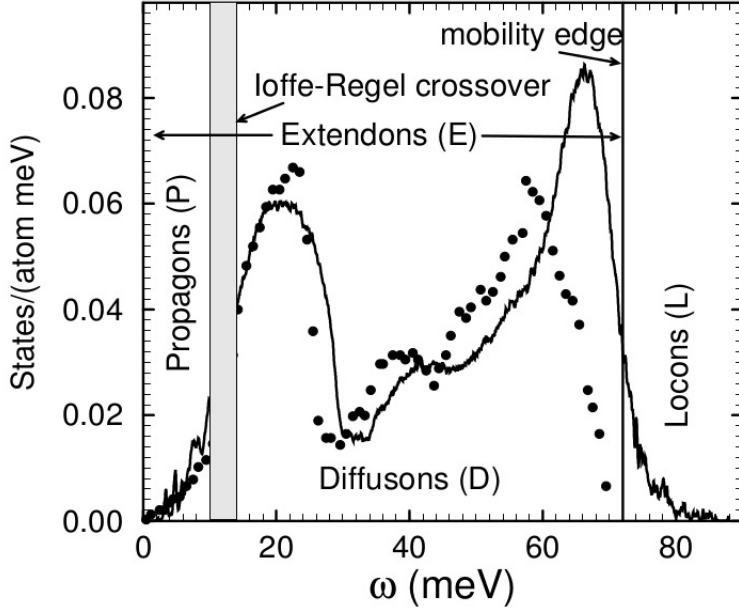


Figure 1.1: Density of vibrational states for a model of amorphous silicon and classification of vibrational modes (vibrons). Figure is reproduced from Ref. 73.

spatially localized modes that not contribute to thermal transport, and are typically found at the high frequency of the vibrational spectrum [47, 73].

The spectrum of vibrons is depicted in Fig. 1.1 for a model of amorphous silicon [73]. The propagons exist at low frequencies below the Ioffe-Regel (IR) limit [75], which is the proposed transition between propagating and non-propagating modes. The IR limit is discussed in Sections 3.3.3 and 4.4.4. Propagons and diffusons are called extendons because they are delocalized. The mobility edge marks the transition from the delocalized diffusons to the localized locons [73].

1.3 System-level versus Mode-level Predictions

1.3.1 System-level Prediction

There are several atomistic methods for predicting the thermal conductivity at the system level. The molecular dynamics (MD)-based direct method predicts the thermal conductivity by a direct application of the Fourier law for heat conduction [12, 76, 77, 78, 79, 80]. While the direct method is conceptually simple, it can be difficult to account for finite-size effects. The Green-Kubo (GK) method can predict the thermal conductivity from equilibrium MD simulations. These equilibrium simulations are often simpler to setup and account for finite-size effects (see Section A.6). The Green-Kubo and direct methods can be applied to crystals, alloys, amorphous solids [12, 29, 36, 62, 77, 77, 81, 82, 83, 84, 85], and is described in detail elsewhere [86, 87]. While the GK and direct methods can take into account the effects of disorder, they predict no mode-level properties of the thermal carriers.

While so-called “quantum corrections” to thermal conductivities predicted from classical MD simulations have been proposed, Turney et al. demonstrate that these corrections are not rigorous and should not be applied [88]. Comparison of MD-predicted thermal conductivities to experimental measurements should therefore be limited to high temperatures, around and above a material’s Debye temperature. The GK method, which is a system-level technique, is important for the present study because it can be used to validate the mode-level techniques that are the focus. The capabilities of the GK method are summarized in Table 1.1. It is important to note that the theoretical formulation of the GK method prohibits its use with DFT calculations, where the per atom potential energies cannot be rigorously defined.[89]

1.3.2 Mode-level Prediction

While the total thermal conductivity is typically the quantity of interest for modeling and engineering analysis, the mode-level properties can be just as important. The mode-level properties

allow for a deeper understanding of the total thermal conductivity. The mode-level properties are used to understand the difference between predictions for alloys in Chapter 3 and amorphous materials in Chapter 4.

The Callaway-Holland (CH) theory, which is based on the work of Callaway [21], Holland [22], Klemens [23], and Slack [24], uses analytical models for phonon dispersion and lifetimes. These analytical models are often empirically fit to experimental results, which limits the predictive capability of the CH theory. While the CH theory can calculate mode properties from the analytical models, it is unclear how accurate these properties are.[25]

There are several methods that can predict the mode-level vibrational properties. Anharmonic lattice dynamics (ALD) calculations [12, 29], based on perturbation theory [16, 18], can be used along with phonon-defect scattering perturbation theory to predict the mode properties and thermal conductivity of mass and/or bond disordered lattices (see Section 3.3.3.2) [23, 35, 90, 91]. However, ALD is a perturbative method that is valid at low temperatures where 3-phonon processes dominate [12, 16, 17]. Quantum or classical statistics can be used with the ALD method. Because the ALD method is based on a unit cell and disorder is included as a perturbation, the mode properties predicted are for phonons. One of the objectives of this work is to investigate if the phonon properties predicted by the ALD method are consistent with the properties of propagons in a fully disordered system (see Chapter 3).

The inputs to the ALD method are the harmonic and anharmonic force constants from the interatomic interactions, which can be obtained from empirical interatomic potentials or DFT calculations [12, 92]. Because the ALD method is computationally inexpensive, it can be used with computationally expensive DFT calculations to predict thermal conductivities that are experimentally accurate [26, 27, 28, 30, 30, 33, 38, 38, 39]. However, most studies using ALD and DFT have been limited to disordered lattices (i.e., alloys) whose thermal conductivities are large and dominated by low-frequency propagons [26, 27, 28, 30, 30, 33, 39]. Because no comprehensive study has been performed on a range of materials, it is unclear what limitations exist for

using the ALD and phonon-defect perturbative method [32, 32, 36, 37, 40, 41]. The limitations of the ALD and phonon-defect perturbative method is investigated in Chapter 3.

The key to explicitly incorporating the effects of disorder is to use large disordered supercells, or a unit cell with a large number of atoms. The use of computationally inexpensive empirical potentials allows for calculations to be performed on a large number of atoms, up to 10^5 – 10^6 [62, 83, 84, 85]. The Allen-Feldman (AF) theory computes the contribution of diffusons to thermal conductivity from large disordered supercells [47]. The AF theory calculations are based on harmonic lattice dynamics that rely on the system disorder to couple modes thermally [47, 48, 52]. However, because the AF theory is harmonic, it is not suited to studying the low-frequency propagons in disordered materials [48], particularly for disordered lattices where the harmonic theory predicts Rayleigh scattering, which causes a divergent thermal conductivity with increasing system size [93, 94, 95]. The AF theory can use quantum or classical expressions for the specific heat. While the AF theory should be limited to low temperatures where the harmonic approximation is valid, anharmonic effects have been shown to be small for disordered solids such as amorphous silicon [48].

The normal mode decomposition (NMD) method can be used to predict the lifetime of all vibrons from MD simulations [12, 62, 81, 83, 84, 85, 96, 97, 98, 99, 100, 101, 102, 103, 104, 105, 106]. While this method can only predict the mode lifetimes, these can be used with other predictive methods and assumptions to predict the thermal conductivity (see Sections 3.3.4 and 4.4.5). Because the lifetimes predicted by NMD are obtained from MD simulations, they should be used in a classical limit [88]. The thermal conductivity predicted by NMD begins to deviate from GK and direct-method prediction near about half the melting temperature for Lennard-Jones argon [12].

Because of the theoretical limitations of the methods discussed above, no one method is sufficient for predicting the mode properties of all vibrons in a given disordered material. The theoretical methods are summarized and compared in Table 1.1. The methods in Table 1.1 are

Table 1.1: Comparison of theoretical techniques for predicting vibrational mode properties and thermal conductivity for disordered systems.

	CH Theory	ALD	AF Theory	NMD	GK
Description	Empirical	Predictive	Predictive	Predictive	Predictive
Input	Fitted Models	Force constants (empirical potential or DFT)	Force constants (empirical potential or DFT)	Forces and Force Constants (empirical potential or DFT)	Forces (empirical potential)
Disorder	As additional perturbation	As additional perturbation	Naturally included	Naturally included	Naturally included
Statistics	Bose-Einstein or Boltzmann	Bose-Einstein or Boltzmann	Bose-Einstein or Boltzmann	Boltzmann	Boltzmann
Temperature	All	Low	All	Mid-range	All
Modes	Phonons (Vibrongs?)	Phonons (Vibrongs?)	Diffusons	Phonons and Vibrongs	N/A

ranked in the order of their thermal conductivity predictive capability based on prior work in the literature, starting with the least predictive on the left. For example, the CH theory relies completely on empirical fitting, while the GK method can predict the thermal conductivity of some materials in any phase (crystalline, amorphous, liquid) [87]. In Chapter 5, the predictive capabilities are re-ranked in Table 5.1 based on their ability to predict the mode properties in disordered systems from the results in this work.

1.3.3 Computational Cost versus Predictive Ability

The computational costs of the methods discussed in Sections 1.3.1 and 1.3.2 are given in Table 1.2. In most cases, the computational cost of a method is known *a priori* and should be considered before any analysis is performed. The computational costs for these methods can be represented by the total number of atoms, N_a , that are being simulated. For ordered and disordered systems, the total number of atoms can be related to the number of atoms in the unit cell, n , and the number of unit cells, N ($N = 1$ for a disordered system), which gives $N_a = Nn$ (see Section 2.3.1).

One of the goals of this work is to thoroughly asses the predictive abilities of these methods in relation to their computational costs. For example, The NMD method can predict the mode lifetimes for the vibrational modes in ordered and disordered systems (i.e., phonons and vibrons), making its predictive ability high [12, 62, 81, 83, 84, 85, 99, 100, 101, 102, 103, 104, 105, 106]. However, the explicit use of disorder makes the NMD method's computational cost high (see Section 2.3.4), making it particularly challenging to use with DFT calculations [29, 36, 107, 108, 109, 110].

For the AF Theory and NMD method, the major computational cost is the eigenvalue solution of the dynamical matrix (see Sections 3.3.1 and 4.3.2), which scales poorly in both CPU and memory costs. For ALD, N_a determines the resolution of the Brillouin zone (BZ) sampling (see Section 2.3.1 and Ref. 111). Some systems (such as the silicon alloys studied in Section 3.5) require a fine sampling of the BZ, which increases the ALD computational costs. Using large systems can be avoided by following the extrapolation procedure which is discussed in Appendix A.6. Efficient MD codes like LAMMPS scale linearly with the number of atoms in the system which makes the GK method (see Section 3.4) computationally-inexpensive.

The computational costs for each method are ranked in Table 1.2 starting with least expensive on the left. The rankings do not take into account the coefficients of the computational scalings. For example, to perform NMD on a system of 6912 atoms in less than 24 hours may take 100

Table 1.2: Ranking of computational costs for theoretical techniques for predicting vibrational mode properties and thermal conductivity, starting with the least expensive on the left.

	CH Theory	AF Theory	NMD	GK	ALD
Computational Cost					
CPU	Minimal	High	High	High	High
Memory	Minimal	High	High	Low	Low
Maximum N_a	N/A	6912	6912	800000	8
Maximum number of Modes	N/A	20736	20736	N/A	592704
Computational Scaling					
CPU	Minimal	$(Nn)^3$	$(Nn)^2$	$(Nn)^1$	N^2n^4
Memory	Minimal	$(Nn)^2$	$(Nn)^2$	$(Nn)^1$	Nn^2

central processing units (CPUs). The same number of CPUs are required to perform the GK method on a system of 100000 atoms in the same amount of time. Coefficients of the computational scalings would take into account the difference in computational cost of classical pair potentials versus multi-body potentials, for example. Thus, the ranking in Table 1.2 is to be used as a rough guideline. The maximum system sizes are those achieved in this work.

The GK method, which scales most efficiently in both memory and CPU cost, has the most potential to simulate systems with increased N_a , but does not predict the properties of any modes. While the properties for a large number of modes can be predicted the ALD method, no explicit atomic dynamics are simulated and the calculation is based on a small number of atoms. The poor scaling of the computational cost with system size for the ALD method prohibits increasing the system size significantly. The same is true for the AF and NMD methods. Suggestions are given in Section 5.2.2 for increasing the system sizes for the AF and NMD methods, as well as suggestion for other MD-based methods.

1.4 Overview and Scope

The objective of this work is to develop a theoretical and computational framework for predicting the vibrational mode properties in a range of disordered materials using atomistic techniques. This objectives will be achieved through the use of four predictive methods: MD-based GK, MD-based NMD, ALD, AF Theory (see Section 1.3). The analysis is performed on atomistic models of a wide-range of ordered and disordered systems. Emphasis is placed on investigating each material with as many of the four methods as possible to analyze the thermal properties self-consistently. The outline is as follows:

In Chapter 2, two MD-based methods for predicting vibrational mode properties are compared and evaluated. The vibrational mode properties and thermal conductivities are predicted for models of three materials: argon, silicon, and a carbon nanotunbe. Theoretical derivations are presented and the computational framework for performing the analysis is discussed. Recommendations are made based on the comparison of the two methods for future work using MD-based methods (see Section 5.2.2.2).

In Chapter 3, the virtual crystal approximation for predicting the vibrational properties of alloys is investigated. Two model systems, Lennard-Jones argon and Stillinger-Weber silicon, are used to perform the analysis. The analysis is performed using molecular dynamics simulations and lattice dynamics calculations. The vibrational mode properties in crystalline, alloyed, and amorphous materials are studied using fully atomistic models. Mode frequencies and lifetimes are first calculated by treating the disorder explicitly and under the virtual crystal approximation. The two model systems have different vibrational mode spectra, which plays an important role in determining the applicability of the virtual crystal approximation. The mode properties are then used to predict thermal conductivity, and common phenomenological limits are used to interpret the results. Important connections between disordered lattices and amorphous materials are made through a comparison of their mode properties, which solidifies the modeling framework for studying the propagating and non-propagating vibrational modes in disordered systems.

In Chapter 4, the properties of the propagating and non-propagating vibrational modes in amorphous silica and silicon are predicted using realistic atomistic models. The calculations are performed using molecular dynamics simulations, lattice dynamics calculations. Using the mode properties, the thermal conductivity accumulation functions are predicted and compared with recent experimental measurements by Regner et al.[15] and thin film thermal conductivity measurements. The two amorphous materials studied have significantly different contributions from propagating and non-propagating vibrational modes, which is evident in their accumulation functions and the comparison of the predictions to experimental measurements.

In Chapter 5, the major contributions of the work are presented and suggestions for future study are discussed. The results presented in this work provide a theoretical and computational framework for the study of emerging disordered and nanoscaled systems.

Chapter 2

Vibrational Lifetimes from Molecular Dynamics

Two frequency-domain methods for predicting phonon frequencies and lifetimes using the phonon spectral energy density are described. Both methods draw input from molecular dynamics simulations and lattice dynamics calculations, but differ in the form of the phonon spectral energy density. One phonon spectral energy density expression (referred to as Φ) can be formally derived from lattice dynamics theory. A similar approach in the time domain has been validated [12]. The other phonon spectral energy density expression (referred to as Φ') has been proposed [112] but not validated. The expressions for Φ and Φ' are presented and then applied to predict the phonon properties and thermal conductivities of three systems: Lennard-Jones argon, Stillinger-Weber silicon, and a carbon nanotube modeled using the reactive empirical bond order potential. Φ' does not capture the total phonon spectral energy density predicted by Φ and therefore cannot correctly predict the phonon lifetimes or thermal conductivity. Its use in future work is discouraged and we recommend the use of Φ .

2.1 Introduction

Phonons are the dominant carriers of thermal energy in dielectric and semiconducting crystals [16, 17, 18, 19, 113, 114]. While substantial effort has been devoted to developing theories of phonon transport, the current understanding is incomplete, even in bulk materials. For example, which phonon modes dominate thermal energy transport and the importance of interactions involving four or more phonons are still being investigated [17, 18, 26, 29, 113]. The situation becomes more complicated in nanostructures, where the phonons also interact with free surfaces and interfaces [13, 70, 77, 78, 79, 85, 115, 116, 117, 118, 119, 120, 121].

Analytical models of thermal transport, such as the Debye model, are limited by the necessary approximations and assumptions [13, 21, 22]. With the Green-Kubo or non-equilibrium direct methods, molecular dynamics (MD) simulations can be used to predict thermal conductivity, but only in a classical (i.e., high-temperature) framework [12, 29, 77, 81, 99, 122, 123]. Because the analysis in these two MD-based methods is performed at the system level, no information about the phonons is obtained. Phonon specific heats, group velocities, and lifetimes are the required inputs for predicting thermal conductivity at the phonon-mode-level using Boltzmann transport equation-based models [12, 13, 29, 81, 85, 99, 123]. These phonon properties can be predicted using harmonic and anharmonic lattice dynamics calculations [12, 17, 19, 88, 99, 124], where quantum statistical effects can be naturally included. Anharmonic lattice dynamics calculations are limited to three-phonon scattering events, however, and are thus only valid at low temperatures [12, 17, 18, 29].

At high temperature, four-phonon and higher-order processes become important to thermal transport [12, 17, 18, 29]. All orders of phonon processes are present in a MD simulation as the positions and momenta of the atoms are evolved using the full anharmonicity of the interatomic interactions [29, 81]. Phonon properties can be predicted from a MD simulation using normal mode analysis in the time domain [12, 81, 85, 99, 101, 103]. In Section 2.2.1, we will describe how this approach can be performed in the frequency-domain using the phonon spectral energy

density (SED, referred to as Φ). An alternative expression for the phonon SED (referred to as Φ'), was recently proposed but has not been rigorously tested [112, 125, 126]. Φ' was first used to predict the phonon dispersion curves of carbon nanotubes (CNTs) [125]. Thomas et al. used Φ' to predict the phonon lifetimes and thermal conductivity of isolated and water-filled CNTs, obtaining good agreement with other atomistic predictions [112]. The phonon lifetime reductions speculated for water-filled CNTs [112] and CNTs on SiO_2 substrates [127] suggest that Φ' captures phonon physics at least qualitatively. The phonon lifetimes and thermal conductivity for PbTe [128] and Half Heusler alloys [36] have also been predicted using Φ' . De Koker predicted the phonon lifetimes and thermal conductivity for MgO using an expression similar to Φ' (but different than Φ) [107]. Another recent atomistic study using Stillinger-Weber silicon predicted phonon lifetimes using both Φ and Φ' , but a detailed comparison of the predictions between the two was not performed [129].

The objective of this work is to assess the validity of Φ' as a phonon SED by comparing the phonon properties it predicts to those predicted by Φ . In Section 2.2.1, we present the correct phonon SED (Φ), which requires the phonon mode eigenvectors. The expression for Φ is well-defined theoretically and has been tested and validated in previous studies in the time domain [12, 99]. In Section 2.2.3, we present the proposed alternative expression for the phonon SED, Φ' , which does not require the phonon mode eigenvector [112]. Phonon frequencies, lifetimes, and thermal conductivities are then predicted and compared using Φ and Φ' for three test systems: Lennard-Jones (LJ) argon [130] in Section 2.4.1, Stillinger-Weber (SW) silicon [131] in Section 2.4.2, and an (8,8) CNT modeled with the reactive empirical bond order (REBO) potential [132] in Section 2.4.3. While Φ' is found to accurately predict the phonon frequencies, we find that it does not correctly predict the phonon lifetimes because it does not capture the total phonon spectral energy density.

2.2 Phonon Spectral Energy Density

2.2.1 As Derived from Normal Mode Coordinates, Φ

The correct expression for the phonon SED, Φ , can be derived from the formulation of anharmonic lattice dynamics theory [16, 17, 18, 19]. As shown in Appendix A.1, the phonon SED at wavevector κ is a function of frequency, ω , and is given by

$$\Phi(\kappa, \omega) = \sum_{\nu}^{3n} C_0(\nu) \frac{\Gamma(\nu) / \pi}{[\omega_0(\nu) - \omega]^2 + \Gamma^2(\nu)}, \quad (2.1)$$

which is a superposition of $3n$ Lorentzian functions with centers at $\omega_0(\nu)$ and linewidths $\Gamma(\nu)$ (one for each polarization, ν). The $C_0(\nu)$ terms are mode-dependent constants. For simplicity, we refer to $\Phi(\kappa, \omega)$ as Φ . The kinetic energy normal mode coordinate, $\dot{q}(\nu; t)$, is [19]

$$\dot{q}(\nu; t) = \sum_{\alpha, b, l}^{3, n, N} \sqrt{\frac{m_b}{N}} \dot{u}_{\alpha}(b; t) e^*(\nu \alpha) \exp[i\kappa \cdot \mathbf{r}_0(l)], \quad (2.2)$$

where $e(\nu \alpha)$ are the components of the time-independent phonon mode eigenvector (see Section 2.3.2), n is the number of atoms in the unit cell, m_b is the mass of the b^{th} atom in the unit cell and $\mathbf{r}_0(l)$ is the equilibrium position vector of the l^{th} unit cell. There are N total unit cells and $\dot{u}_{\alpha}(b; t)$ is the α -component of the velocity of the b^{th} atom in the l^{th} unit cell at time t .

Given a set of atomic velocities from MD simulation and the phonon mode eigenvector, Φ can be calculated using

$$\Phi(\kappa, \omega) = 2 \sum_{\nu}^{3n} T(\nu; \omega) = 2 \sum_{\nu}^{3n} \lim_{\tau_0 \rightarrow \infty} \frac{1}{2\tau_0} \left| \frac{1}{\sqrt{2\pi}} \int_0^{\tau_0} \dot{q}(\nu; t) \exp(-i\omega t) dt \right|^2, \quad (2.3)$$

and then fit using Equation (2.1) to extract the phonon properties $\omega_0(\nu)$ and $\Gamma(\nu)$. The phonon lifetime, $\tau(\nu)$, is defined as $1/[2\Gamma(\nu)]$. In practice, τ_0 should be much larger than the longest phonon lifetime and the continuous fourier transform in Equation (2.3) is performed using a

discrete fast fourier transform (see Section 2.4.1, 2.4.2 and 2.4.3).

2.2.2 Formulation in the Time-Domain

Previous work using normal mode analysis has represented the phonon energy in the time domain [12, 81, 85, 99, 101, 103], while Φ is a representation of the phonon energy in the frequency domain. The time- and frequency-domain approaches are mathematically equivalent by use of the Wiener-Khinchin theorem [36, 133], which applied to Eq. (2.1) gives

$$\frac{T(\boldsymbol{\kappa}; t) T(\boldsymbol{\kappa}; 0)}{T(\boldsymbol{\kappa}; 0) T(\boldsymbol{\kappa}; 0)} = \cos^2[\omega_a(\boldsymbol{\kappa}) t] \exp[-2\Gamma(\boldsymbol{\kappa}) t]. \quad (2.4)$$

The frequency-domain approach using the normal mode kinetic energy has the advantage of predicting both the phonon lifetime and frequency by fitting a simpler function than is required in the time-domain approach.

The time-domain approach can be simplified by calculating the normal mode coordinate, $q(\boldsymbol{\kappa}; t)$,

$$q(\boldsymbol{\kappa}; t) = \sum_{b,l} \left(\frac{m_b}{N} \right)^{1/2} \exp[i\boldsymbol{\kappa} \cdot \mathbf{r}_0(l)] \mathbf{e}_b^*(\boldsymbol{\kappa}) \cdot \mathbf{u}(l; t), \quad (2.5)$$

and using it along with Eq. (2.2) to calculate the total normal mode energy, $E(\boldsymbol{\kappa}; t)$ [Eq. (A.6)].

The autocorrelation of the total normal mode energy is

$$\frac{E(\boldsymbol{\kappa}; t) E(\boldsymbol{\kappa}; 0)}{E(\boldsymbol{\kappa}; 0) E(\boldsymbol{\kappa}; 0)} = \exp[-2\Gamma(\boldsymbol{\kappa}) t], \quad (2.6)$$

Thus, one can find the lifetime by fitting the normalized autocorrelation of the mode total energy to an exponential decay. Instead of fitting an exponential function, the lifetime can be approxi-

mated as

$$\tau(\kappa) = \int_0^\infty \frac{E(\kappa; t)}{E(\kappa; 0)} \frac{E(\kappa; 0)}{E(\kappa; 0)} dt, \quad (2.7)$$

an expression that is beneficial when studying disordered systems (see Section 3.3.3.1 and Appendix A.4).

2.2.3 Alternative Formulation, Φ'

We now seek to motivate the expression Φ' that was proposed in previous studies, but has not been validated [112, 125, 126]. Thomas et al. [112] define

$$\Phi'(\kappa, \omega) = \frac{1}{4\pi\tau_0} \sum_{\alpha}^3 \sum_b^n \frac{m_b}{N} \left| \sum_l^N \int_0^{\tau_0} \dot{u}_{\alpha}(l; t) \exp[\Theta] dt \right|^2, \quad (2.8)$$

where $\Theta \equiv i[\kappa \cdot \mathbf{r}_0(l) - \omega t]$. Thomas et al. [112] claim that Φ' represents the phonon SED. As seen in Eqs. (2.5) and (2.2), the phonon mode eigenvectors are necessary to properly map between the atomic velocities and the normal mode coordinates. This need for the eigenvectors is the essential difference between the expressions for Φ and Φ' . The potential advantage of Φ' is that other than the wavevectors, which can be determined from the crystal structure, no phonon properties need to be known *a priori*. However, to identify the degenerate modes in Φ' , the phonon frequencies are necessary (see Section 2.3.2). Since Φ' does not require the phonon mode eigenvector, it can (in principle) be used to study disordered systems or perturbed crystalline systems (e.g. dilute alloys [36], water-filled CNTs [112], and CNTs on substrates [127]). Despite its use in previous studies, Φ' has not been rigorously validated. The interpretation of Eq. (2.8) is investigated in Appendix A.2. For simplicity, we refer to $\Phi'(\kappa, \omega)$ as Φ' . Given a set of atomic velocities, Thomas et al. extract the phonon properties $\omega_0(\kappa)$ and $\tau(\kappa)$ from Equation (2.8) by fitting Φ' for a given wavevector to a superposition of Lorentzian functions.

2.3 Computational Details

2.3.1 Allowed Wavevectors

Now that we have presented the two expressions for the phonon SED, we will provide the computational details of how they can be evaluated and used to predict phonon properties. The SED is defined for the allowed wavevectors of a crystal, which can be specified from the crystal structure's Bravais lattice, its basis (i.e., unit cell), and the size of the computational domain. A D -dimensional Bravais lattice is a collection of points with positions

$$\mathbf{r}_0(l) = \sum_{\alpha}^D N_{\alpha} \mathbf{a}_{\alpha}, \quad (2.9)$$

where \mathbf{a}_{α} are the lattice vectors and N_{α} is an integer [19]. The unit cell is the building block of the crystal and is placed on the points defined by the Bravais lattice. The equilibrium position of any atom in the crystal can be described by

$$\mathbf{r}_0(b) = \mathbf{r}_0(0) + \mathbf{r}_0(b), \quad (2.10)$$

where $\mathbf{r}_0(b)$ is the equilibrium position of the b^{th} atom in the unit cell relative to $\mathbf{r}_0(0)$. The allowed wavevectors for any crystal structure are defined by

$$\boldsymbol{\kappa} = \sum_{\alpha} \mathbf{b}_{\alpha} \frac{n_{\alpha}}{N_{\alpha}}, \quad (2.11)$$

where \mathbf{b}_{α} are the reciprocal lattice vectors and $-N_{\alpha}/2 < n_{\alpha} \leq N_{\alpha}/2$, where n_{α} are integers and N_{α} are now constant even integers. The wavevectors are taken to be in the first Brillouin zone [130].

For the LJ argon and SW silicon systems studied here, the cubic conventional cells are used with four (argon) and eight (silicon) atoms per unit cell. For the MD simulations of LJ argon and

SW silicon, cubic simulation domains are used (i.e., $N_1 = N_2 = N_3 = N_0$) [12, 81, 123]. For the CNT, the Brillouin zone is one-dimensional, so that $N_1 = N_2 = 1$, and we take $N_3 = 50$ [112].

2.3.2 Phonon Lifetimes and Frequencies

Once the allowed wavevectors are specified, the atomic velocities from an MD simulation can be used to calculate Φ' using Equation (2.8). To calculate Φ [Equation (2.3)], requires the phonon mode eigenvector, which can be obtained using harmonic lattice dynamics calculations and the finite temperature lattice constant (i.e., quasi-harmonic lattice dynamics calculations) [19, 134]. The Φ and Φ' methods can be used for any material system where there are available interatomic potentials.

The phonon frequencies and lifetimes are found by fitting the spectral curves Φ and Φ' with Lorentzian functions using a non-linear least squares method. Both of these phonon properties are independent of the Lorentzian peak magnitude. For Φ' , the different polarizations at a given wavevector are superimposed by definition of Equation (2.8). The different polarizations can be fit individually using single Lorentzian peaks or as a superposition of peaks. At high temperatures, the broadening of the peaks from different polarizations can make it difficult to uniquely locate the peaks in Φ' . Knowledge of the quasi-harmonic frequencies is necessary to identify the unique peaks in Φ' as well as degeneracies. [12, 135].

Φ has the advantage that degenerate and nearly degenerate polarizations can be isolated and fit individually. The uncertainty in the predicted phonon frequencies is on the order of the frequency resolution used to perform the fast Fourier transforms required to evaluate Φ and Φ' , which is $10^2 - 10^4$ less than the phonon frequencies studied in this work (see Sections 2.4.1, 2.4.2, and 2.4.3). At the temperatures studied in this work, we find that fitting single or simultaneous peaks in either Φ or Φ' results in less than five percent difference in the predicted lifetimes. The uncertainty from fitting the Lorentzian functions is between five and ten percent of the predicted

lifetimes, with the error increasing with increasing temperature.*

To illustrate the procedure, Φ was calculated for LJ argon (Section 2.4.1) with $N_0 = 10$ and $T = 20$ K, where T is temperature. Φ for the two modes denoted by A and B [see Fig. A.1(b)] and wavevector $[\pi/5a, \pi/5a, \pi/5a]$ is shown in Fig. 2.1(b). The lower-frequency peak corresponds to the longitudinal acoustic mode, [19] while the higher frequency peak corresponds to an acoustic mode which has been zone-folded (see Section A.3.3). As discussed in Section 2.2.2, the frequency and lifetime extraction in normal mode decomposition can also be performed in the time domain. The autocorrelation of the normal mode kinetic and total energies for the two modes (A and B) are plotted in Fig. 2.1(a). The fits to Eq. (2.6) for the total energy are also plotted and fall on top of the raw data. The inset to Fig. 2.1(a) shows the integration of the total energy according to Eq. (2.7) and the converged values of the lifetimes. The time-domain analysis on the total mode energy has the advantage that only one property needs to be fit – the lifetime. Extracting the frequency from the kinetic energy in the time domain is challenging, however, particularly for short lifetimes, where they will be only a few oscillations in the decay. The frequency is easily extracted from the frequency-domain analysis.

2.3.3 Thermal Conductivity

Once the frequencies and lifetimes of all phonon modes in the first Brillouin zone are obtained, the bulk thermal conductivity in direction \mathbf{n} , $k_{\mathbf{n}}$, can be calculated from [20]

$$k_{\mathbf{n}} = \sum_{\boldsymbol{\kappa}} \sum_{\nu} c_{ph}(\boldsymbol{\kappa}) v_{g,\mathbf{n}}^2(\boldsymbol{\kappa}) \tau(\boldsymbol{\kappa}). \quad (2.12)$$

Here, c_{ph} is the phonon volumetric specific heat and $v_{g,\mathbf{n}}$ is the component of the group velocity vector in direction \mathbf{n} . Since the systems we consider are classical and obey Maxwell-Boltzmann

*The range of data must be selected when fitting the Lorentzian functions to Φ or Φ' . This range should be large enough for the Lorentzian functions to decrease significantly from their value at half-width at half-maximum, where the linewidth is specified, but not too large as to pick up noise. The error in predicting the lifetime is obtained by varying the range of data used to fit the Lorentzian function.

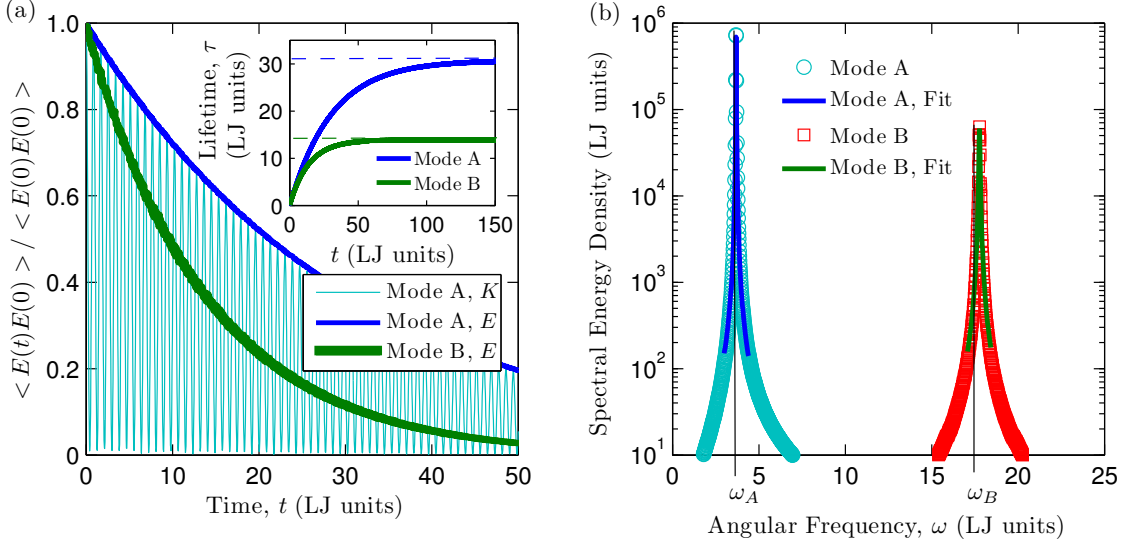


Figure 2.1: Raw data and fits for normal mode decomposition in (a) time-, and (b) frequency-domain analysis for two of the [100] phonon modes from the conventional unit cell for $N_0 = 10$ [see Fig. A.1(b)] The inset in (a) shows the convergence of the lifetime according to Eq. (2.7). In (b), the vertical lines denote the frequency predicted from harmonic lattice dynamics calculations.

statistics [86], the specific heat is k_B per mode in the harmonic limit, where k_B is the Boltzmann constant. As temperature increases, anharmonicity causes the mode specific heats to deviate from k_B [81]. The effect is small for the systems and temperatures studied here. For LJ argon, the mode-averaged specific heat has been predicted to be $0.95k_B$ per mode at a temperature of 40 K and approaches k_B with decreasing temperature [81]. For SW silicon at a temperature of 300 K, the predicted mode-averaged specific heat is $1.01k_B$ per mode [103]. For the CNT at $T = 300$ K, we predict the mode-averaged specific heat to be $1.03k_B$ per mode. Because we do not have mode-dependent specific heats, we take the specific heat to be k_B per mode for the three systems studied (argon, silicon, and CNT). The group velocity vector is the gradient of the dispersion curve (i.e., $\partial\omega/\partial\kappa$) and can be calculated from the frequencies and wavevectors using finite differences. In this work, the group velocities are calculated using the frequencies from quasi-harmonic lattice dynamics calculations because a smaller finite difference in wavevector

can be used than what is available from the MD simulations (see Section 2.3.1). [†]

2.3.4 Computational Cost and Work Flow Optimization

The computational time required to perform normal mode decomposition depends on the number of atoms in the system, N_a , and the number of atoms in the unit cell, n . For the eigenvalue problem associated with harmonic lattice dynamics, the time required for each wave vector scales as n^3 and the required memory scales as n^2 . This poor scaling limits the study of systems with more than 10,000 atoms in the unit cell (as might be required for a nanostructure such as a thin films or nanowire), for which the calculations will take one to two days given current computational resources. The harmonic lattice dynamics calculations for different wave vectors are trivially parallelizable and can be performed using the open-source GULP package [134]. For efficiently parallel MD algorithms (e.g., the open-source LAMMPS package [136]), the simulation time and required memory scale as N_a .

The computational time and memory required to project the atomic velocities and positions onto the normal mode coordinates scale as N_a and these calculations are trivially parallelizable over the normal modes. Reasonable computational times can be realized by using LAMMPS to perform the MD simulations, outputting the atomic trajectories, and writing programs to perform the normal mode decomposition using a scripting language like Python with the NumPy module [137]. Because normal mode decomposition is trivially parallelizable on multi-core architectures over the normal modes, massively parallel calculations can be achieved by using a PBS scheduler such as TORQUE. Ideally, however, to reduce memory requirements, the projection of the atomic positions and velocities onto the normal mode coordinates and calculations of the normal mode potential and kinetic energies would be directly built into the MD code. The energies would then

[†]The anharmonic frequency shift affects the group velocity. McGaughey and Kaviany find that anharmonic and quasi-harmonic predictions of the group velocity differ for LJ Argon by less than one percent at a temperature of 50 K and that the difference decreases with decreasing temperature [81]. The anharmonic frequency shifts are on average a few percent for LJ argon at a temperature of 40 K and are less for the other temperatures and systems studied here.

be periodically output to perform the required autocorrelations and/or Fourier transforms.

In normal mode decomposition, the sampling rate must be high enough to capture the maximum frequency in the system. The sampling rate and total run time should be chosen in powers of two as a convenience in performing fast Fourier transforms. Obtaining the phonon properties from Eqs. (2.1), (2.4), (2.6), and (2.7), requires specification of a time or frequency range and initial guesses for the frequency and lifetime. These parameters can be obtained from observation of the raw data. An initial guess for the frequency can also be obtained from the harmonic lattice dynamics calculations. When investigating new systems, it is best to fit the phonon properties in a semi-automated way (i.e., each fit should be visualized so that the fitting parameters can be tuned). Once appropriate fitting parameters are chosen, the fitting can usually be fully automated for large data sets. For crystalline systems, only the properties of the modes of the irreducible wave vectors are needed, such that the autocorrelations or Fourier transforms for symmetric modes can be averaged before fitting (see Appendix A.3.2 for a discussion of symmetries).

For the Φ and Φ' methods, the computational cost of evaluating Equation (2.8) is less than that for Equation (2.3) by a factor of $3b$. For bulk crystals, the number of atoms in the unit cell is typically small ($n < 10$). For the (8,8) CNT system, $n = 32$ and evaluating Φ' is two orders of magnitude less expensive than evaluating Φ .

To calculate the phonon lifetimes, the MD simulation time should be an order of magnitude longer than the longest phonon lifetime [138]. If only the phonon frequencies are required, however, the location of the peaks in Φ and Φ' develop in a time on the order of the inverse of the phonon frequency, $1/\omega_0(\kappa)$. For the systems studied here, this time can be two to five orders of magnitude less than the time needed to develop the lifetimes.

Fitting Φ' becomes challenging at higher temperatures, when the phonon linewidths broaden and become comparable to the spacing between mode frequencies. The cost of fitting Φ' can be reduced by fitting the peaks from all allowed wavevectors in the system simultaneously, but the error associated with this procedure is unknown [36]. We find that a semi-automated procedure,

whereby the fits are visualized, is necessary to ensure that all peaks are fit correctly. While the computational cost of fitting Φ' is much smaller than the computational cost of calculating Φ' , the semi-automated fitting procedure can be of similar time cost to the user. The cost of fitting Φ is much smaller because the different polarization peaks can be isolated and the fitting can be fully automated.

2.4 Case Studies

2.4.1 Lennard-Jones Argon

We now use MD simulation to compare the SED, phonon properties, and thermal conductivity calculated for LJ argon using Φ and Φ' . The MD simulations are performed using LAMMPS.[136] A truncated and shifted potential cutoff scheme is used with a cutoff radius of 8.5 Å. The quasi-harmonic phonon frequencies, eigenvectors, and group velocities are generated using GULP [134]. We consider temperatures of 5, 20, and 40 K at zero-pressure with lattice constants of 5.278, 5.315, and 5.371 Å. For LJ argon, Turney et al. found that lattice dynamics-based predictions of thermal conductivity (e.g., by anharmonic lattice dynamics or Φ) start to diverge from MD-based predictions (e.g., from the direct or Green-Kubo methods) above half the melting temperature ($T_{\text{melt}} \approx 80$ K) [12]. Here, we limit the temperature to below half the melting temperature for the three systems studied (argon, silicon, and CNT).

The MD system consists of $N_1 \times N_2 \times N_3 = 8^3 = 512$ conventional cubic unit cells for a total of 2048 atoms ($b = 4$ atoms). Using a 4.285 fs time step, the system is equilibrated for 2^{20} time steps before collecting data every 2^5 time steps for an additional 2^{20} time steps in the *NVE* ensemble (constant number of atoms, system volume, and total system energy) [86]. The sampling rate must be high enough to capture the highest phonon frequency in the system. The sampling rate and total run time are chosen in powers of two as a convenience in performing the fast Fourier transforms required to efficiently evaluate Φ and Φ' . The same MD simulation data

are used to calculate Φ and Φ' . Five simulations with different initial conditions are performed and the Φ and Φ' values are averaged before the peak fitting. Φ and Φ' are further averaged over degenerate wavevectors in the Brillouin zone, reducing the wavevectors to the first octant [87].

The SED (Φ and Φ') for the wavevector $[\pi/2a, 0, 0]$ is presented in Fig. 2.2 for all three temperatures (the edge of the Brillouin zone is at $[\pi/a, 0, 0]$). For Φ , the spectral curve is plotted as a superposition over the twelve phonon polarizations, with degeneracy reducing the number of peaks to seven. Overall, Φ' does not equal the total phonon spectral energy density Φ , but the major features are similar. At all temperatures there are linewidth variations between the two spectral curves. The peak magnitudes become comparable for Φ and Φ' as the temperature increases.

The phonon frequencies and lifetimes extracted for all allowed wavevectors in the first Brillouin zone using Φ and Φ' at each of the three temperatures are compared on a mode-by-mode basis in Figs. 2.3(a), 2.3(b), and 2.3(c). There, ω_0 , ω'_0 , τ , and τ' refer to the mode properties predicted using Φ and Φ' . The phonon frequencies agree well at all three temperatures, with increasing scatter at high temperatures and high frequencies. This scatter is due to the high-frequency peak broadening seen in Fig. 2.2 at $T = 40$ K, which can force peaks close in frequency for Φ' to be fit as a single Lorentzian function. The frequencies predicted by Φ and Φ' include the effects of anharmonicity, which increase the frequencies compared to the quasi-harmonic predictions [12, 135]. The agreement between the frequencies predicted from Φ and Φ' is explained in Appendix A.2.

The lifetimes show large scatter between Φ and Φ' on a mode-by-mode basis, with increasing scatter at high temperature that shows no systematic difference. The scatter at high frequencies is in part due to the peak broadening seen in Fig. 2.2, which can force peaks close in frequency for Φ' to be fit as a single Lorentzian function with a single lifetime. The broadening does not affect fitting at low frequencies, where the linewidths are much smaller than the peak spacings. There, any scatter comes solely from the difference between Φ and Φ' .

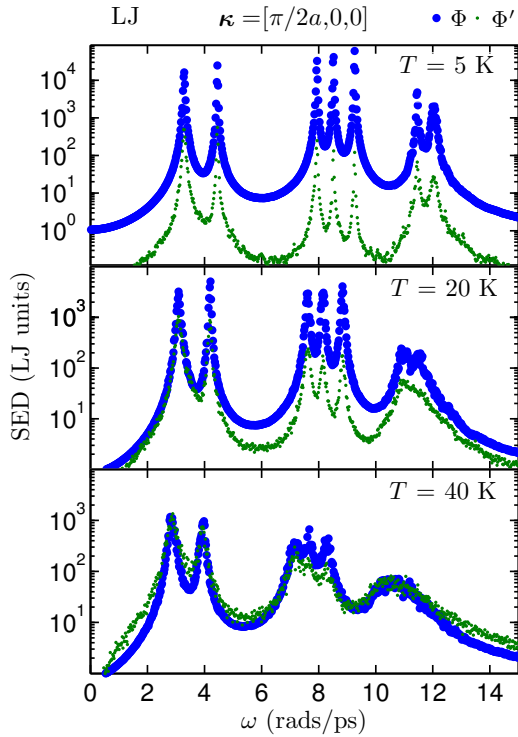


Figure 2.2: The phonon spectral energy density (Φ) is plotted as larger blue circles. The proposed alternative expression for the phonon spectral energy density (Φ') is plotted as smaller green points. The wavevector is $(\pi/2a, 0, 0)$. Note that peak broadening at higher temperatures and frequencies above 10 rads/ps can force peaks close in frequency for Φ' to be fit as a single Lorentzian function. Φ does not suffer from this issue since the broadened peaks can be fit individually.

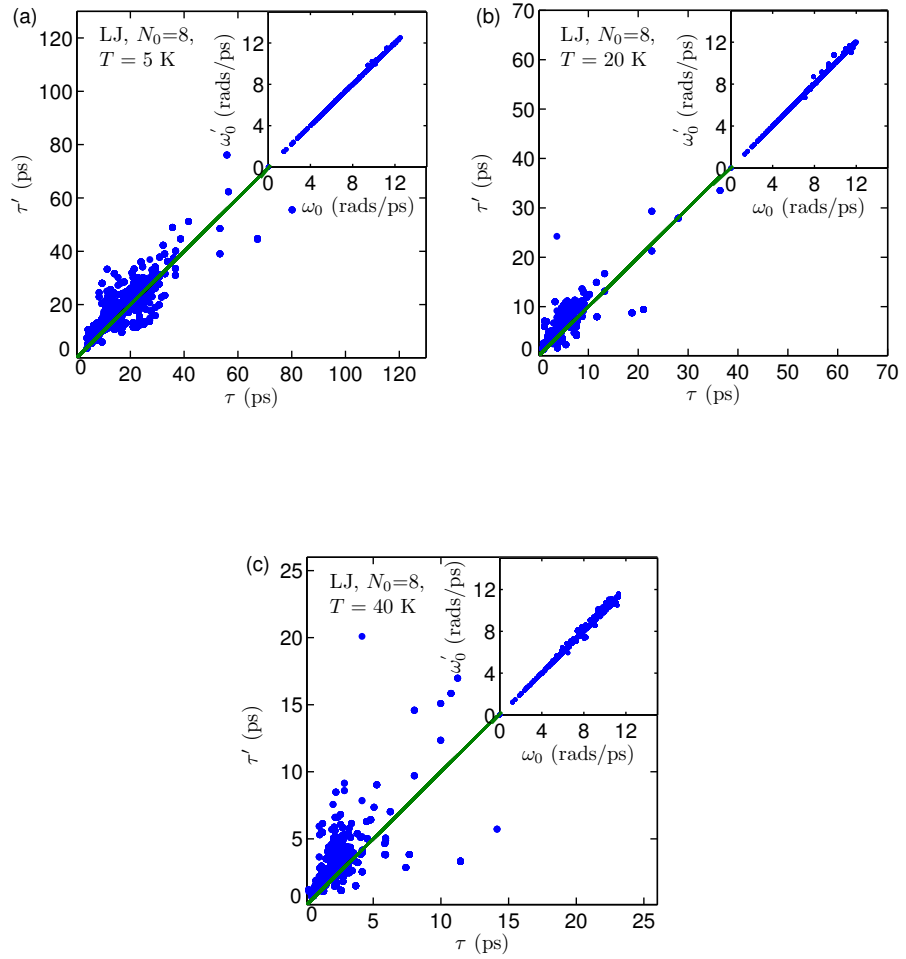


Figure 2.3: Comparison of the phonon frequencies and lifetimes predicted using Φ (ω and τ) and Φ' (ω' and τ') for LJ argon at temperatures of (a) 5 K, (b) 20 K, and (c) 40 K. The phonon frequencies agree well at all three temperatures, while the phonon lifetimes show large scatter.

The phonon properties are then used to predict thermal conductivity using Equation (2.12). The results are presented in Table 3.1. The bulk thermal conductivities provided in Table 3.1 are predicted using the finite simulation-size scaling procedure discussed in [12]. The bulk thermal conductivities predicted from Φ' are smaller and outside the uncertainty for those predicted from Φ for temperatures of 5 and 20 K. While the bulk thermal conductivities at a temperature of 40 K agree within their uncertainties, the predicted mode-by-mode lifetimes show large scatter [Fig. 2.3(c)] and the agreement should be regarded as coincidental.

The disagreement between Φ and Φ' in thermal conductivity comes directly from the differences in the phonon lifetimes. All other properties (frequencies, group velocities, specific heats) are nearly or exactly the same for the two calculations. The bulk thermal conductivities predicted from Φ and Φ' are also compared to predictions from the Green-Kubo method[86] in Table 3.1. For $N_1 = N_2 = N_3 = 8$, the thermal conductivity predicted by the Green-Kubo method is converged with respect to the simulation size [81]. The same MD data used to calculate Φ and Φ' is used for the Green-Kubo predictions. For all three temperatures, there is good agreement between the thermal conductivity predictions using Φ and Green-Kubo. For temperatures of 20 and 40 K, there is good agreement between the predictions from Φ , Green-Kubo, and previous reports using non-equilibrium MD, anharmonic lattice dynamics, and time-domain Φ [12].

2.4.2 Stillinger-Weber Silicon

We next compare the phonon properties and thermal conductivity predicted from Φ and Φ' for SW silicon [131] at a temperature of 300 K and zero pressure with a lattice constant of 5.437 Å. The SW system is stiffer (larger phonon group velocities, frequencies, and lifetimes) than LJ argon and is an additional test to determine if there is a systematic error in the predictions from Φ' . The MD simulations are performed using LAMMPS [136]. The MD system consists of $N_1 \times N_2 \times N_3 = 6^3 = 216$ conventional unit cells for a total of 1728 atoms ($b = 8$ atoms).

Table 2.1: Thermal conductivity values in W/m-K predicted using the Φ , Φ' , and Green-Kubo methods. The predictions for Φ and Green-Kubo for the LJ system are in good agreement with those from other atomistic simulation methods [12] while those from Φ' differ and show no consistent behavior. The uncertainties in the predicted thermal conductivities for Φ and Φ' come predominantly from the finite simulation-size scaling procedure (see Ref. [12, 85]), where the phonon properties and thermal conductivity are predicted for increasing system sizes ($N_1 = N_2 = N_3$) to extrapolate a bulk thermal conductivity. For SW silicon and the CNT, the extrapolation procedure is not performed.

T (K)	Green-Kubo	Φ	Φ'
LJ (bulk)			
5	8.0 ± 0.30	7.9 ± 0.42	5.8 ± 0.31
20	1.3 ± 0.15	1.2 ± 0.07	1.0 ± 0.10
40	0.45 ± 0.07	0.47 ± 0.03	0.49 ± 0.05
SW ($N_1 = N_2 = N_3 = 6$)			
300		322 ± 16	396 ± 38
CNT ($N_1 = N_2 = 1, N_3 = 50$)			
300		428 ± 21	398 ± 40

The phonon frequencies, eigenvectors, and group velocities are generated using GULP [134].

Using a 0.5 fs timestep, the system is equilibrated for 2^{20} time steps before collecting data every 2^5 time step for 2^{22} time steps in the NVE ensemble [86]. As with the LJ system, the sampling rate is determined by the highest phonon frequency in the system. Five simulations with different initial conditions are performed and the Φ and Φ' values are averaged before the peak fitting. Φ and Φ' are further averaged over degenerate wavevectors in the Brillouin zone, reducing the wavevectors to the first octant [87].

The extracted phonon frequencies and lifetimes are plotted in Fig. 2.4. As with the LJ system, the phonon frequencies are predicted accurately by Φ' but the lifetimes show large scatter on a mode-by-mode basis. For the system size studied, Φ' predicts a larger thermal conductivity than Φ outside the prediction uncertainties, in contrast to the LJ system (see Table 3.1). The disagreement in thermal conductivity comes directly from the phonon lifetimes.

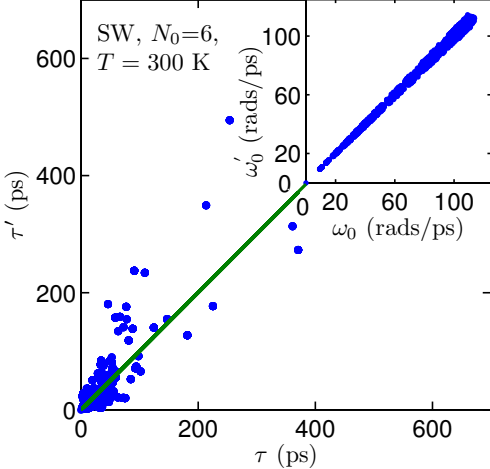


Figure 2.4: Comparison of the phonon frequencies and lifetimes predicted using Φ (ω and τ) and Φ' (ω' and τ') for SW silicon. The phonon frequencies agree well, while the phonon lifetimes show large scatter.

2.4.3 Carbon Nanotube

Finally, we compare the phonon properties and thermal conductivities predicted by Φ and Φ' for an (8,8) CNT (diameter of 1.10-nm and length of 12.3 nm) at a temperature of 300 K and zero pressure [112].

The interactions in the CNT system are modeled using the REBO potential without the four-body interaction term [132]. The MD simulations are performed using an in-house code. The MD system consists of 1600 atoms (32 atoms/unit cell). The phonon frequencies, eigenvectors, and group velocities are generated using an in-house code. The purpose of simulating this system is to check the results of Thomas et al. [112] (who used Φ' and non-equilibrium MD), and to compare the predictions of Φ' and Φ .

Using a 1.0 fs timestep, the system is equilibrated for 2^{20} time steps before collecting data every 2^3 time step for 2^{22} time steps in the NVE ensemble [86]. As with the LJ and SW systems, the sampling rate is determined by the highest phonon frequency in the system. Five simulations with different initial conditions are performed and the Φ and Φ' values are averaged before the peak fitting. Since the Brillouin zone of the CNT is one-dimensional, Φ and Φ' are further

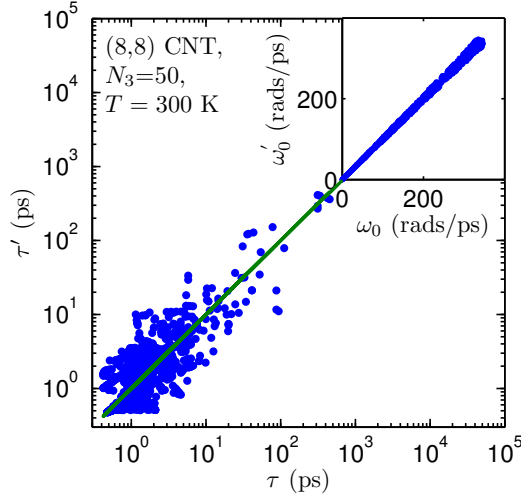


Figure 2.5: Comparison of the phonon frequencies and lifetimes predicted using $\Phi(\omega, \tau)$ and $\Phi'(\omega', \tau')$ for a (8,8) CNT modeled using the REBO potential. The phonon frequencies agree well, while the phonon lifetimes show large scatter.

averaged over directionally-degenerate wavevectors.

The phonon frequencies and lifetimes for the allowed wavevectors in the one-dimensional Brillouin zone are shown in Fig. 2.5. Like the LJ and SW silicon systems, the phonon frequencies can be predicted accurately by Φ' , but the lifetimes show large scatter. The estimated thermal conductivity of the CNT predicted using Φ' is in agreement with the results of Thomas et al. [112]. The thermal conductivity predicted by Φ' is less than that predicted by Φ , but not outside their uncertainties.

2.5 Summary

We presented the correct phonon SED, Φ , and its relation to the phonon frequencies and lifetimes. We then presented an alternative formulation to the phonon spectral energy density, Φ' , which does not require the phonon mode eigenvectors. Because Φ' does not contain the eigenvectors, this alternative formulation does not represent the phonon spectral energy density, but does contain information about the phonon dispersion as the temperature approaches 0 K (see

Appendix A.2).

We then calculated the phonon SED for LJ argon, SW silicon, and a CNT modeled with the REBO potential using Φ and Φ' . The phonon frequencies and lifetimes predicted from Φ and Φ' are shown in Figs. 2.3, 2.4 and 2.5. The frequencies are in good agreement between the two SED methods, while the lifetimes show large scatter.

The phonon SED Φ is well-defined theoretically, while Φ' does not properly map to the phonon energies since it is missing the phonon mode eigenvector. We deduce that this is the reason Φ' does not accurately predict the phonon lifetimes. It is surprising how close the predicted thermal conductivities can be using Φ and Φ' (LJ at $T = 40$ K and the CNT results). The thermal conductivities predicted by Φ and Φ' , however, show no consistency for the three systems studied.

The most important predictions are the mode-by-mode phonon properties. Of particular importance are the lifetimes, which are the key input for Boltzmann transport equation-based models [13]. Thus, we do not recommend Φ' for predicting phonon lifetimes or thermal conductivity. Any agreement in thermal conductivity predictions between atomistic studies[112] and experiment [107, 128] should be regarded as coincidental, and the phonon lifetime reductions predicted for systems with additional scattering methods [36, 112] should only be interpreted qualitatively. The use of Φ' in future work is discouraged and we reccomend the use of Φ .

Chapter 3

Predicting Alloy Vibrational Mode Properties using Lattice Dynamics Calculations, Molecular Dynamics Simulations, and the Virtual Crystal Approximation

The virtual crystal (VC) approximation for mass disorder is evaluated by examining two model alloy systems: Lennard-Jones argon and Stillinger-Weber silicon. In both material systems, the perfect crystal is alloyed with a heavier mass species up to equal concentration. The analysis is performed using molecular dynamics simulations and lattice dynamics calculations. Mode frequencies and lifetimes are first calculated by treating the disorder explicitly and under the VC approximation, with differences found in the high-concentration alloys at high frequencies. Notably, the lifetimes of high-frequency modes are underpredicted using the VC approximation, a result we attribute to the neglect of higher-order terms in the model used to include point-defect

scattering. The mode properties are then used to predict thermal conductivity under the VC approximation. For the Lennard-Jones alloys, where high-frequency modes make a significant contribution to thermal conductivity, the high-frequency lifetime underprediction leads to an underprediction of thermal conductivity compared to predictions from the Green-Kubo method, where no assumptions about the thermal transport are required. Based on observations of a minimum mode diffusivity, we propose a correction that brings the VC approximation thermal conductivities into better agreement with the Green-Kubo values. For the Stillinger-Weber alloys, where the thermal conductivity is dominated by low-frequency modes, the high-frequency lifetime underprediction does not affect the thermal conductivity prediction and reasonable agreement is found with the Green-Kubo values.

3.1 Introduction

Due to their potentially low thermal conductivities, disordered materials (e.g., alloys, amorphous solids, aerogels) are used in applications ranging from thermoelectric energy conversion to thermally insulating barriers. [1, 2, 3, 4, 5, 6, 7, 8, 9, 10] Disordered lattices are a subgroup of disordered materials where the atomic positions follow a lattice structure but the constituent species are spatially random. Examples include isotopic solids, where the species have the same electronic structure but small mass variations,[30, 35] and alloys, our focus here, where at least two distinct species are present.[34, 139]

We further restrict our focus to dielectric or semiconducting solids, where the heat is conducted by the atomic vibrational modes. Predicting the thermal conductivity of such materials requires the properties of the full spectrum of vibrational modes. [20, 48, 73] Accurate predictions of these properties for crystalline systems (i.e., perfect lattices) can be made with anharmonic lattice dynamics (ALD) theory using input from density functional theory (DFT) calculations.[26, 28, 29, 30, 31, 32, 36, 37, 38, 39] Computational costs limit DFT calculations

to less than 100 atoms, however, making it challenging to explicitly incorporate the effects of disorder. [27, 30, 37, 38, 39, 104, 140]

Disorder is typically included in the ALD framework using Abeles' virtual crystal (VC) approximation, whereby the disordered solid is replaced with a perfect VC with properties equivalent to an averaging over the disorder (e.g., atomic mass, bond strength).[34] The ALD calculations are performed on a small unit cell with the averaged properties (i.e., all vibrational modes are phonons) and phonon-phonon and phonon-disorder scattering are included as perturbations. [30, 34, 35, 37, 39] Except for low-frequency (long-wavelength) acoustic modes, the general validity of this assumption is unclear. We will refer to this approach as VC-ALD. Recent work using DFT calculations and the VC-ALD approach has modeled disordered lattices with relatively large (\sim 10-100 W/m-K) [30, 38, 39] and small (\sim 1 W/m-K)[37] thermal conductivities. No comprehensive study has been performed to assess the applicability of the VC-ALD approach for a range of disorder strength.

The objective of this study is to investigate the use of the VC approximation for predicting the vibrational mode properties and thermal conductivity of alloys by a detailed comparison of three predictive methods: (i) molecular dynamics (MD)-based normal mode decomposition (NMD), (ii) MD-based Green-Kubo (GK), and (iii) VC-ALD. By using computationally-inexpensive empirical potentials for argon [Lennard-Jones (LJ) at a temperature of 10 K] [130] and silicon [Stillinger-Weber (SW) at a temperature of 300 K], [131] we can self-consistently study the effects of disorder both explicitly and as a perturbation. For both materials, the perfect lattice is disordered with a heavier mass species up to equal concentration, spanning a range of small to large disorder. By spanning this range, the limits of the perturbative models are examined.

The remainder of the paper is organized as follows. In Section 3.2, the theoretical formulation of thermal transport in ordered and disordered solids and the computational framework are described. In Section 4.4, the frequencies, group velocities, lifetimes, and diffusivities of the vibrational modes of the LJ argon alloys are predicted when the disorder is explicitly modeled

and when it is treated as a perturbation in the VC approximation. A breakdown of the VC-ALD method is identified by a comparison with the VC-NMD method in Section 3.3.3.2 and a correction is suggested in Section 3.3.4. The vibrational mode properties are then used to predict thermal conductivities in Section 3.4, allowing for a comparison to the predictions of the top-down GK method, where no assumptions about the nature of the thermal transport are required. The vibrational mode properties and thermal conductivity of the SW silicon alloys, where low-frequency modes dominate the thermal conductivity, are predicted in Section 3.5 to provide a comparison and contrast to the LJ argon alloys.

3.2 Theoretical and Computational Framework

3.2.1 Thermal Conductivity Prediction

To predict the thermal conductivity of a disordered lattice, one begins with the theory for a perfect lattice. For a perfect lattice, all vibrational modes are phonon modes, which by definition are delocalized, propagating plane waves. [20] Using the single-mode relaxation time approximation [20] to solve the Boltzmann transport equation gives an expression for thermal conductivity in direction \mathbf{n} ,

$$k_{ph,\mathbf{n}} = \sum_{\boldsymbol{\kappa}} \sum_{\nu} c_{ph}(\boldsymbol{\kappa}_{\nu}) v_{g,\mathbf{n}}^2(\boldsymbol{\kappa}_{\nu}) \tau(\boldsymbol{\kappa}_{\nu}). \quad (3.1)$$

Here, the sum is over the phonon modes in the first Brillouin zone, $\boldsymbol{\kappa}$ is the wave vector, and ν labels the polarization branch. The phonon mode has frequency $\omega(\boldsymbol{\kappa}_{\nu})$, volumetric specific heat $c_{ph}(\boldsymbol{\kappa}_{\nu})$, \mathbf{n} -component of the group velocity vector $v_{g,\mathbf{n}}(\boldsymbol{\kappa}_{\nu})$, and lifetime $\tau(\boldsymbol{\kappa}_{\nu})$.

The relaxation time approximation has been found to be valid for lower thermal conductivity materials (e.g., Si and SiGe alloys), [26, 28, 39] while larger thermal conductivity materials such as GaN and diamond require an iterative solution to the BTE for more accurate predictions

using Eq. (3.1). [27, 30] For the crystalline LJ argon and SW silicon phases, the lattices and the components of their thermal conductivity tensors are cubically symmetric, so that we will refer to k_{ph} as an isotropic scalar thermal conductivity. This isotropy will hold for disordered lattices in the infinite-size limit. Since MD simulations are classical and obey Maxwell-Boltzmann statistics,[86] the volumetric specific heat is k_B/V per mode in the harmonic limit, where V is the system volume and k_B is the Boltzmann constant. This harmonic approximation for specific heat has been shown to be valid for LJ argon and SW silicon at the temperatures of interest here [81, 103] and is used so that direct comparisons can be made between the MD- and lattice dynamics-based methods.

For disordered systems, the vibrational modes are no longer pure plane-waves (i.e., phonon modes), except in the low-frequency (long-wavelength) limit. When applied in the classical limit, the Allen-Feldman (AF) theory computes the contribution of diffusive, non-propagating modes (i.e., diffusons) to thermal conductivity from[47]

$$k_{AF} = \sum_{\text{diffusons}} \frac{k_B}{V} D_{AF,i}(\omega_i), \quad (3.2)$$

where $D_{AF,i}$ is the mode diffusivity and ω_i is the frequency of the i th diffuson. The diffusivity of diffusons can be calculated from harmonic lattice dynamics theory. [47, 48, 52]

Assuming that all vibrational modes travel with the sound speed, v_s , and scatter over a distance of the lattice constant, a , a high-scatter (HS) limit of thermal conductivity in the classical limit is[2]

$$k_{HS} = \frac{k_B}{V_b} b v_s a, \quad (3.3)$$

where V_b is the volume of the unit cell and b is the number of atoms in the unit cell. The HS limit will be used to discuss the differences between the LJ argon and SW silicon alloys.

3.2.2 Virtual Crystal Approximation

Under the VC approximation, the disordered solid is replaced with a perfect, single-species crystal with properties (e.g., density, cohesive energy) equivalent to an averaging over the disorder (e.g., atomic mass, bond strength).[34] The VC approximation is visualized for an alloy in Figs. 3.1(a) and 3.1(b), where a mass-disordered supercell is replaced by a perfect crystal with an averaged mass. Abeles first introduced the concept of a VC to predict the thermal conductivity of SiGe, GaAs/InAs, and InAs/InP alloys. [34] Klemens-Callaway theory, which is valid for low-frequency modes and small disorder, was used to model the phonon-phonon and phonon-defect scattering. [21, 23, 34, 90, 91, 141] The Abeles theory is conceptually simple, treating both disorder and anharmonicity as perturbations, and leads to a closed-form analytical function for the thermal conductivity. With the use of phenomenological fitting parameters, good agreement between the predictions and experimental measurements was found for SiGe and GaAs/InAs alloys. Deviations were observed for InAs/InP alloys at large concentrations of InP, which were attributed to the large mass ratio of 3.7 between indium and phosphorus.[34]

When considering alloys, it is important to note that the overall disorder strength is determined by the mass ratio, the stiffness ratio, and the alloy concentration. Cahill and co-workers found that as little as $6.2 \times 10^{19} \text{ cm}^{-3}$ germanium reduces the thermal conductivity of epitaxial silicon layers by a factor of two. [142] Using the Abeles theory, they explained this result by mass perturbative disorder alone (the Ge/Si mass ratio is 2.6). [142, 143] The relative effects of bond and mass disorder were investigated computationally using MD simulations by Skye and Schelling for SiGe alloys up to equal concentration. [76] They also found that mass disorder is the dominant scattering mechanism. Subsequent studies have modeled the effect of differing species by only including atomic mass differences.[41, 79]

Unlike the phenomenological Abeles theory, the VC-ALD approach predicts thermal conductivity by directly summing over the modes of the full vibrational spectrum, with phonon-phonon and phonon-defect scattering treated as perturbations. [30, 37, 39] In the VC-ALD method,

the phonon-phonon scattering is predicted using ALD.[12, 29] The phonon-defect scattering is treated using perturbative methods that can handle mass and/or bond disorder. [23, 35, 90, 91] In $\text{Ni}_{0.55}\text{Pd}_{0.45}$, which has a large mass ratio (1.8) and concentration of each species, experimental measurements of vibrational frequencies and linewidths agree well with predictions from the perturbative mass-disorder theory. [35, 91, 141]

Using DFT methods to predict the mode-specific phonon properties of the VC, Lindsay and Broido found good agreement between VC-ALD and experimental measurements of thermal conductivity for isotopically defected GaN (the gallium isotopes have concentrations of 0.6 and 0.4 and a mass ratio of 1.03).[30] Garg et al. used DFT calculations with VC-ALD to predict the thermal conductivity of SiGe alloys for all concentrations at a temperature of 300 K, obtaining good agreement with experiment.[39] By including disorder explicitly in their ALD calculations, the predicted thermal conductivity decreased by 15%. Isotopically-defected GaN and low concentration SiGe alloys have relatively large thermal conductivities at a temperature of 300 K (\sim 100 W/m-K). Li et al. used DFT calculations with VC-ALD to predict the thermal conductivity of $\text{Mg}_2\text{Si}_x\text{Sn}_{1-x}$ (\sim 10 W/m-K) in good agreement with experimental measurements for all concentrations.[38] The VC-ALD approach has also been used to predict the effect of interfacial mixing in GaAs/AlAs superlattices, but the thermal conductivity predictions were not compared with experimental measurements.[32] In our survey of experimental measurements and numerical modeling, we find that VC predictions tend to be accurate when the disordered lattice thermal conductivity is significantly above the high-scatter limit [Eq. (3.3)], which tends to be around 1 W/m-K. [2, 30, 34, 39, 141, 142, 143]

An ALD study using phonon properties from DFT calculations for crystalline PbTe[31] predicted thermal conductivities of 2 W/m-K at a temperature of 300 K in fair agreement with experiment. For PbTeSe alloys, a VC-ALD study predicted a small thermal conductivity reduction compared to the perfect crystals.[37] Experimental results are limited for these alloys,[144, 145] making it difficult to asses the validity of the VC-ALD approach for materials whose thermal

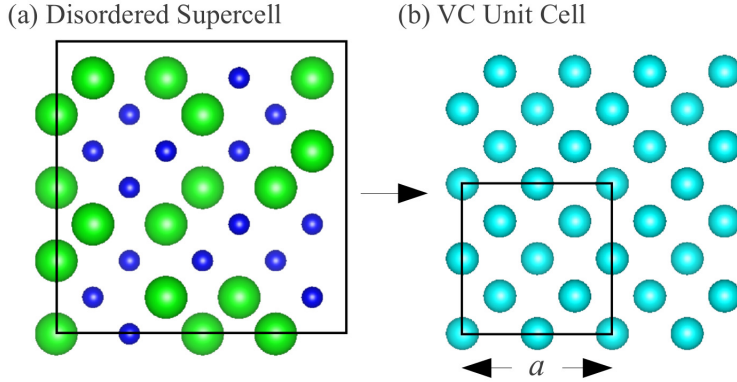


Figure 3.1: (a) Explicitly disordered alloy supercell of silicon and “heavy” silicon ([100] direction into the page). [146] (b) Equivalent VC supercell with one averaged mass. The sphere size represents increasing mass only, no bond disorder is considered. The 8-atom conventional cubic unit cell is shown in (b).

conductivities approach the high-scatter limit.

Given all these results, it is unclear what limitations exist for using the VC approach. In this study, we will consider a low thermal conductivity alloy using the LJ potential and a high thermal conductivity alloy using the SW potential. The computational studies discussed above were limited to VC-ALD because of DFT calculation costs. Our use of computationally inexpensive empirical potentials allows us to include the disorder explicitly and as a perturbation and to compare the predictions.

3.2.3 Calculation and Simulation Details

The key to explicitly incorporating the effects of disorder is to use large disordered supercells. Perfect and disordered lattice supercells are generated using the conventional unit cells for LJ argon ($n = 4$) and SW silicon ($n = 8$), where n is the number of atoms in the unit cell. Supercells are built cubically with size N_0 , where N_0 is the number of unit cell repetitions in the three spatial directions. Supercells up to $N_0 = 12$ (6,096 atoms) are used for the LJ argon calculations. For SW silicon, $N_0 = 8$ (4,096 atoms) is used for the MD-based NMD calculations and $N_0 \leq 42$ (592,704 atoms) is used for the MD-based GK and VC-ALD.

Disorder is created by randomly specifying the masses of the atoms on the lattice. The composition of each lattice is labeled by $m_{1-c}^i m_c^j$, where (i) $m^i = 1$ and $m^j = 3$ in LJ units for argon, and (ii) $m^i = m_{Si}$ and $m^j = 2.6m_{Si}$ for SW silicon and “heavy silicon”, which has the mass of germanium. Concentrations, c , of 0, 0.05, 0.15 and 0.5 are considered.

For LJ argon, the lattice constant at a temperature of 10 K is 5.290 Å.[87] The MD simulations were performed using LAMMPS.[136] Efficient MD codes like LAMMPS scale linearly with the number of atoms in the system, N_a , which makes the GK method (see Section 3.4) computationally-inexpensive when used with empirical potentials. An amorphous LJ phase, discussed in Section 3.3.4, was created by liquefying the crystal and instantly quenching by removing all kinetic energy. The energy of the resulting structure was minimized and then annealed in an *NPT* (constant number of atoms N , pressure P , and temperature T) ensemble at zero pressure and a temperature of 10 K. The effective zero-pressure lattice constant of the amorphous phase at this temperature, based on the atomic density, is 5.389 Å. For SW silicon, we use a lattice constant of 5.43 Å for all calculations, which brings the perfect crystal GK thermal conductivity predictions at a temperature of 300 K [83, 103] into better agreement with ALD predictions[147] compared to using the zero-pressure lattice constant.

All MD simulations are first equilibrated in a *NVT* (constant number of atoms, volume, and temperature) ensemble for 10^6 time steps. Data is then collected from simulations in the *NVE* (constant number of atoms, volume, and total energy) ensemble. For LJ argon, the potential energy is cutoff and shifted at 8.5 Å (the force is not adjusted). Time steps of 4.285 and 0.5 fs were used for the LJ argon and SW silicon simulations. The same atomic trajectories are used for the NMD and GK methods.

3.3 Vibrational Mode Properties in Alloys

3.3.1 Density of States

In this section, we begin to examine the effects of explicitly including disorder by computing the frequencies and density of states (DOS) for the vibrational modes of disordered LJ lattice supercells and their equivalent VCs. The frequencies are computed using harmonic lattice dynamics calculations with GULP.[134] For the VC, the allowed wave vectors are set by N_0 and, due to the use of the conventional unit cell, there are 12 polarization branches per wave vector. For the disordered supercells (referred to herein as Gamma), the only allowed wave vector is the gamma-point (i.e., $\kappa = 0$), where there are $12N_0^3$ polarization branches. Calculation of the Gamma modes require the eigenvalue solution of a dynamical matrix of size $(3N_a)^2$ that scales as $[(3N_a)^2]^3$, limiting the system sizes that can be considered. This eigenvalue solution is also required to perform the Gamma-NMD (see Section 3.3.3.1) and AF calculations (see Section 3.3.4).

The DOS for the VC and Gamma modes are plotted in Figs. 3.2(a), 3.2(b), and 3.2(c) for concentrations of 0.05, 0.15, and 0.5 for $N_0 = 12$ (6,912 atoms). The VC and Gamma DOS agree at low frequencies for all concentrations, where they follow the prediction of the Debye approximation that the DOS will scale as ω^2 .[130] Similar agreement between VC and Gamma DOS at low frequencies was found in DFT predictions for $\text{Si}_c\text{Ge}_{1-c}$ [39] and classical models of amorphous $\text{Si}_c\text{Ge}_{1-c}$. [148] The Debye approximation underpredicts the DOS at moderate frequency, which is due to non-linearities in the dispersion,[130] but the VC and Gamma predictions remain in good agreement.

The increasing average atomic mass with increasing concentration for the VC shifts all frequencies downward by a factor $1/[(1 - c)m^i + cm^j]^{1/2}$. The increasing average atomic mass for the Gamma modes also reduces the frequencies, but not in a systematic manner. The effect of the disorder is seen at frequencies greater than ten by a broadening and shift of the Gamma DOS to

higher frequencies because of the explicit use of light atoms in the supercell. This effect becomes more pronounced as the concentration increases. Duda et al. observed similar high-frequency broadening effects in model LJ alloys. [149] The high-frequency broadening is an indication of phonon localization, which is known to first occur at the Brillouin zone edge.[150] Based on the DOS, the vibrational modes of the explicitly disordered supercells at low frequencies are propagating, while the broadening of the DOS at high-frequency indicates that the Gamma vibrational modes may differ from the VC phonon modes in this regime. This behavior is further investigated in the next three sections.

3.3.2 Dispersion and Group Velocity

The group velocity vector in a VC is defined as the gradient of the dispersion curve,

$$\mathbf{v}_{g,\mathbf{n}}(\boldsymbol{\kappa}) = \frac{\partial \omega(\boldsymbol{\kappa})}{\partial \boldsymbol{\kappa}}. \quad (3.4)$$

We calculate the group velocities for the VC using finite differences on the frequencies calculated from harmonic lattice dynamics.[135]

For a disordered solid, the three acoustic group velocities (two transverse and one longitudinal) can be predicted using the elastic constants [134] or by finite differencing of the three lowest frequency branches of the dispersion relation of the supercell. [62, 85] Except for this low-frequency behavior, there is not an accepted method to predict the group velocity of a vibrational mode in a disordered system, although there have been attempts. [2, 62, 85, 102, 149, 151] In the Cahill-Pohl model, for example, the group velocity of all disordered modes is the sound speed, v_s , which is also assumed for the high-scatter model, Eq. (3.3). [2] This assumption is not generally valid for any material.[52, 62, 85, 102, 149, 151, 152]

Calculating the structure factors of the supercell Gamma modes is a method to test for their plane-wave character at a particular wave vector and polarization corresponding to the VC. [52,

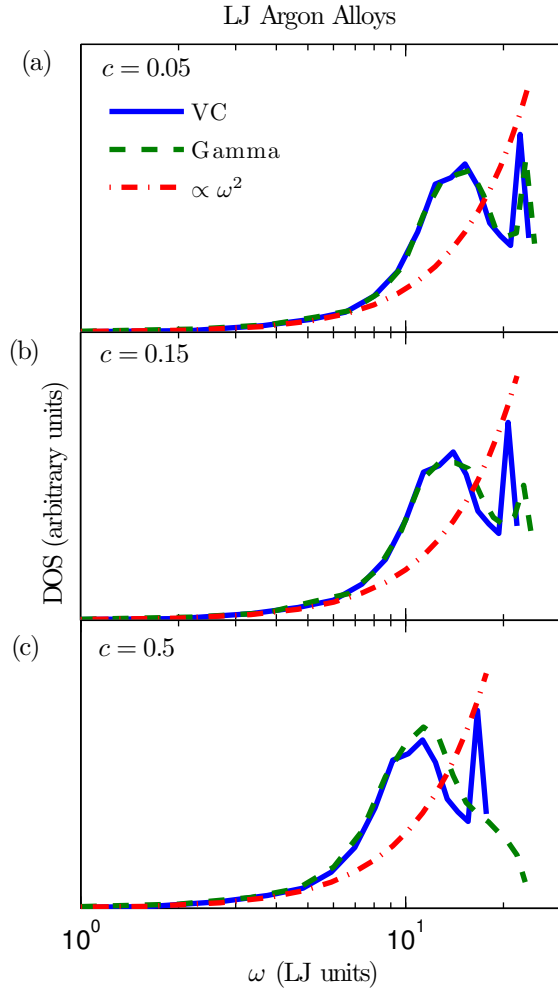


Figure 3.2: Vibrational DOS for LJ alloys calculated using the VC approximation and an explicitly disordered supercell (labeled Gamma) for concentrations of (a) 0.05, (b) 0.15, and (c) 0.5. VC and Gamma show similar low-frequency behavior for all concentrations. For increasing concentrations, the frequencies of both VC and Gamma decrease, while the high frequency DOS for Gamma spreads and reaches to a higher maximum frequency because of the explicit disorder. The supercells are of size $N_0 = 12$ (6,912 atoms).

[73] Feldman et al. used the structure factor to predict an effective dispersion for a model of amorphous silicon, but did not predict group velocities.[52] Volz and Chen used the dynamic structure factor to predict the dispersion of crystalline SW silicon using MD simulation. [153] Recently, the effective dispersion of a model disordered lattice was predicted using the structure factor. [152]

The structure factor at a VC wave vector κ_{VC} is defined as[73]

$$S^{L,T}(\kappa_{\omega}) = \sum_{\nu} E^{L,T}(\kappa_{\nu}) \delta[\omega - \omega(\kappa_{\nu}=\mathbf{0})], \quad (3.5)$$

where the summation is over the Gamma modes, E^T refers to the transverse polarization and is defined as

$$E^L(\kappa_{\nu}) = \left| \sum_b \hat{\kappa}_{VC} \cdot e(\kappa_{\nu}=\mathbf{0} \ b) \exp[i\kappa_{VC} \cdot \mathbf{r}_0(l=0)] \right|^2 \quad (3.6)$$

and E^L refers to the longitudinal polarization and is defined as

$$E^T(\kappa_{\nu}) = \left| \sum_b \hat{\kappa}_{VC} \times e(\kappa_{\nu}=\mathbf{0} \ b) \exp[i\kappa_{VC} \cdot \mathbf{r}_0(l=0)] \right|^2. \quad (3.7)$$

In Eqs. (4.13) and (4.14), the b summations are over the atoms in the disordered supercell, $\mathbf{r}_0(l=0)$ refers to the equilibrium atomic position of atom b in the supercell, l labels the unit cells ($l = 0$ for the supercell), α labels the Cartesian coordinates, and $\hat{\kappa}_{VC}$ is a unit vector. Explicit disorder is included in the Gamma frequencies $\omega(\kappa_{\nu}=\mathbf{0})$ and the $3N_a$ components of the eigenvectors, $e(\kappa_{\nu}=\mathbf{0} \ b)$.

Physically, $S^{L,T}(\kappa)$ represents the frequency spectrum required to create a wavepacket with a well-defined wave vector and polarization. [52, 73, 154] For a perfect lattice, the structure factor peaks are delta functions centered at the mode frequencies, indicating that the modes are pure plane-waves (i.e., phonons). A sampling of the structure factors for the LJ argon alloys are plotted in Fig. 3.3 for wave vectors along the [100] and [111] directions in the $N_0 = 10$ systems.

* Well-defined peaks at all wave vectors are due to the lattice structure of the disordered systems. Typically, the structure factor for amorphous materials has well-defined peaks only for small wave vector.[52, 73] With increasing disorder, the structure factor spreads in width, particularly at high frequencies, which is an indication that the modes are not pure plane waves.

From Fig. 3.3, an effective dispersion curve (middle panels) can be extracted by locating the peaks in the structure factors at neighboring VC wave vectors. The peaks in the structure factor are larger than the VC predicted frequencies (plotted as solid lines in Fig. 3.3) by at most 5%. Similar agreement is found with the disordered SW silicon lattice supercells.

Even though there is good agreement between the VC-predicted dispersion curves and the peaks in the structure factors from Fig. 3.3, the effect of the width of the peaks is not clear. We will use the group velocities predicted by the VC dispersion for both LJ argon and SW silicon in the VC-NMD and VC-ALD calculations for consistency and simplicity. The validity of this group velocity choice will be discussed in Section 3.3.5.

3.3.3 Lifetimes

3.3.3.1 From VC-NMD and Gamma-NMD

Once the group velocities are predicted using the VC dispersion, the mode lifetimes are required to predict the thermal conductivity using Eq. (3.1). As an alternative to the VC-ALD approach for predicting lifetimes, which is discussed in the next section, we first use the MD simulation-based NMD method.[81, 99, 111, 155] In NMD, the atomic trajectories are first mapped onto the vibrational mode coordinate $q(\kappa; t)$ and its time derivative $\dot{q}(\kappa; t)$ by [19]

$$q(\kappa; t) = \sum_{\alpha, b, l}^{3, n, N} \sqrt{\frac{m_b}{N}} u_\alpha(b; t) e^*(\kappa \cdot \alpha) \exp[i\kappa \cdot \mathbf{r}_0(l)] \quad (3.8)$$

*Due to the finite-size system, the delta function in Eq. (4.12) is broadened using a Lorentzian function with a full-width at half maximum set to $20\delta_{\omega, avg}$, where $\delta_{\omega, avg}$ is the average frequency spacing. [48].

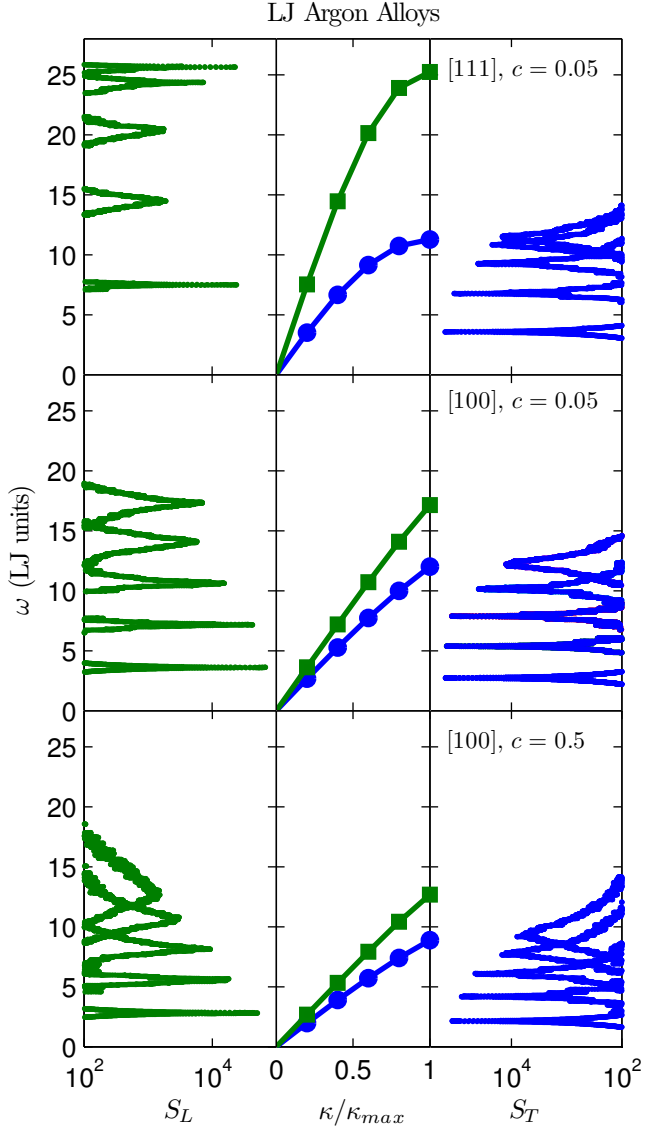


Figure 3.3: Left and right panels: The structure factor for longitudinal (S_L) and transverse (S_T) polarizations along high-symmetry directions of the mass disordered LJ argon supercells ($N_0 = 10$, $c = 0.05, 0.5$). Center panels: The VC predicted dispersion curves (solid lines) agree well with the locations of the peaks in S_L and S_T (data points). The wavenumber axis in the center panel is normalized by the maximum value of the wavenumber in the given direction.

and

$$\dot{q}(\boldsymbol{\kappa}; t) = \sum_{\alpha, b, l}^{3, n, N} \sqrt{\frac{m_b}{N}} \dot{u}_\alpha(b; t) e^*(\boldsymbol{\kappa}_\alpha^b) \exp[i\boldsymbol{\kappa} \cdot \mathbf{r}_0(l)]. \quad (3.9)$$

Here, m_b is the mass of the b_{th} atom in the unit cell, u_α is the α -component of the atomic displacement from equilibrium, \dot{u}_α is the α -component of the atomic velocity, and t is time.

The total energy of each vibrational mode, $E(\boldsymbol{\kappa}; t)$, is calculated from

$$E(\boldsymbol{\kappa}; t) = \frac{\omega(\boldsymbol{\kappa})^2}{2} q(\boldsymbol{\kappa}; t)^* q(\boldsymbol{\kappa}; t) + \frac{1}{2} \dot{q}(\boldsymbol{\kappa}; t)^* \dot{q}(\boldsymbol{\kappa}; t). \quad (3.10)$$

The vibrational mode lifetime is predicted using

$$\tau(\boldsymbol{\kappa}) = \int_0^{t^*} \frac{\langle E(\boldsymbol{\kappa}; t) E(\boldsymbol{\kappa}; 0) \rangle}{\langle E(\boldsymbol{\kappa}; 0) E(\boldsymbol{\kappa}; 0) \rangle} dt, \quad (3.11)$$

where the upper integration limit t^* is set to be much larger than the mode lifetime and the brackets indicate an ensemble average.[155] The NMD calculations scale as $(N_a)^2$.[12]

We perform the MD simulations using the fully disordered supercells and project onto the frequencies and eigenvectors from both the VC unit cell [$\omega(\boldsymbol{\kappa})$, $e(\boldsymbol{\kappa}_\alpha^b)$] and the Gamma supercell [$\omega(\boldsymbol{\kappa}=0)$, $e(\boldsymbol{\kappa}=0_\alpha^b)$]. Previous studies of disordered supercells with the NMD method have used the Gamma modes only to perform the projections. [62, 83, 84, 102, 151] The trajectories from the MD simulations are also used in the GK method calculations (Section 3.4). The MD simulations were ten times longer than the longest lifetime in the system, which was estimated from the VC-ALD predicted lifetimes. For LJ argon and SW silicon, data was collected for 2^{20} and 2^{22} time steps and the atomic trajectories were sampled every 2^8 and 2^4 time steps. Ensemble averaging of the energy autocorrelations was performed using ten independent, initially-randomized velocity distributions.

For the normal modes of the lattice supercell, where the energy autocorrelation follows an

exponential decay,[99, 111] Eq. (3.11) is exact, but this expression becomes an approximation when using the VC normal modes to perform the mappings in Eqs. (3.8) and (4.19). Even for larger disorder ($c = 0.5$), where the energy autocorrelations deviate from an exponential decay, an effective lifetime can still be predicted using Eq. (3.11) (see Appendix A.4). The lifetimes predicted using VC-NMD and Gamma-NMD are shown in Figs. 3.4(a)-3.4(d) for the LJ argon crystal and all alloys at a temperature of 10 K. The range of frequencies for VC-NMD and Gamma-NMD differ slightly due to differences in the DOS (see Fig. 3.2). For a small interval of frequency, there is a wider range of predicted lifetimes for Gamma-NMD. This spread is because there is no symmetry-averaging of the mode properties, which is possible for the VC by considering the crystal lattice's irreducible Brillouin zone.[130]

The lifetimes predicted by both VC-NMD and Gamma-NMD show a ω^{-2} scaling at low frequency and a ω^{-4} scaling (for the alloys) and even faster for mid-range frequencies. The ω^{-2} scaling is due to three-phonon scattering processes [21, 124]. The ω^{-4} scaling is due to phonon-mass point defect scattering.[23, 35, 90, 91] A constant lifetime is observed at the highest frequencies for both VC-NMD and Gamma-NMD except at $c = 0.5$ for VC-NMD. We are not aware of any theoretical prediction of this high-frequency behavior.

The majority of the lifetimes predicted by both VC-NMD and Gamma-NMD are larger than the Ioffe-Regel (IR) limit, [75]

$$\tau_{IR} = \frac{2\pi}{\omega}. \quad (3.12)$$

The physical interpretation of the IR limit is a mode that scatters in a time equal to its oscillation period. Our results suggest that the IR limit is a good lower-limit for the lifetimes predicted by VC-NMD and Gamma-NMD for LJ argon (Fig. 3.4) and VC-NMD for SW silicon [see Fig. 3.8(a) in Section 3.5].

Overall, good agreement is seen in the predicted lifetimes from VC-NMD and Gamma-NMD in both magnitude and trends. The use of the VC normal modes is an approximation that becomes worse as the concentration is increased (see Appendix A.4), but our results suggest that

the effect is only pronounced at the highest frequencies and at high alloy concentrations. The only approximation associated with Gamma-NMD is the use of the harmonic lattice dynamics-predicted frequencies and eigenvectors to map the atomic trajectories from the fully anharmonic MD simulations. This assumption has been shown to be valid for LJ argon below temperatures of 40 K.[111] Based on the good agreement with Gamma-NMD, the VC-NMD lifetimes are used along with the VC group velocities to predict thermal conductivity in Section 3.4. For Gamma-NMD, there is no accepted way to predict the mode group velocities, so that the thermal conductivity cannot be predicted using Eq. (3.1).

3.3.3.2 From VC-ALD

Under the VC approximation, the ALD calculations[111] are performed on the conventional unit cells of LJ argon and SW silicon with a single atomic mass based on the alloy concentration. The ALD calculations scale as $b^4(N_0)^2$.[12] Disorder is not included explicitly but is treated using perturbation theory. Assuming phonon scattering mechanisms to operate independently, the effective phonon lifetime can be found using the Matthiessen rule, [20]

$$\frac{1}{\tau(\kappa)} = \frac{1}{\tau_{p-p}(\kappa)} + \frac{1}{\tau_{p-d}(\kappa)}, \quad (3.13)$$

where $\tau_{p-p}(\kappa)$ accounts for intrinsic phonon-phonon scattering and $\tau_{p-d}(\kappa)$ accounts for phonon-defect scattering.

Phonon-phonon scattering in ALD is modeled by including three-phonon processes.[37, 39, 111] The present study is concerned with temperatures much less than the melting temperature of either LJ argon [87] or SW silicon[131] so that we believe the effects of higher-order phonon processes are negligible.[111, 156] We predict the phonon-phonon lifetimes using the method described in Ref. 111, with all classical expressions for the populations to remain consistent with the classical MD-based methods from Section 3.3.3.1.

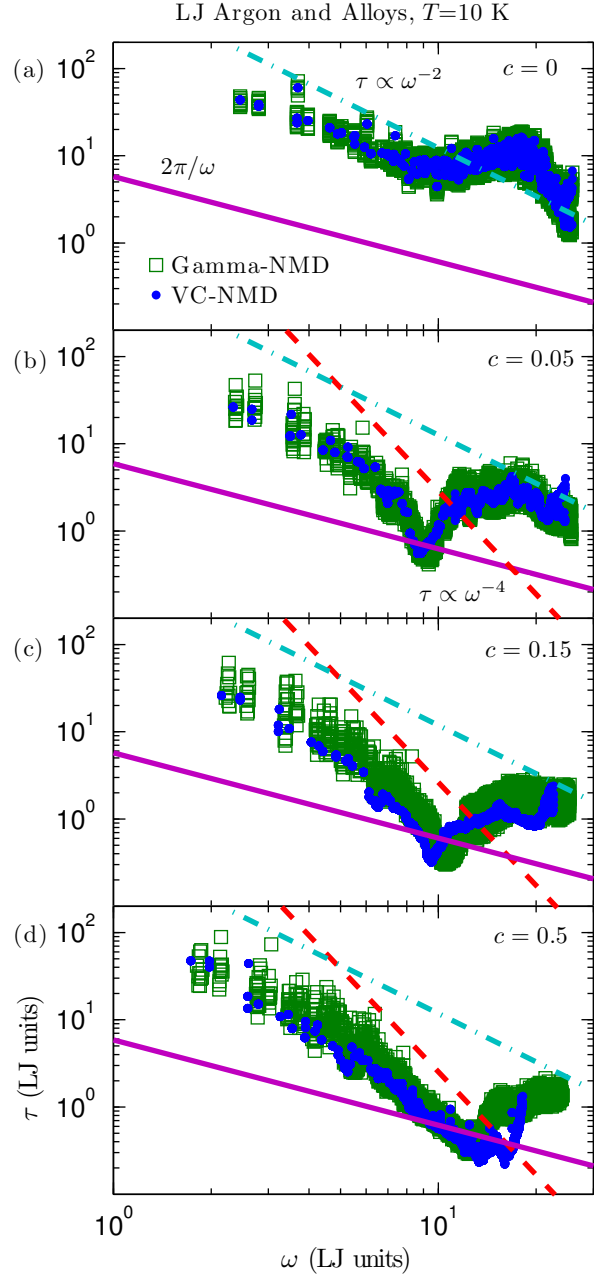


Figure 3.4: Lifetimes predicted using VC-NMD and Gamma-NMD from MD simulations of (a) perfect LJ argon and (b),(c),(d) mass-disordered LJ alloys for $N_0 = 10$. ω^{-2} and ω^{-4} scalings are observed at low to mid frequencies. For both VC-NMD and Gamma-NMD, most mode lifetimes are greater than the Ioffe-Regel limit of $2\pi/\omega$. [75] While there is more scatter in the Gamma-NMD data (see Section 3.3.3.1), the lifetime magnitudes and trends agree well, an important consideration when comparing the VC-NMD and VC-ALD lifetimes in Fig. 3.5(a).

Using perturbation theory, Tamura derived a general expression for phonon scattering by mass point defects to second order that was applied to study isotopic germanium.[35] By considering the symmetry properties of the FCC lattices considered in this work, his expression reduces to

$$\frac{1}{\tau_{p-d}(\kappa)} = \frac{\pi}{2} g_2 \omega^2(\kappa) DOS[\omega(\kappa)], \quad (3.14)$$

where

$$g_n = \sum_{\mu} c^{\mu} (1 - m^{\mu}/\bar{m}^{\mu})^n. \quad (3.15)$$

Here, c^{μ} and m^{μ} are the concentration and mass of the μ -th species and \bar{m}^{μ} is the average mass. Bond disorder can be accounted for using a similar expression with an average atomic radius or suitable scattering cross-section. [23, 90] For the binary LJ argon and SW silicon alloys considered here, there is one atom type in the unit cell with $\mu = i, j$, so that the alloying atom labeled by m_c^j can be considered to be an “isotope” of the atom labeled m_{1-c}^i .

The lifetimes predicted by VC-ALD for LJ argon at a concentration of 0.05 are plotted in Fig. 3.5(a). [†] Also plotted are the lifetimes for the perfect system and from the VC-NMD predictions [Fig. 3.4(b)] at this concentration. At low frequencies, where the DOS is Debye-like [$D(\omega) \propto \omega^2$, Fig. 3.2], $\tau_{p-p}(\kappa)$ scales as ω^{-2} , a scaling also observed in the VC-NMD and Gamma-NMD lifetimes. Under the Debye-approximation, the phonon scattering due to mass point-defects is predicted to scale as ω^{-4} from Eq. (3.14). [35, 91] This scaling is observed in the VC-NMD, Gamma-NMD, and VC-ALD predicted lifetimes in the mid-frequency range. VC-ALD does not predict the frequency-independent lifetimes at high frequency for LJ argon observed in VC-NMD and Gamma-NMD, and a significant number fall below the IR limit. The

[†]To perform the calculation of Eq. (3.14), it is necessary to broaden the DOS using a Lorentzian function. [35] We use a value of $100\delta_{\omega,avg}$.

lifetimes predicted by NMD and ALD for the perfect LJ argon crystal agree within 20% on a mode-by-mode basis, and the resulting thermal conductivities agree within their uncertainties (see Table 3.1).

Tamura applied his theory to predict the reduction of lifetimes in isotopic germanium, which is weakly disordered ($\sim 5\%$ variation in the atomic masses). In the LJ alloys, the masses differ by a factor of three. Large mass ratios were also considered in DFT VC-ALD studies of SiGe (mass ratio of 2.6)[39], PbTeSe (2.6)[37], and MgSiSn (4.9)[38]. The importance of higher-order interactions in the Tamura theory can be estimated by the disorder strength (i.e., g_n for $n > 2$).[35] For isotopically-disordered germanium, Tamura estimated that the higher-order contributions were negligible ($g_2 = 5.87 \times 10^{-4}$, $g_3 \sim 10^{-7}$, and $g_4 \sim 10^{-7}$).[35] For LJ argon at a concentration of 0.15, $g_2 = 0.3018$, $g_3 = -0.3250$ and $g_4 = 0.4411$. It is possible that the neglect of the higher-order interactions in the Tamura theory is responsible for the discrepancy of the lifetimes predicted by VC-NMD and Gamma-NMD versus VC-ALD at high frequencies. Full evaluation of the higher-order interactions in the Tamura theory is of similar complexity to anharmonic phonon interaction, [111, 124, 156] and is beyond the scope of this work.

3.3.4 Diffusivities

We now use the AF theory to provide a lower limit for the contribution of a given vibrational mode to thermal conductivity. While studies have been performed on alloying the amorphous phase, [48] the AF theory has not been previously applied to disordered lattices. In the classical, harmonic limit for specific heat, a mode's contribution to the thermal conductivity is determined by its diffusivity,

$$D_{ph,\mathbf{n}}(\boldsymbol{\nu}) = v_{g,\mathbf{n}}^2(\boldsymbol{\nu}) \tau(\boldsymbol{\nu}), \quad (3.16)$$

such that from Eq. (3.1)

$$k_{ph,\mathbf{n}} = \sum_{\boldsymbol{\kappa}} \sum_{\boldsymbol{\nu}} \frac{k_B}{V} D_{ph,\mathbf{n}}(\boldsymbol{\nu}). \quad (3.17)$$

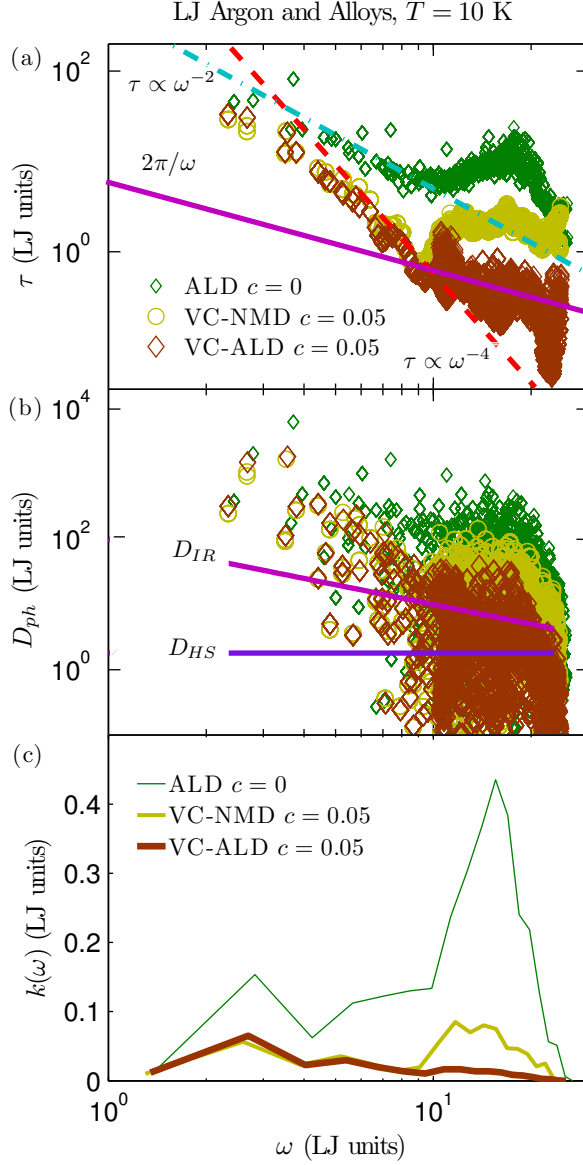


Figure 3.5: (a) Predicted lifetimes using VC-NMD and VC-ALD for LJ argon ($T = 10$ K, $N_0 = 10$, and $c = 0.05$). (b) Mode diffusivities compared to the high-scatter limit, D_{HS} [Eq. (3.18)], and IR limit, D_{IR} [Eq. (3.19)]. VC-NMD and VC-ALD predict a large number of high-frequency modes with $D_{ph} < D_{HS}$. (c) Thermal conductivity frequency spectrum, which peaks at high frequency, in contrast to SW silicon [(Fig. 3.8(c))].

The lower limit for phonon diffusivity is zero since the group velocities can be zero (e.g., optical modes at the Brillouin zone center).

In the high-scatter limit,[2] the diffusivity of each mode is

$$D_{HS} = \frac{1}{3}v_s a, \quad (3.18)$$

which leads to Eq. (3.3). The physical interpretation of Eq. (3.18) is that all vibrational modes transport heat at the sound speed and have a mean free path of the lattice spacing. Based on the IR limit, another possible lower-bound of diffusivity is

$$D_{IR} = \frac{2\pi}{3} \frac{v_s^2}{\omega}. \quad (3.19)$$

To evaluate Eqs. (3.18) and (3.19), the sound speed is estimated by

$$v_s = \frac{1}{3}v_{s,L} + \frac{2}{3}v_{s,T}, \quad (3.20)$$

where $v_{s,L}$ and $v_{s,T}$ are the longitudinal and transverse sound speeds calculated from the elastic constants, [134] which agree within 20% with the branch-averaged sound speeds along the high-symmetry dispersion directions [100],[110], and [111]. For LJ argon and SW silicon, $v_s = 6.93$ (LJ units) and 5,790 m/s. The Cahill-Pohl model assumes Eq. (3.19) for the mode diffusivities.[2] As seen in Fig. 3.5(b) for the LJ argon alloy at a concentration of 0.05, VC-NMD and VC-ALD predict [from Eq. (3.16), using the x -component of group velocity], a significant number of modes with $D_{ph}(\kappa)$ less than D_{HS} , and D_{IR} approaches D_{HS} at high frequencies. For both VC-NMD and VC-ALD, we approximate $\mathbf{v}_{g,n}(\kappa)$ from the VC dispersion (Section 3.3.2) so that any differences in diffusivity D_{ph} will come from the predicted lifetimes.

In a disordered system, modes can transport heat by harmonic coupling in the AF theory of diffusons.[47] While the high-scatter model assumes a mode-independent diffusivity, the AF

theory is capable of predicting mode-specific thermal diffusivities D_{AF} . [48, 52, 157] Since the AF theory is harmonic, the diffusivities typically diverge as the frequency approaches zero because these vibrations are long-wavelength plane waves that are weakly scattered by the disorder. [94, 95] The mode-specific diffusivities, D_{AF} , of an LJ argon amorphous phase (see Section 4.3) [‡] are plotted in Fig. 3.6 along with D_{HS} and D_{IR} . Except at the highest frequencies, the diffusivity of all amorphous modes can be approximated using the mode-independent diffusivity D_{HS} . The lower-limit D_{IR} is clearly an overprediction for the amorphous mode diffusivities. Also plotted in Fig. 3.6 are diffusivities predicted from the AF theory for the explicitly-disordered LJ argon lattice supercell alloy at a concentration of 0.5. As expected, the AF theory predictions diverge at low frequency. [§] The diffusivity of all modes are larger than D_{HS} except at the highest frequencies, where they tend to zero as with the amorphous phase. This result supports the hypothesis that the lower-bound of the VC predicted phonon diffusivity should be D_{HS} (and not zero as for a crystal), which is further explored in Sections 3.4 and 3.5.

3.3.5 Discussion

In this section, in anticipation of the thermal conductivity predictions in Section 3.4, we discuss two possible sources of error in the VC-predicted mode properties. To start, we note that for disordered systems, it is generally only possible to assign a unique lifetime and group velocity to vibrational modes in the low-frequency, propagating limit. [52, 158] The mode diffusivity is the fundamental transport property. [47, 48, 52]

We believe that the VC-predicted group velocities, particularly for $v_{g,n}(\kappa) \approx 0$, are an underprediction of the velocity scale required to evaluate Eq. (3.16). This statement is supported by the AF-theory diffusivities plotted in Fig. 3.6, which are finite for the majority of the frequency

[‡]For a finite system, the AF theory requires a frequency broadening to predict the mode-specific thermal diffusivities. [47] We broaden using a Lorentzian function with a width $\delta_{\omega,avg}$.

[§]For the LJ alloys with $c \leq 0.15$, the predicted k_{AF} is strongly system-size dependent, indicating this diverging behavior. For LJ argon alloys at $c = 0.5$, the divergence with system size is small for the range of system size studied ($N_0 = 4$ to $N_0 = 12$). For $N_0 = 12$, $k_{AF}/k_{GK} = 0.93$ because the finite system-size limits the diffusivities of the lowest frequencies.

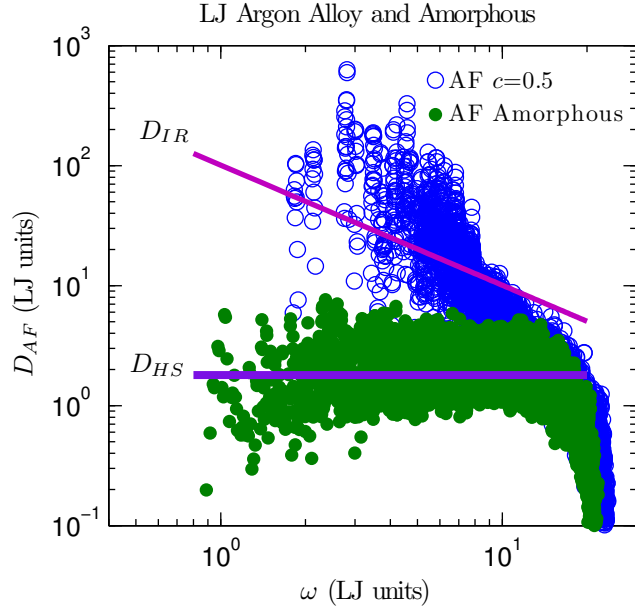


Figure 3.6: AF theory predictions of disordered mode diffusivities for LJ argon alloy and amorphous phases. The amorphous phase is well-described by a mode-independent diffusivity D_{HS} [Eq. (3.18)]. The system size for the alloy is $N_0 = 10$ (6,912 atoms), and the amorphous phase has 6,912 atoms.

range the LJ alloy at a concentration of 0.5. While the diffusivity from Eq. (3.16) can be zero because of the VC predicted group velocities, this result is not consistent with the AF theory predictions.

The VC-NMD and Gamma-NMD predicted lifetimes are generally larger than the IR limit for LJ argon and its alloys (see Fig. 3.4). The constant lifetime observed at the highest frequencies for both VC-NMD (except at $c = 0.5$) and Gamma-NMD is consistent with the plateau of mode diffusivity at high frequency predicted for a model disordered lattice, which was explained by a plateau in the vibrational mode lifetimes. [93] Recently, a study of model disordered lattices predicted the mid-frequency minimum and the high-frequency plateau of the mode diffusivities.[152] Similar behavior of the mode diffusivities has been observed in model jammed systems.[95, 158] VC-ALD predicts essentially monotonically decreasing lifetimes with increasing frequency for the LJ argon alloys [Fig. 3.5(a)] with many falling below the IR limit. Because VC-NMD and VC-ALD use the same values for $v_{g,n}(\kappa_\nu)$, the mode diffusivities will therefore

be underpredicted for VC-ALD compared to VC-NMD for the LJ argon alloys because of the lifetime underprediction.

3.4 Thermal Conductivity Prediction

The thermal conductivities of the LJ systems can now be predicted from Eq. (3.1) using the vibrational mode properties from VC-NMD and VC-ALD. Given the discussion regarding the VC-predicted mode properties in Section 3.3.5, we also predict thermal conductivity using the equilibrium MD-based GK method, which is a top-down method that does not make any approximations about the nature of the vibrational modes. Thermal conductivities predicted by the GK method naturally capture all scattering mechanisms. [77, 83, 85] The heat current was computed every ten time steps from the same atomic trajectories (positions and velocities) used for the VC-NMD and Gamma-NMD calculations. The thermal conductivity is determined from the maximum of the integral of the heat current autocorrelation function.

The thermal conductivities predicted by VC-NMD, VC-ALD, and GK are system size-dependent [i.e., $k = k(N_0)$] for all lattices and methods except perfect LJ argon from GK.[81] To predict a bulk thermal conductivity, k_{bulk} , a linear extrapolation procedure is used, whereby

$$\frac{k(N_0)}{k_{bulk}} = 1 - \frac{c_0}{N_0}, \quad (3.21)$$

where c_0 is a constant.[12, 29, 36] The thermal conductivity is predicted for varying system sizes and the bulk thermal conductivity is obtained by fitting Eq. (3.21) to the data. For VC-NMD and VC-ALD, the validity of Eq. (3.21) requires that the low-frequency modes be dominated by phonon-phonon scattering (i.e., $\tau \propto \omega^{-2}$) and follow the Debye approximation with respect to the group velocity and DOS. [29, 36] For the LJ argon alloys, this requirement is satisfied for modest system sizes (for $N_0 = 6$ to 12) so that both VC-NMD and VC-ALD thermal conductivity predictions can be extrapolated to a bulk value.

Bulk thermal conductivity predictions for the LJ argon alloys using VC-NMD, VC-ALD, and GK are tabulated in Table 3.1 and plotted in Fig. 3.7. Also plotted in Fig. 3.7 is the high-scatter thermal conductivity prediction k_{HS} [Eq. (3.3)]. The thermal conductivity predicted for the LJ amorphous phase by GK is 0.17 W/m-K, which is in good agreement with k_{HS} (0.16 W/m-K) for the perfect crystal. The predicted thermal conductivities of the LJ argon alloys at high concentration are a factor of two to three larger than k_{HS} . While agreement between the three methods is found for the perfect crystal, VC-NMD and VC-ALD underpredict the alloy thermal conductivities compared to GK. The underprediction is modest for VC-NMD, where k_{NMD} is 80% of k_{GK} or greater for all concentrations. The VC-ALD method significantly underpredicts the thermal conductivity of the LJ argon alloys. The largest deviation is at a concentration of 0.05, where k_{VC-ALD} is 56% of k_{GK} .

In Section 3.3.4, we argued for the existence of a minimum mode diffusivity, D_{HS} [Eq. (3.18)]. As shown in Fig. 3.5(b), the diffusivities of many high-frequency modes in the LJ alloys, predicted by both VC-NMD and VC-ALD, fall below this limit. Based on this observation, we propose that any diffusivity below the limit be set to D_{HS} for thermal conductivity prediction. The results of this adjustment, referred to as VC-NMD* and VC-ALD*, are plotted in Fig. 3.7 and included in Table 3.1. The adjusted thermal conductivities predicted by VC-NMD* are now within 10% of the GK value for all concentrations, which is within the prediction uncertainties. Combined with D_{HS} , we believe that the VC-NMD predicted diffusivities are good representations for the explicitly-disordered modes present in the MD simulations. Another possible adjustment, D_{IR} [Eq. (3.19)], results in a thermal conductivity of 0.94 ± 0.09 W/m-K for the LJ argon alloy at a concentration of 0.05, well above the value predicted by GK. We also note that the thermal conductivity of the amorphous phase is well-modeled by a mode-independent diffusivity D_{HS} , while D_{IR} overpredicts for all modes in the amorphous phase (see Fig. 3.6). Thus, we believe that D_{HS} is the more appropriate high-scatter limit.

By applying the high-scatter limit adjustment VC-ALD*, the thermal conductivities are brought

into marginally better agreement with the GK values, worst for a concentration of 0.05, where k_{VC-ALD^*} is 65% of k_{GK} . As seen in Fig. 3.5(b), the VC-ALD method fails to accurately predict the high-frequency mode diffusivities for LJ argon alloys. Since the group velocities are the same for VC-NMD and VC-ALD, the underprediction of the high-frequency diffusivities is due to the underprediction of the high-frequency mode lifetimes from VC-ALD compared to VC-NMD. We know that the VC-NMD predicted lifetimes are more accurate values due to their agreement with Gamma-NMD [Fig. 3.4].

The thermal conductivity spectrum, defined as the contribution to thermal conductivity of modes at a given frequency, is plotted in Fig. 3.5(c) for VC-NMD and VC-ALD for the perfect crystal and the alloy with a concentration of 0.05. The thermal conductivity of LJ argon and its alloys has important contributions from high-frequency modes. VC-ALD underpredicts the high-frequency diffusivities compared to VC-NMD, which leads to an underprediction of the high-frequency thermal conductivity spectrum compared to VC-NMD. This result can be traced back to an underprediction of the high-frequency lifetimes compared to VC-NMD and Gamma-NMD [Fig. 3.5(a)].

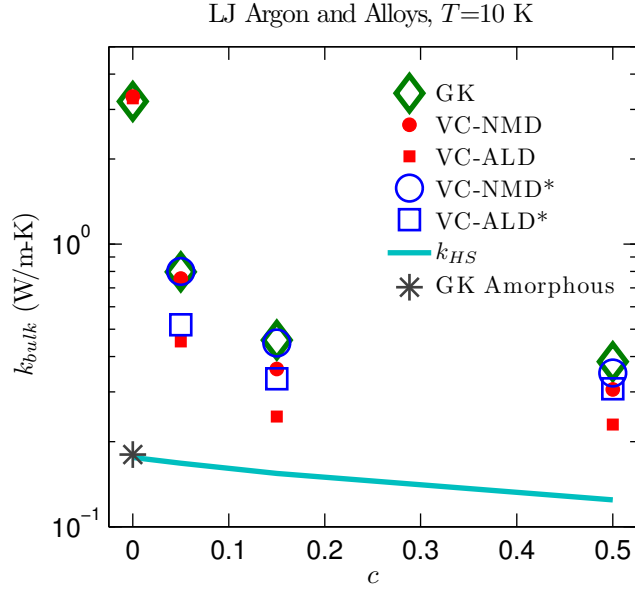


Figure 3.7: Thermal conductivity predictions for LJ argon and alloys at $T=10$ K using the VC-NMD, VC-ALD, and GK methods. The high-scatter thermal conductivity prediction k_{HS} [Eq. (3.3)] and the high-scatter adjusted VC-NMD* and VC-ALD* are also plotted.

Table 3.1: Thermal conductivity predictions using the VC-NMD, VC-ALD, and GK methods. For LJ argon alloys, the bulk extrapolation is used for all three methods. For SW silicon alloys, only VC-ALD and GK can be used to extrapolate a bulk thermal conductivity (see Section 3.4). For VC-NMD and GK, the uncertainties are estimated by omitting independent simulations from the ensemble averaging (see Section 4.3). For VC-ALD, the uncertainties are estimated by omitting extrapolation points used for Eq. (3.21).

c	GK	VC-NMD	VC-ALD	VC-NMD*	VC-ALD*
LJ					
0.00	3.3 ± 0.1	3.3 ± 0.1	3.4 ± 0.1	-	-
0.05	0.80 ± 0.07	0.76 ± 0.07	0.45 ± 0.02	0.80 ± 0.1	0.52 ± 0.05
0.15	0.46 ± 0.07	0.36 ± 0.04	0.24 ± 0.01	0.45 ± 0.05	0.33 ± 0.07
0.50	0.38 ± 0.07	0.31 ± 0.04	0.23 ± 0.01	0.35 ± 0.05	0.31 ± 0.07
SW					
0.00	520 ± 30	-	480 ± 20	-	-
0.05	20 ± 2	-	24 ± 2	-	24 ± 2
0.15	9.9 ± 0.9	-	12 ± 1	-	12 ± 1
0.50	9.3 ± 0.9	-	11 ± 1	-	11 ± 1

3.5 SW silicon

The failure of VC-ALD to predict the thermal conductivities of the LJ alloys is due to an under-prediction of the high-frequency mode lifetimes, which make an important contribution to the thermal conductivity [see Sections 3.3.4 and 3.4, Figs. 3.5(a) and 3.5(c)]. To provide a contrast, we now predict the vibrational mode properties and thermal conductivity for bulk and alloyed SW silicon, where it is known that low-frequency modes dominate the thermal conductivity. [123, 147] The lifetimes for the perfect crystal and an alloy with a concentration of 0.5 predicted by VC-NMD and VC-ALD are plotted in Fig. 3.8(a). The VC-NMD predicted lifetimes are generally larger than the IR limit for SW silicon alloys, similar to the VC-NMD predictions for the LJ argon alloys (Fig. 3.4). Unlike the LJ argon alloys, the VC-NMD and VC-ALD predicted lifetimes agree over most of the frequency spectrum, except at the highest frequencies, where VC-ALD underpredicts VC-NMD and falls below the IR limit. The high-frequency plateau of the VC-NMD predicted lifetimes for LJ argon (Fig. 3.4) is not seen for SW silicon. As seen in Figs. 3.5(b) and 3.8(b), VC-NMD and VC-ALD both predict a significant number of modes with $D_{ph}(\kappa)$ less than D_{HS} for both the LJ argon and SW silicon alloys.

The thermal conductivity spectra for bulk SW silicon and an alloy with a concentration of 0.5 are plotted in Fig. 3.8(c). For bulk and the alloy, the thermal conductivity is dominated by low-frequency modes, so that large system-sizes are needed to satisfy the extrapolation requirements and only GK and VC-ALD can be used to predict a bulk value from Eq. (3.21). While a previous study found that it was necessary to use cell sizes of $N_0 = 60$ for Tersoff silicon alloys,[84] we find that Eq. (3.21) is valid for SW silicon and $38 \leq N_0 \leq 42$. This system-size requirement highlights the efficiency of the VC-ALD method compared to VC-NMD, which is necessary when computationally-expensive DFT calculations are used. [29, 30, 37, 39, 92, 159] The bulk thermal conductivity predictions for VC-ALD and GK are shown in Table 3.1 and plotted in Fig. 3.9. The alloy thermal conductivities predicted by VC-ALD are 20% larger than those from GK, in contrast to VC-ALD underpredicting for LJ argon alloys. This overprediction by VC-ALD

compared to GK is close to the overprediction (15%) of VC-ALD using DFT calculations of SiGe alloys compared to experiment without including disorder explicitly.[39]

The predicted thermal conductivities for the SW silicon alloys at all concentrations are over an order of magnitude larger than the high-scatter prediction, k_{HS} . Because the thermal transport in SW silicon is dominated by low-frequency modes, the high-scatter adjustment VC-ALD* is within one percent compared to the unadjusted VC-ALD. While higher-order interactions in the Tamura theory may be responsible for the discrepancy of the lifetimes predicted by VC-NMD and VC-ALD in SW silicon at the highest frequencies [Fig. 3.8(a)], this effect is not important to the overall thermal transport. VC-ALD predicts accurate alloy thermal conductivities for SW silicon because it is a low-frequency dominated material, which is the frequency range where the standard application of the Tamura theory is valid.[35]

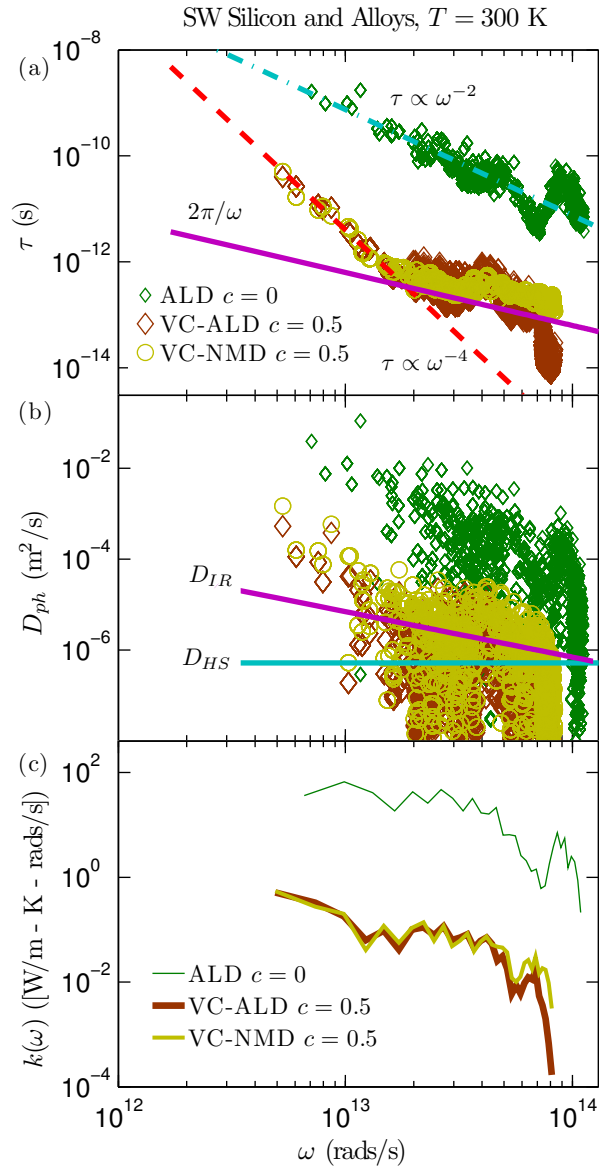


Figure 3.8: (a) Predicted lifetimes using VC-NMD and VC-ALD for SW silicon ($T = 300$ K, $N_0 = 8$, and $c = 0.05$). (b) Mode diffusivities compared to the high-scatter limit, D_{HS} [Eq. (3.18)], and the IR limit, D_{IR} [Eq. (3.19)]. VC-NMD and VC-ALD predict a large number of high-frequency modes with $D_{ph} < D_{HS}$, as seen in the LJ argon alloys [Fig. 3.5(b)]. (c) Thermal conductivity frequency spectra, which peak at low frequency, in contrast to LJ argon [Fig. 3.5(c)].

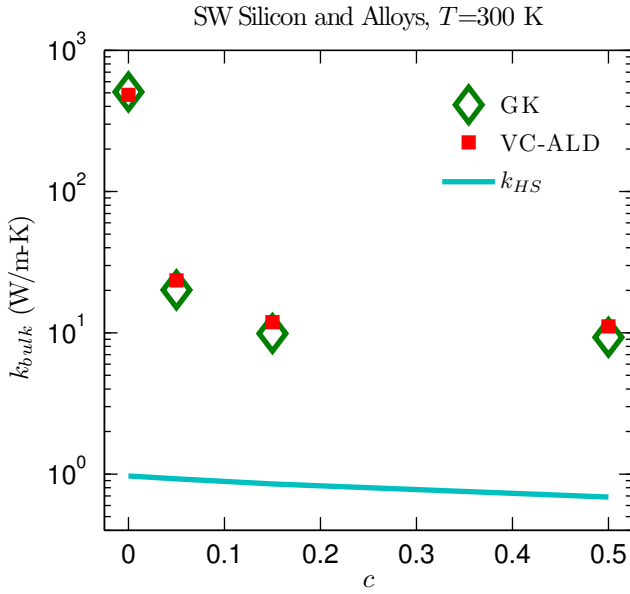


Figure 3.9: Thermal conductivity predictions for SW silicon and alloys at a temperature of 300 K using the VC-ALD and GK methods. The high-scatter thermal conductivity prediction k_{HS} is also plotted. The adjusted VC-ALD* is not shown since it differs by less than one percent compared to VC-ALD.

3.6 Summary

In this study, we investigated the use of the VC approximation for predicting the vibrational mode properties and thermal conductivity of LJ argon and SW silicon alloys by a detailed comparison of the VC-NMD, VC-ALD, and GK methods. By using computationally-inexpensive empirical potentials we self-consistently studied the effects of disorder both explicitly (Sections 3.3.1, 3.3.2, 3.3.3.1, 3.3.4, and 3.5) and as a perturbation (Sections 3.3.3.2 and 3.5). By spanning a range of disorder, the limits of the perturbative models were examined. A breakdown of the VC-ALD method was identified for LJ argon alloys by a comparison with the VC-NMD method in Section 3.3.3.2 and a correction was suggested in Section 3.4. The mode properties and thermal conductivity of the SW silicon alloys were predicted in Section 3.5 and provided a contrast to the LJ argon alloys, which have a different thermal conductivity spectrum.

The results for the SW silicon and LJ argon alloys suggest that modeling of thermal transport

in ordered and disordered lattices can be separated into two broad groups: low-frequency dominated and full-spectrum materials. Materials dominated by low-frequency modes tend to have high thermal conductivities that are significantly larger than the high-scatter limit [Eq. (3.3)], which is due to the large group velocities and long lifetimes of low-frequency modes.[30, 34, 39, 139, 141, 142, 143, 160] These low-frequency modes closely follow the scalings predicted by the perturbative VC-ALD models, which are valid at low-frequencies.

LJ argon is a material whose thermal transport has significant contribution from high-frequency modes, even for the bulk [see Fig. 3.5 (c)]. This high-frequency range is where we predict that the perturbative Tamura theory will have non-negligible contributions from higher-order interactions (see Section 3.3.3.2). While the higher-order interactions in the Tamura theory are also predicted to be non-negligible for SW silicon, this does not affect the thermal conductivity predictions significantly because high-frequency modes are not important to thermal transport. The negligible contributions of high-frequency modes is demonstrated by experimental measurements of the thermal conductivity of SiGe alloys, which exceed the high-scatter limit by more than an order of magnitude at room temperature for all compositions. [2, 142, 143, 160] Experimentally-accurate theoretical predictions[39] also demonstrate that high-frequency modes are unimportant to thermal transport, although they do serve as important scattering channels. [28]

The VC-ALD method provides a computationally inexpensive framework, which is essential when using *ab initio* methods for predicting thermal conductivity. [28, 29, 30, 31, 32, 36, 37, 38, 39] Based on our results, we believe that the Tamura theory breaks down for mode diffusivities predicted to be below the high-scatter limit, D_{HS} [Eq. (3.18)]. This breakdown may be true for the high-frequency modes of any disordered lattice[93] and the high-scatter limit D_{HS} should be considered whenever the perturbative VC-ALD method is used. Although the high-scatter limit of diffusivity is usually interpreted as a minimum mean free path, [1, 2, 72, 93] we find that this concept is not necessary for interpreting the results of this work. In a disordered lattice, the fundamental quantities are the mode lifetime and diffusivity[47, 73, 75, 93, 95, 152, 158] and the

VC predicted group velocity is an approximation.

Chapter 4

Thermal Conductivity Accumulation in Amorphous Materials

We predict the properties of the propagating and non-propagating vibrational modes in amorphous silica (a-SiO₂) and amorphous silicon (a-Si) and from them, the thermal conductivity accumulation functions. The calculations are performed using molecular dynamics simulations, lattice dynamics calculations, and theoretical models. For a-SiO₂, the propagating modes contribute negligibly to thermal conductivity (6%), in agreement with the thermal conductivity accumulation measured by Regner et al.[15] For a-Si, propagating modes with mean free paths up to 1 μm contribute 40% of the total thermal conductivity. The predicted contribution to thermal conductivity from non-propagating modes and the total thermal conductivity for a-Si are in agreement with Regner et al.'s measurements. The accumulation in the measurements, however, takes place over a narrower band of mean free paths (100 nm - 1 μm) than that predicted (10 nm - 1 μm).

4.1 Introduction

The vibrational modes in disordered solids (e.g., alloys, amorphous materials) can be classified as propagons (propagating and de-localized, i.e., phonon-like), diffusons (non-propagating and de-localized), and locons (non-propagating and localized). [47, 73] Diffusons contribute to thermal conductivity by harmonic coupling with other modes due to the disorder. Locons do not contribute significantly to thermal transport in three-dimensional systems. [161]

Experimental measurements, estimates based on experiments, and modeling predictions have demonstrated that propagating modes contribute significantly to the thermal conductivity of amorphous silicon (a-Si) [15, 48, 51, 52, 54, 55, 62] and amorphous silicon nitride, [74] but not to that of amorphous silica (a-SiO₂). [1, 2, 15, 49, 50, 51, 53, 70, 71] Notably, using broadband frequency domain thermoreflectance, Regner et al. measured how the thermal conductivity of a-SiO₂ and a-Si thin films at a temperature of 300 K change with the thermal penetration depth associated with the heating laser, which identifies the depth normal to the surface at which the temperature amplitude is $1/e$ of its surface amplitude.[15] Adopting the convention of Koh and Cahill,[162] they interpret the measured thermal conductivity at a given thermal penetration depth to be representative of the phonons with mean free paths (MFP) less than that value, allowing for the construction of the thermal conductivity accumulation function.[163, 164, 165] For a-SiO₂, the thermal conductivity of a 1000 nm thick film did not vary for thermal penetration depths between 100 and 1000 nm. This result suggests that any propagating modes that contribute to thermal conductivity have MFPs below 100 nm. For a-Si, they find that the thermal conductivities of films with thicknesses of 500 and 2000 nm vary by 40% between thermal penetration depths of 100 and 1000 nm. This result suggests that propagating modes with MFPs in this range contribute significantly to thermal conductivity.

To interpret the results of Regner et al. requires knowledge of the MFPs of the propagating modes and the contribution to thermal conductivity from the non-propagating modes. Experimentally, inelastic neutron scattering can be used to measure phonon lifetimes (and from these,

MFPs), but this technique is suited to single-crystal samples. [166] Traditionally, empirical expressions and simple models have been the only means to estimate MFPs in amorphous materials, [1, 2, 49, 68, 69] while the Allen-Feldman (AF) theory can be used to model the non-propagating modes.[47, 48]

Predicting the vibrational MFPs in an amorphous solid requires the group velocities and lifetimes of the low-frequency propagating modes. [1, 48, 49, 50, 51, 52, 53, 54, 55] It is typically assumed that the group velocity of these modes is equal to the sound speed.[1, 2, 48, 49, 50, 51, 52, 68, 69] To evaluate the expressions and models for the low-frequency mode lifetimes requires knowledge of how the lifetimes scale with frequency. [1, 48, 49, 50, 51, 52, 53, 54, 55, 56, 57] The scaling for a-SiO₂ has only recently been measured, with evidence of ω^{-2} , ω^{-4} , and a second ω^{-2} regime as the mode frequency, ω , increases from 3.14 to 6.28×10^{12} rads/s. [58, 59, 60, 61] For a-Si, the scaling is not well understood, [48, 51, 52, 54, 55, 56, 57, 62] with temperature-dependent[54, 56, 63] and film thickness-varying measurements [46, 51, 54, 55, 56, 64, 65, 66, 67] suggesting both ω^{-2} and ω^{-4} scalings. [48, 52]

The objective of this work is to investigate the propagating and non-propagating contributions to the thermal conductivity of a-SiO₂ and a-Si by predicting the MFPs and thermal conductivity accumulation functions for realistic models and comparing the predictions to experimental measurements. The paper is organized as follows. The theoretical formulation and modeling framework are discussed in Section 4.2. The sample preparation for the a-SiO₂ and a-Si bulk models and the computational details are discussed in Section 4.3. In Sections 4.4.1, 4.4.2, and 4.4.3, harmonic lattice dynamics calculations are performed to predict the vibrational density of states, the plane-wave character of the vibrational modes, and the group velocity of the low-frequency propagating modes (i.e., the sound speed). The vibrational mode lifetimes are predicted using the molecular dynamics-based normal mode decomposition (NMD) method in Section 4.4.4. Using the sound speeds and lifetimes, the vibrational mode diffusivities (i.e., the product of the square of the group velocity and the lifetime) are calculated and compared with predictions from the AF

theory in Section 4.4.5. Using this comparison, a cutoff frequency between propagating and non-propagating modes is specified. The properties of the propagating and non-propagating modes are then used to predict the total thermal conductivity in Section 4.5.1. The thermal conductivity accumulation functions are predicted in Section 4.5.2, where the results are compared with the experimental results.

4.2 Theoretical Formulation of Vibrational Thermal Conductivity

We calculate the total vibrational thermal conductivity, k_{vib} , of an amorphous solid from

$$k_{vib} = k_{pr} + k_{AF}, \quad (4.1)$$

where k_{pr} is the contribution from propagating modes [19, 20, 130] and k_{AF} is the contribution from non-propagating modes predicted by the AF theory.[48] Mode-level properties obtained from molecular dynamics (MD) simulations and lattice dynamics calculations will be used as inputs. Equation (4.1) has been used in previous studies of amorphous materials, [1, 48, 49, 50, 51, 52, 53, 54, 55] leading to predictions that while k_{pr} is a negligible fraction of k_{vib} for a-SiO₂ (< 10%), [1, 49, 50, 53] it is non-negligible for a-Si (20 – 80%). [48, 51, 52, 54, 55, 62]

The propagating contribution is modeled as [48, 52]

$$k_{pr} = \frac{1}{V} \int_0^{\omega_{cut}} DOS(\omega)C(\omega)D_{pr}(\omega)d\omega, \quad (4.2)$$

where V is the system volume, ω_{cut} is the maximum frequency of propagating modes, $DOS(\omega)$ is the vibrational density of states (DOS), $C(\omega)$ is the mode specific heat, and $D_{pr}(\omega)$ is the mode diffusivity. When using mode properties obtained from calculations on finite-sized systems, it is

common to write Eq. (4.2) as a summation over the available modes. [48, 52] We choose the integral form because the required use of finite-sized simulation cells limits the lowest frequency modes that can be accessed. An extrapolation must be made to the zero-frequency limit that is more easily handled with the integral. [48, 50, 51, 52, 53, 54, 55] Equation (4.2) is obtained by using the single-mode relaxation time approximation to solve the Boltzmann transport equation for a phonon gas. [20] In the derivation of Eq. (4.2), the system is assumed to be isotropic (valid for an amorphous material) and have a single polarization, making the mode properties only a function of frequency. The choice of a single polarization (i.e., an averaging of the transverse and longitudinal branches) does not significantly change the results predicted in this work or that of others. [48, 51, 52, 53, 54, 55] We will evaluate Eq. (4.2) under the Debye approximation, which assumes isotropic and linear dispersion such that the DOS is

$$DOS(\omega) = \frac{3V\omega^2}{2\pi^2v_s^3}, \quad (4.3)$$

where v_s is an appropriate sound speed.[130]

The specific heat in the classical, harmonic limit is k_B , where k_B is the Boltzmann constant. [86] Taking this classical limit allows for a direct comparison between the lattice dynamics-based predictions and those from the classical MD simulations. The harmonic approximation has been found to be valid for systems ranging from Lennard-Jones (LJ) argon,[81] to crystalline Stillinger-Weber silicon and carbon nanotubes[155] at temperatures below half the melting temperature. The full quantum expression for the specific heat is [20]

$$C(\omega) = k_B \left[\frac{\hbar\omega/2k_B T}{\sinh(\hbar\omega/2k_B T)} \right]^2, \quad (4.4)$$

where \hbar is the Planck constant.[130] The quantum specific heat will be used for the non-propagating modes to compare the k_{AF} predictions to experimental measurements in Sections 4.5.1 and 4.5.2.

The diffusivity of the propagating modes is

$$D_{pr}(\omega) = \frac{1}{3}v_s^2\tau(\omega), \quad (4.5)$$

where $\tau(\omega)$ is the frequency-dependent mode lifetime.[20] An equivalent physical picture in terms of a scattering length is

$$D_{pr}(\omega) = \frac{1}{3}v_s\Lambda(\omega), \quad (4.6)$$

where $\Lambda(\omega)$ is the MFP, defined as

$$\Lambda(\omega) = v_s\tau(\omega). \quad (4.7)$$

The lifetimes will be modeled using

$$\tau(\omega) = B\omega^{-n}. \quad (4.8)$$

By using a constant sound speed, the lifetime and diffusivity frequency scalings will be the same. For amorphous materials, the scaling exponent n has been found experimentally and numerically to be between two and four. [43, 48, 52, 54, 55, 58, 59, 60, 61, 62, 75, 95, 158, 167, 168, 169, 170, 171, 172, 173, 174, 175, 176, 177, 178, 179, 180, 181] A value of two corresponds to Umklapp scattering,[21] while a value of four corresponds to Rayleigh scattering from point defects.[23] Combined with Eq. (4.3), choosing $n \leq 2$ ensures that the thermal conductivity evaluated from Eq. (4.2) is finite. Choosing $n > 2$ causes the thermal conductivity to diverge, which can be fixed using additional anharmonic [48, 52] or boundary scattering terms. [51, 54, 55]

The AF diffuson contribution to thermal conductivity is [48, 52]

$$k_{AF} = \frac{1}{V} \sum_{i, \omega_i > \omega_{cut}} C(\omega_i) D_{AF}(\omega_i), \quad (4.9)$$

where ω_i is the frequency of the i th diffuson mode, $C(\omega_i)$ is the diffuson specific heat, and $D_{AF}(\omega_i)$ is the diffuson diffusivity. Equation (4.9) is written as a sum because there are enough high-frequency diffusons in the finite-size systems studied here to ensure a converged value.[48, 52] The AF diffusivities are calculated from[47]

$$D_{AF}(\omega_i) = \frac{\pi V^2}{\hbar^2 \omega_i^2} \sum_{j \neq i} |S_{ij}|^2 \delta(\omega_i - \omega_j), \quad (4.10)$$

where δ is the Dirac delta function.* The heat current operator S_{ij} , which measures the thermal coupling between vibrational modes i and j based on their frequencies and spatial overlap of eigenvectors, can be calculated from harmonic lattice dynamics theory. [47, 48, 52] For Eq. (4.10), S_{ij} is directionally averaged because amorphous materials are isotropic.

4.3 Calculation Details

4.3.1 Sample Preparation

The three smallest a-SiO₂ samples are the same as those used in Ref. 82 and contain 288, 576, and 972 atoms at a density of 2350 kg/m³. The atomic interactions are modeled using the modified Beest-Kramer-van Santen (BKS) potential [182, 183] from Ref. 82, except that the 24-6 LJ potential[184] is changed to a 12-6, which has a negligible effect on the predictions. The LJ potentials use a cutoff of 8.5 Å and the Buckingham potentials use a cutoff of 10 Å. The electrostatic interactions are handled using the Wolf direct summation method with a damping

*The summation in Eq. (4.10) is performed over all modes $j \neq i$ including modes with $\omega < \omega_{cut}$.

parameter of 0.223\AA^{-1} and a cutoff of 12\AA .[185] Larger systems of 2880, 4608, and 34562 atoms were created by tiling the smaller samples, melting at a temperature of 10000 K, and quenching instantaneously to a temperature of 300 K at constant volume. The melt-quench procedure and subsequent MD simulations were performed using the MD package LAMMPS and a time step of 0.905 fs.[136] The resulting a-SiO₂ structure is built from a network of rigidly-bonded SiO₄ tetrahedral sub-units that are weakly bonded via shared oxygen atoms, as shown in Fig. 4.1 (a). The 34562 atom sample has a supercell side length of 8.05 nm.

For a-Si, we use samples with 216, 1000, 4096, and 100000 atoms, which is the largest to our knowledge, generated from the modified Wooten-Winer-Weaire (WWW) algorithm from Ref. 186. The resulting a-Si structure is a rigid, predominantly tetrahedrally-bonded network[186] and is shown in Fig. 4.1 (b). A larger sample was created from the 100000 atom sample by tiling it twice in all directions to create an 800000 atom sample with a side length of 24.81 nm. All a-Si structures have a density of 2330 kg/m³, equivalent to the perfect crystal with a lattice constant of 5.43\AA . The Stillinger-Weber (SW) potential is used to model the atomic interactions.[131] The MD simulations are performed using LAMMPS with a time step of 0.5 fs.

Amorphous materials may have many different atomic configurations with nearly equivalent potential energies, leading to potential metastability during MD simulations. [52, 62, 187, 188, 189] This meta-stability can cause errors when predicting vibrational lifetimes using NMD (see Section 4.4.4). To remove metastability, all a-SiO₂ and a-Si samples were annealed at a temperature of 1100 K for 10 ns.[52, 62] The removal of meta-stability is demonstrated by a decrease and plateau of the sample's potential energy during the annealing.

4.3.2 Simulation Details

Before data collection, all MD simulations are first equilibrated in an *NVT* (constant number of atoms, volume, and temperature) ensemble for 10^6 time steps at a temperature of 300 K. Data are then collected from simulations in the *NVE* (constant number of atoms, volume, and

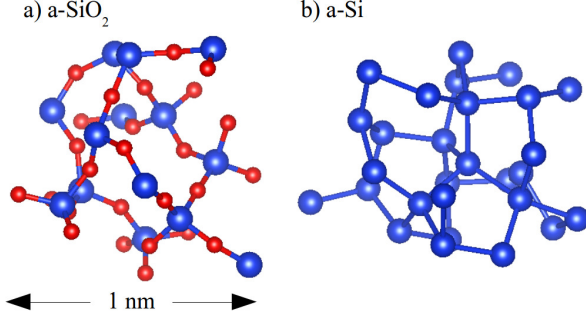


Figure 4.1: (a) Small sample of an a-SiO₂ structure created from a melt-quench technique showing the Si-O tetrahedral bond network. Bond lengths range between 1.6 and 1.8 Å. (b) Small sample of an a-Si structure created by the modified WWW algorithm. Bond lengths range between 2.3 and 2.7 Å. Visualizations using the VESTA package with blue silicon atoms and red oxygen atoms.[146]

total energy) ensemble for 2²¹ time steps, where the atomic trajectories are sampled every 2⁸ time steps. Ten MD simulations with different initial conditions are run and the predictions are ensemble-averaged.

The Green-Kubo (GK) method is used to predict a top-down thermal conductivity k_{GK} [i.e., without using Eq. (4.1)] [86] using the first-avalanche method to specify the converged value of the integral of the heat current autocorrelation function (Section 4.5.1). [190] For system sizes of 4608 (a-SiO₂, supercell side length of 4.026 nm) and 4096 (a-Si, supercell side length of 4.344 nm) atoms, the trajectories from the MD simulations are also used to predict the vibrational mode lifetimes using the NMD method (Section 4.4.4).

For an amorphous supercell, the only allowed wave vector is the Gamma point (i.e., $\kappa = 0$), where κ is the wavevector and there are $3N_a$ polarization branches labeled by ν , where N_a is the number of atoms. Calculation of the vibrational modes at the Gamma point requires the eigenvalue solution of a dynamical matrix of size $(3N_a)^2$ that scales as $[(3N_a)^2]^3$, limiting the system sizes that can be considered to 4608 (a-SiO₂) and 4096 (a-Si) atoms. The eigenvalue solution is also required to predict the vibrational DOS (Section 4.4.1) and structure factors (Section 4.4.2), and to perform the NMD calculations (Section 4.4.4) and the AF calculations (Section 4.4.5).

The frequencies and eigenvectors were computed using harmonic lattice dynamics calculations with GULP.[134] The calculation of the AF thermal diffusivities [Eq. (4.10)] is performed using GULP and a Lorentzian broadening of $14\delta\omega_{avg}$ for a-SiO₂ and $5\delta\omega_{avg}$ for a-Si, where $\delta\omega_{avg}$ is the average mode frequency spacing [$\delta\omega_{avg} = 1.8 \times 10^{10}$ rads/s (a-SiO₂) and 1.0×10^{10} rads/s (a-Si)]. [48, 52] Varying the broadening by 10% around these values does not change k_{AF} within its uncertainty (see Section 4.5.1).

4.4 Vibrational Mode Properties

4.4.1 Density of States

The vibrational DOS is computed from

$$DOS(\omega) = \sum_i \delta(\omega_i - \omega), \quad (4.11)$$

where a unit step function of width $100\delta\omega_{avg}$ is used to broaden $\delta(\omega_i - \omega)$. The results for a-SiO₂ and a-Si are plotted in Fig. 4.2. The DOS for a-Si is similar to that of crystalline silicon, [73, 102] with peaks at mid- and high-frequencies. The DOS for a-SiO₂ is constant over most of the frequency-range, with a gap that separates the high-frequency Si-O interactions.[82] There is a clear ω^{-2} scaling for both a-Si and a-SiO₂ at the lowest frequencies. The onset of this scaling occurs at a higher frequency for a-Si ($\sim 1.5 \times 10^{13}$ rads/s) than a-SiO₂ ($\sim 4.5 \times 10^{12}$ rads/s). This low-frequency scaling is predicted by the Debye model [Eq. (4.3)] and suggests that these modes may be propagating (i.e., phonon-like).

4.4.2 Structure Factor

Calculating the structure factors of the supercell Gamma modes is a method to test for their propagating (i.e., plane-wave) character at a particular wavevector and polarization. This ap-

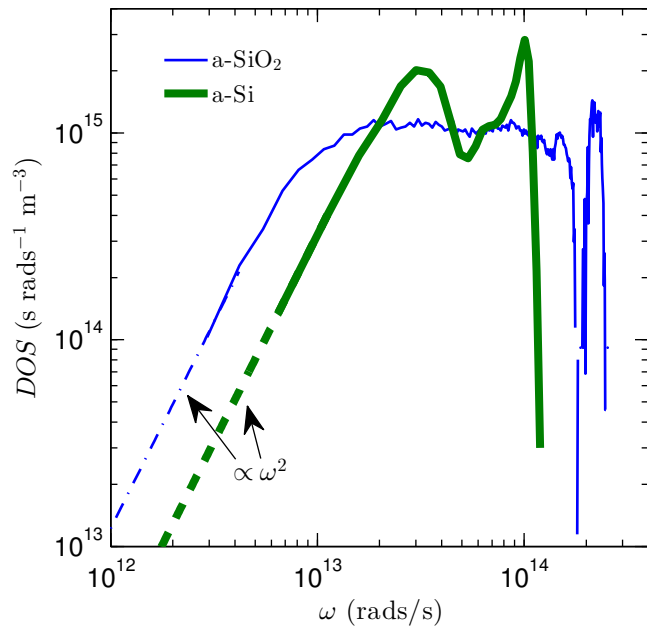


Figure 4.2: Vibrational DOS of a-SiO₂ and a-Si plotted on a log-log scale. Both models show an ω^2 scaling at low frequency. The DOS for a-Si has two peaks similar to the DOS of the crystalline phase.[121] The DOS for a-SiO₂ is flat over most of the spectrum, with a high frequency gap that separates the Si-O interactions.[82]

proach has been previously used to predict effective dispersion curves of disordered and amorphous materials experimentally [45, 53, 59, 61, 154, 168, 171, 172, 191, 192] and numerically. [48, 52, 73, 75, 152, 153, 169, 170, 173, 175, 177, 178, 180, 193, 194, 195, 196, 197] The structure factor at a wavevector κ is defined as[73]

$$S^{L,T}(\omega) = \sum_{\nu} E^{L,T}(\nu) \delta(\omega - \omega(\kappa=\mathbf{0})), \quad (4.12)$$

where the summation is over the Gamma modes, E^T refers to the transverse polarization and is defined as

$$E^L(\nu) = \left| \sum_b \hat{\kappa} \cdot e(\kappa=\mathbf{0} \ b) \exp[i\kappa \cdot \mathbf{r}_0(l=0)] \right|^2 \quad (4.13)$$

and E^L refers to the longitudinal polarization and is defined as

$$E^T(\nu) = \left| \sum_b \hat{\kappa} \times e(\kappa=\mathbf{0} \ b) \exp[i\kappa \cdot \mathbf{r}_0(l=0)] \right|^2. \quad (4.14)$$

In Eqs. (4.13) and (4.14), the b summations are over the atoms in the disordered supercell, $\mathbf{r}_0(l=0)$ refers to the equilibrium atomic position of atom b , l labels the unit cells ($l = 0$ for the supercell), α labels the Cartesian coordinates, and $\hat{\kappa}$ is a unit vector. The vibrational mode shape is contained in the $3N_a$ components of its eigenvector, $e(\kappa=\mathbf{0} \ b)$. [19]

The transverse and longitudinal structure factors are plotted in Figs. 4.3(a) and 4.3(b) for a-SiO₂ and a-Si for wavevectors along the [100] direction of the supercells. Because amorphous structures are isotropic, the structure factors are direction-independent. Mode frequencies, $\omega_0(\kappa)$, and linewidths, $\Gamma(\kappa)$, can be predicted by fitting each structure factor peak to a Lorentzian function of the form

$$S^{L,T}(\omega) = \frac{C_0(\kappa)}{[\omega_0(\kappa) - \omega]^2 + \Gamma^2(\kappa)}, \quad (4.15)$$

where $C_0(\kappa)$ is a constant related to the DOS. [152] A dispersion relation is identified by plotting the $\omega_0(\kappa)$ values in the middle panels of Figs. 4.3(a) and 4.3(b), where the error bars indicate the linewidths. For a-Si, Lorentzian fits to the structure factor peaks have coefficients of determination[198] greater than 0.8 for $|\kappa|/\kappa_{max} \leq 0.75$ and less than 0.7 for $|\kappa|/\kappa_{max} > 0.75$, where $\kappa_{max} = 2\pi/a$ and a is the lattice constant of crystalline silicon (5.43 Å).[131] For a-SiO₂, the coefficients of determination are greater than 0.8 for $|\kappa|/\kappa_{max} \leq 0.2$ and less than 0.7 for larger wavevectors, where the structure factors peaks are less than an order of magnitude larger than the background. To evaluate κ_{max} for a-SiO₂, we use a lattice constant of 4.8 Å, which corresponds to the *a*-direction of quartz.[199]

For a-Si, the extracted dispersion is nearly linear at small wavevectors with a slight decrease in slope at the largest values. [48, 52] For a-SiO₂, the dispersion is concave-down for the smallest wavevectors considered, transitioning to a strong concave-up dispersion at intermediate wavevectors. For the intermediate wavevectors, the longitudinal dispersion for a-SiO₂ is well-described by the so-called “dispersion law for diffusons,” where $\omega \propto \kappa^2$. [152] This large concave-up dispersion has been observed in experimental measurements and numerical models of amorphous materials [53, 75, 173, 175, 191] including a-SiO₂.[53, 75, 173, 191] We note that at frequencies lower than 10^{12} rads/s, experimental measurements of a-SiO₂ recover a linear dispersion. [53, 59, 61, 172, 191] This frequency range is not accessible with the models studied in this work.

The atomic structures of a-SiO₂ and a-Si play an important role in determining the differences in the low-frequency mode properties. The weakly-bonded network of tetrahedra in a-SiO₂ [82, 182, 183, 184] results in a Debye scaling of the DOS that occurs at a lower frequency than in a-Si (Fig. 4.2), which is a network of strongly-bonded tetrahedra. [73, 131, 186, 193] The lower-frequency onset of the Debye-scaling of the DOS for a-SiO₂ leads to the strong non-linear dispersion seen in Fig. 4.3(a). The behavior of the DOS and structure factors demonstrate a clear difference in the properties of the low-frequency modes for our models of a-SiO₂ and a-Si, which

further is investigated in the following sections.

4.4.3 Sound Speed

For a disordered solid, except for the transverse and longitudinal sound speeds, there is not an accepted method to predict the group velocity of individual vibrational modes. While the structure factor gives the frequency spectrum needed to construct a propagating state with pure wavevector κ , the individual mode spectra $E^T(\nu)$ and $E^L(\nu)$ predict the plane-wave character of each mode. [73, 193] It is not generally possible to assign a unique wavevector to individual modes, even at low frequency, [73, 193] which makes predicting their group velocities challenging. While attempts have been made to predict individual mode group velocities, [62, 84, 85, 102, 149, 151] there is no theoretical basis for the proposed methods.

We now use the DOS and structure factors predicted in Sections 4.4.1 and 4.4.2 to predict the group velocities of the low-frequency modes for a-SiO₂ and a-Si (i.e., the sound speeds). By fitting the DOS from Fig. 4.2 to Eq. (4.3), a sound speed is obtained and is reported in Table 4.1. Because the DOS is a mixture of transverse and longitudinal modes, only a single sound speed can be predicted. Both longitudinal and transverse sound speeds can be predicted from the structure factor peaks by forward differencing the dispersion relation as

$$v_s = \frac{\omega_0(\kappa_{min})}{\kappa_{min}}, \quad (4.16)$$

where κ_{min} is $0.1\kappa_{max}$ for a-SiO₂ and $0.125\kappa_{max}$ for a-Si. The results are provided in Table 4.1.

The transverse and longitudinal sound speeds can also be predicted from the material's bulk (G) and shear (K) moduli from[134]

$$v_{s,T} = \left(\frac{G}{\rho} \right)^{1/2} \quad (4.17)$$

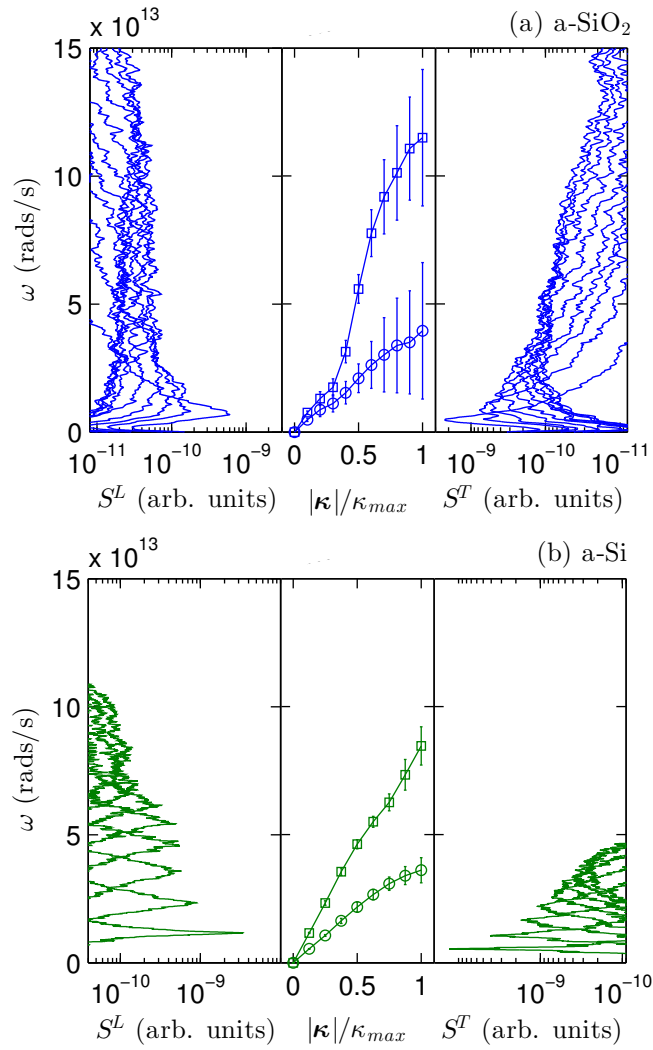


Figure 4.3: Longitudinal (left panel) and transverse (right panel) structure factors [Eq. (4.12)] for (a) a-SiO₂ and (b) a-Si. The wavevectors are normalized by $\kappa_{max} = 2\pi/a$, where a is 4.8 (a-SiO₂) and 5.43 (a-Si) Å, based on the lattice constants of the crystalline phases. [131, 199]

and

$$v_{s,L} = \left(\frac{4G + 3K}{3\rho} \right)^{1/2}. \quad (4.18)$$

Using the bulk and shear moduli defined in terms of the elastic constants according to the Voight convention,[134] the corresponding sound speeds are reported in Table 4.1.

The longitudinal and transverse sound speeds for a-SiO₂ predicted using the moduli are 10-20% lower than predictions made by Horbach et al. using a linear fit to the peaks of the current correlation function for a model with 8016 atoms using the BKS potential [3568 m/s (transverse) and 5937 m/s (longitudinal)]. [173] The smaller values predicted by the structure factors and DOS result from the concave-down dispersion seen at low wavevector (i.e., we are not able to reach the linear portion of the dispersion curve).[173] Experimental measurements of the sound speeds of a-SiO₂ using Brillouin light and inelastic x-ray scattering range between 3800 to 4000 m/s (transverse) and 6000 to 6400 m/s (longitudinal). [168, 172, 191, 200, 201] Differences between our predictions and experimental measurements may be related to limitations of the BKS potential.

The effect of the concave-down dispersion is less pronounced for a-Si than for a-SiO₂, where the sound speeds predicted by all three methods are within five percent of each other. Our sound speed predictions for a-Si using all three methods are within 10% of predictions made using the elastic moduli [202, 203] and structure factor[175] from models created by the original WWW algorithm. [204] The 4096 atom model created by the modified WWW algorithm [186] predicted a longitudinal sounds speed of 7670 m/s from the structure factor, [177] within 5% of our prediction. In an attempt to explain the anomalously high longitudinal sound speed (8300 m/s) and thermal conductivity measurements in Ref. 54, three 1000 atom a-Si models relaxed using a tight-binding electron structure method predicted an average of 4740 m/s (transverse) and 7830 m/s (longitudinal).[54] By annealing our structures to remove metastability, the sound speeds predicted by the elastic moduli are increased, but not by the amount reported in Ref. 54. Experimental transverse sound speeds measurements using Rayleigh wave scattering are 3420

Table 4.1: Longitudinal and transverse sound speeds in m/s estimated from the elastic moduli [Eqs. (4.17) and (4.18)], structure factors [Eq. (4.16)], and DOS [Eq. (4.3)]. The pre-annealed group velocities predicted by the elastic constants are labeled as Moduli*.

Method	Moduli*	Moduli	S^T, S^L	DOS
a-SiO₂				
Transverse	2,541	3,161	2,732	2,528
Longitudinal	4,761	5,100	4,779	
a-Si				
Transverse	3,670	3,886	3,699	3,615
Longitudinal	7,840	8,271	8,047	

and 4290 m/s for sputtered and ion-bombarded a-Si thin films,[205] which is within 15% of the predictions from our models. It is clear that the experimentally-measured sound speeds for a-Si show a wide range.

The sound speed $v_{s,DOS}$ will be used for both a-SiO₂ and a-Si for the rest of this work, allowing for the use of a single polarization for the propagating contribution [Eq. (4.2)]. By comparing the sound speeds in Table 4.1, it is clear that the low-frequency DOS of our models for a-Si and a-SiO₂ are dominated by transverse modes, which is expected due to their degeneracy and lower frequencies compared to the longitudinal modes. The transverse sound speed predicted for our model of a-SiO₂ is 85% of that predicted by the other methods (Table 4.1) and that measured by experiment. [168, 172, 191, 200, 201] While using a smaller transverse sound speed leads to an underprediction of the mode diffusivities [Eq. (4.5)], it leads to an overprediction of the DOS [Eq. (4.3)]. Holding all other input parameters in Eq. (4.1) constant, a smaller sound speed leads to a larger k_{pr} because the DOS scales as $1/v_s^3$. We can thus regard our k_{pr} prediction as an upper bound.

4.4.4 Lifetimes

We now predict the lifetimes of all vibrational modes in our models of a-SiO₂ and a-Si using the MD simulation-based NMD method, [12, 62, 81, 99, 101, 151, 155] which explicitly includes the disorder in the supercell. [62, 83, 84, 85, 196] In NMD, the atomic trajectories from an MD simulation are first mapped onto the vibrational mode coordinate time derivatives, [19]

$$\dot{q}(\kappa=0; t) = \sum_{\alpha, b, l}^{3, n, N} \sqrt{\frac{m_b}{N}} \dot{u}_\alpha(b; t) e^*(\kappa=0 \alpha) \exp[i(\mathbf{0} \cdot \mathbf{r}_0(b)]. \quad (4.19)$$

Here, m_b is the mass of the b_{th} atom in the supercell, \dot{u}_α is the α -component of the atomic velocity, and t is time. Because the supercells of a-SiO₂ and a-Si are disordered, the NMD method can only be performed at the Gamma point ($\kappa = 0$). The spectral energy of each vibrational mode, $\Phi(\nu, \omega)$, is calculated from

$$\Phi(\nu, \omega) = \lim_{\tau_0 \rightarrow \infty} \frac{1}{2\tau_0} \left| \frac{1}{\sqrt{2\pi}} \int_0^{\tau_0} \dot{q}(\kappa=0; t) \exp(-i\omega t) dt \right|^2. \quad (4.20)$$

We choose the frequency-domain representation of the normal mode energy because we find it to be less sensitive to metastability of the amorphous structure than the time-domain representation.

The vibrational mode frequency and lifetime are predicted by fitting each mode's spectral energy to a Lorentzian function,

$$\Phi(\nu, \omega) = \frac{C_0(\nu)}{[\omega_0(\nu) - \omega]^2 + \Gamma^2(\nu)}, \quad (4.21)$$

where the constant $C_0(\nu)$ is related to the average energy of each mode. This expression is valid when the linewidth $\Gamma(\nu) \ll \omega_0(\nu)$.[155] The mode lifetime is[12, 99]

$$\tau(\nu) = \frac{1}{2\Gamma(\nu)}. \quad (4.22)$$

The NMD-predicted lifetimes are plotted in Figs. 4.4(a) and 4.4(b) for a-SiO₂ and a-Si. Also plotted are the timescales extracted from the structure factor linewidths, $1/[2\Gamma(\kappa)]$ (Section 4.4.2). For a-SiO₂, the NMD lifetimes are larger than the Ioffe-Regel (IR) limit $\tau = 2\pi/\omega$, [75] and are bounded by this limit at low frequencies. There is no clear evidence for an ω^{-2} scaling, which would correspond to propagating modes. At mid-frequencies, the NMD lifetimes are approximately constant and there is a peak near 2×10^{14} rads/s, which corresponds to the peak in the DOS (see Fig. 4.2). The lifetimes predicted from the structure factor fall below the NMD-predicted lifetimes and the IR limit. These low values result because the structure factors for a-SiO₂ are evaluated for wavevectors where the resulting wavepackets are formed by non-propagating modes. [48, 52, 73]

For a-Si, the NMD lifetimes show a clear ω^{-2} scaling at low frequency. The lifetimes plateau at higher frequencies, over a wider range of frequencies than for a-SiO₂, with two peaks corresponding to the peaks in the DOS (see Fig. 4.2). A similar plateau of lifetimes at high frequencies has been reported for disordered lattices [83, 93, 196] and another study of a-Si.[62] The transition from the low-frequency scaling to the plateau region occurs near 10^{13} rads/s, which corresponds to where the DOS first peaks in Fig. 4.2. Similar behavior has been observed for models of disordered lattices. [196] The lifetimes predicted by the structure factors are in good agreement with those predicted by NMD at low frequencies. Similar agreement has been reported in other models of amorphous materials. [52, 96, 97, 206] The agreement between the NMD-predicted lifetimes and the structure factor timescales for a-Si at low frequencies indicates that these modes are plane-wave-like and that the wavepackets formed by these modes are propagating. [48, 52, 73]

The NMD-predicted lifetimes for a-Si range from 0.5 to 10 ps and are similar in magnitude to those predicted for previous WWW-generated models of a-Si. [96, 97, 98, 207] We note that one previous study of a-Si modeled using the Tersoff potential predicted vibrational lifetimes on the order of 100 ps,[62] an order of magnitude larger than the values reported here and in previous

studies. [96, 97, 98, 207] It is unclear what the source of this discrepancy is, although in Ref. 62 the NMD analysis was performed in the time domain, where the effects of metastability can be more strongly pronounced. Using the Tersoff potential on the WWW a-Si models in this work, we predict similar lifetimes to those from the SW potential.

4.4.5 Diffusivities

Using the sound speeds predicted from the DOS (Table 4.1), the NMD-predicted lifetimes for a-SiO₂ and a-Si are used to predict the mode diffusivities with Eq. (4.5). The results are plotted in Figs. 4.5(a) and 4.5(b). We note that the sound speed is most appropriate for the lowest-frequency modes, where the DOS scales as ω^2 (Fig. 4.2). The AF theory is also used to predict the mode diffusivities and the results are plotted in Figs. 4.5(a) and 4.5(b).

For a-SiO₂, the mode diffusivities predicted by NMD and AF agree well over the majority of the frequency range. The AF diffusivities at the highest frequencies show a sharp decrease, which is an indication that these modes are localized.[48] The low- and mid-frequency diffusivities are above the high-scatter limit,

$$D_{HS} = \frac{1}{3}v_s a, \quad (4.23)$$

which assumes that all vibrational modes travel with the sound speed and scatter over a distance of the lattice constant. [2] In evaluating Eq. (4.23), we use the lattice constant of the crystalline phases (see Section 4.4.2). The low-frequency NMD diffusivities do not show a definitive scaling. Based on the results in Ref. 53, we choose a propagating/non-propagating cutoff frequency of 4.55×10^{12} rads/s, which is at the onset of the Debye scaling of the DOS (Fig. 4.2). The constant B in Eq. (4.8) for $n = 2$ is then fit to the AF-predicted diffusivities for frequencies below the cutoff by dividing the diffusivities by $v_{s,DOS}$. The fit value is $B = 5.65 \times 10^{13}$ rads²s⁻¹.

For a-Si, the mode diffusivities predicted by NMD at low frequencies show a clear ω^{-2} scaling. The NMD-predicted diffusivities are larger and show less scatter than those predicted by

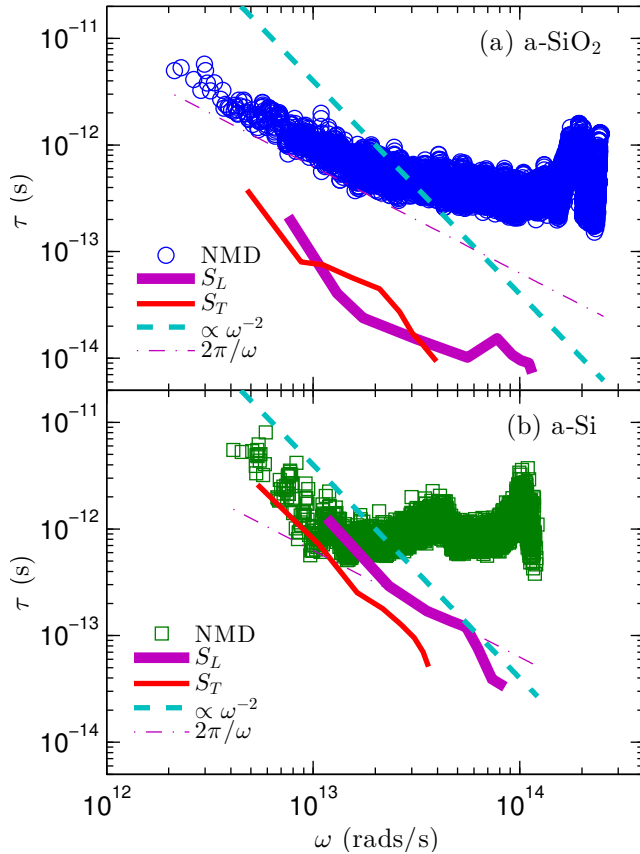


Figure 4.4: Vibrational mode lifetimes predicted by NMD [Eq. (4.22)] and the structure factors [Eq. (4.15)] for (a) a-SiO₂ and (b) a-Si. The NMD-predicted lifetimes are larger than the IR limit. The lifetimes predicted from the structure factors fall below the IR limit at high-frequency for a-Si and for all frequencies for a-SiO₂. For a-Si, a clear ω^{-2} scaling is observed at low frequencies, while the lifetimes plateau at higher frequencies, over a wider range of frequencies than for a-SiO₂, with two peaks corresponding to the peaks in the DOS (Fig. 4.2). The transition from the low-frequency scaling to the plateau region for a-Si occurs near 10^{13} rads/s, which corresponds to where the DOS first peaks in Fig. 4.2.

the AF theory, which is due to the finite-size system and the broadening that is required to evaluate Eq. (4.10).[48] By using a larger broadening ($100\delta\omega_{avg}$), the scatter in the AF-predicted diffusivities at low frequency can be smoothed, but at the cost of decreasing the diffusivities at intermediate and high frequencies, which affects the predicted diffuson contribution to thermal conductivity (see Section 4.5.1). It is possible that a frequency-dependent broadening may be necessary for a-Si and the AF theory, but determining this dependence is not necessary for interpreting our results. For a-Si, the NMD- and AF-predicted diffusivities diverge near a frequency of 10^{13} rads/s. The NMD-predicted diffusivities are relatively constant above this frequency, indicating that the sound speed is no longer an applicable scaling. The AF diffusivities are larger than the high-scatter limit [Eq. (4.23)], except for the highest frequency modes, which are localized. [48]

For a-Si, we choose ω_{cut} and B so that Eq. (4.5) is equal to the average AF-predicted diffusivity at the cutoff frequency. The resulting values are $\omega_{cut} = 1.16 \times 10^{13}$ rads/s (which is at the onset of the Debye scaling of the DOS, Fig. 4.2) and $B = 2.76 \times 10^{14}$ rads²s⁻¹. This choice allows Eq. (4.5) to pass reasonably well through both the AF- and NMD-predicted diffusivities.

While experiments on a-SiO₂ show that there is a cross-over region for the low-frequency lifetime scaling from ω^{-2} to ω^{-4} ,[58] and back to ω^{-2} , [58, 59, 60, 61] our present model is not large enough to investigate the mode properties in this cross-over region. Because experiments are limited for a-Si thin films, [57] we also consider a ω^{-4} scaling for Eq. (4.8). Because this scaling is not clear from the data in Fig. 4.5(b), we use a cutoff frequency of 1.52×10^{13} rads/s (which is at the onset of the Debye scaling of the DOS, Fig. 4.2) based on Refs. 48 and 51 and choose $B = 2.07 \times 10^{40}$ rads⁴s⁻³ so that Eq. (4.5) is equal to the average AF-predicted diffusivity at the cutoff frequency.

Both a-SiO₂ and a-Si have a region at higher frequencies where the AF-predicted mode diffusivities are relatively constant. This behavior has been reported for model disordered systems such as disordered lattices[93, 152, 196] and jammed systems. [95, 158] While diffusons are

non-propagating modes whose MFPs are not well-defined,[48] a diffuson MFP can be calculated from

$$\Lambda_{AF}(\omega_i) = [3D_{AF}(\omega_i)\tau(\omega_i)]^{1/2}, \quad (4.24)$$

where $\tau(\omega_i)$ is the NMD-predicted lifetime for that mode. The diffuson MFPs are plotted in Fig. 4.6. Using this definition, $\Lambda_{AF}(\omega_i)$ for both a-SiO₂ and a-Si is found to vary between the crystal lattice constant (~ 0.5 nm) and the supercell size (~ 5 nm) for modes with frequency above the cutoff. Similar MFPs have been estimated for diffusons in a-Si in previous studies.[48, 52] For modes with frequency below the cutoff, the NMD-predicted MFPs from Eq. (4.7) range up to 16 nm (a-SiO₂) and 43 nm (a-Si). This result is in contrast to the MFPs estimated in Ref. 62 for a-Si, which ranged up to 500 nm. We believe that the origin of the large MFPs in Ref. 62 is a combination of the predicted lifetimes (see Section 4.4.4) and the method used to estimate the mode group velocities.

A diffuson velocity scale can be calculated from

$$v_{AF}(\omega) = \left[\frac{3D_{AF,i}(\omega)}{\tau(\omega)} \right]^{1/2}, \quad (4.25)$$

which is related to the diffuson MFP [Eq. (4.24)]. The calculated diffuson velocities are shown in the insets of Fig. 4.6. For a-SiO₂, v_{AF} is near $v_{s,DOS}$ over the whole frequency range, which is the assumption made for the high-scatter limit Eq. (4.23). For a-Si At low frequencies, v_{AF} is as high as $v_{s,DOS}$ and decreases to about $(1/3)v_{s,DOS}$ in the mid-frequency range. This variation of $v_{AF}(\omega)$ is similar to the variation of the group velocity which can be estimated from the dispersion relation in Fig. 4.3. Compared to the diffuson velocities in Fig. 4.3, the effective group velocities that have been predicted using dispersion relations near zero wavevector for large supercells of amorphous [62, 84, 85] and disordered lattices[149, 151] are underestimates in the low- and mid-frequency range. For the highest frequencies, the modes are localized (locons)

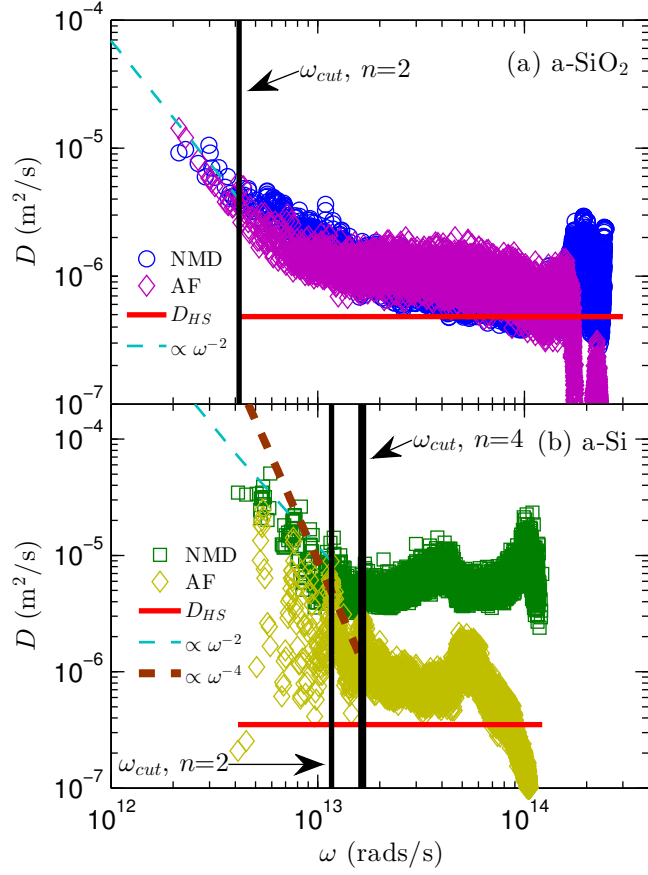


Figure 4.5: Vibrational mode diffusivities predicted from NMD [using Eqs. (4.5) and (4.22) with the DOS sound speed from Table 4.1] and the AF theory [Eq. (4.10)]. Also shown are extrapolations based on an ω^{-2} scaling with Eqs. (4.5) and (4.8) for a-SiO₂ and a-Si, and an additional ω^{-4} scaling for a-Si. For both systems, the diffusivities are larger than the high-scatter limit [Eq. (4.23)] except at high frequencies, where the modes are localized.

and their velocities (and hence, diffusivities) go to zero since they do not contribute to thermal transport.[73]

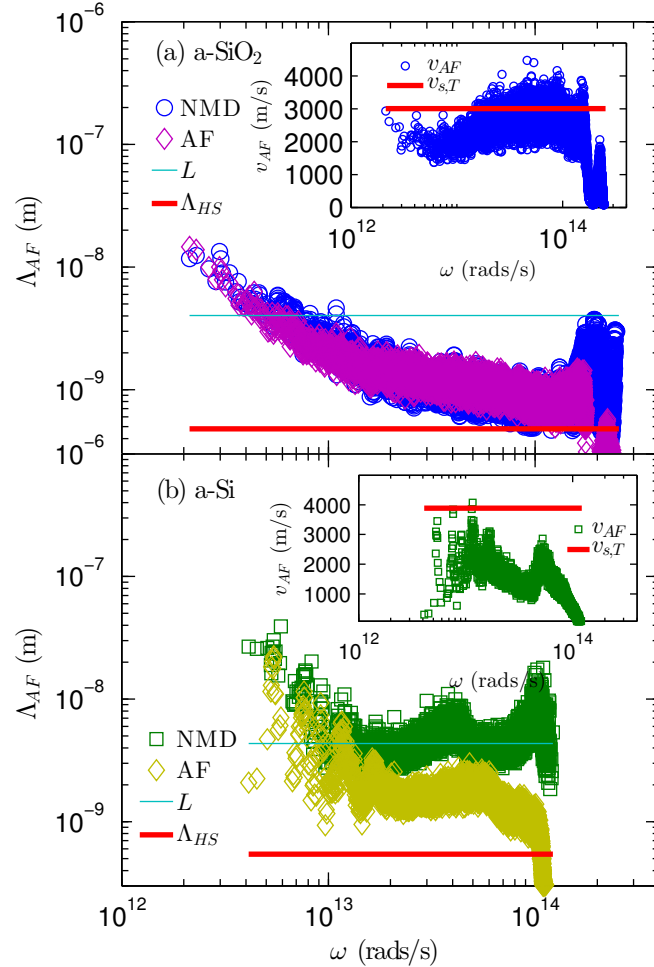


Figure 4.6: (a) Diffuson MFPs predicted from Eqs. (4.7) and (4.24) and velocities (inset) predicted from Eq. (4.25) for a-SiO₂. (b) Diffuson MFPs and velocities predicted for a-Si. The majority of MFPs in the mid- to high-frequency range are between the simulation box size L and the bond distance a . The high-scatter MFP is defined as $\Lambda_{HS} = a$. The MFPs and velocities approach zero only at the highest frequencies, which is an indication that the modes are localized.

4.5 Thermal Conductivity

4.5.1 Bulk

To predict the bulk thermal conductivity for our models of a-SiO₂ and a-Si, we use both Eq. (4.1) and the GK method. The GK method is computationally inexpensive compared to the NMD and AF methods so that larger system sizes can be accessed. The GK-predicted thermal conductivities for a-SiO₂ and a-Si are plotted in Fig. 4.7 versus the inverse of the system size. For a-SiO₂, there is no system-size dependence. The bulk thermal conductivity is estimated to be 2.1 ± 0.2 W/m-K by averaging over all the samples. This prediction is in agreement with the GK predictions in Ref. 82 within the uncertainties, but larger than the MD-based direct-method predictions in Ref. 208. Shenogin et al. predicted the total thermal conductivity of a-SiO₂ using non-equilibrium MD simulations of the same small structures used in this work. They find 2.0 W/m-K for their largest system which was based on a 972 atom model tiled six times in one direction.[157] Our GK-predicted value is larger than experimental measurements, which range between 1.3 and 1.5 W/m-K, [2, 15, 70, 71] which may be due to the classical nature of the MD simulation and/or the suitability of the BKS interatomic potential for modeling thermal transport in a-SiO₂. [82, 208] Quantum statistical effects are considered later in this section.

For a-Si, there is a clear system-size dependence of thermal conductivity. Because the low-frequency DOS has the form of Eq. (4.3) and the diffusivities scale as ω^{-2} , the thermal conductivity will scale as the inverse of the system size. The bulk value can be found by extrapolating to an infinite system size. [29, 36, 155] The extrapolation is performed using the three largest system sizes, [†] leading to a bulk value of 2.0 ± 0.2 W/m-K, where the uncertainty is estimated from the ensemble averaging for each system size. Our extrapolated bulk value is in reasonable agreement with experimental values for a wide range of thin film thicknesses (see Fig. 4.8 in

[†]We do not observe that tiling the a-Si model increases the thermal conductivity above the expected linear scaling as was found in Ref. 62 using the MD-based direct method. This finding is likely due to the small model used to perform the tiling in that study (512 atoms), while we use a large model (100,000 atoms).

Section 4.5.2).

To predict thermal conductivity from Eq. (4.1), we use the parameters B and ω_{cut} specified in Section 4.4.5 assuming an ω^{-2} scaling below ω_{cut} and the AF-predicted diffusivities. For a-SiO₂, the propagating, non-propagating, and total thermal conductivities are 0.10 ± 0.05 , 1.9 ± 0.1 , and 2.0 ± 0.1 W/m-K (see Table 4.2). The uncertainties are estimated by varying ω_{cut} and the AF broadening by 10%. The total value agrees with the GK value within the uncertainties. For the propagating contribution, using an expression similar to Eq. (4.2), Baldi et al.[53] estimated 0.1 W/m-K and Love and Anderson[50] estimated 0.03 W/m-K.

By using the ω^{-2} diffusivity scaling for a-Si, the propagating, non-propagating, and total thermal conductivities are 0.6 ± 0.2 , 1.2 ± 0.2 , and 1.8 ± 0.2 W/m-K. This value for total thermal conductivity is in agreement with the GK-predicted bulk value within the uncertainties. Earlier studies using similar models of a-Si found that k_{pr} is less than half of k_{vib} ,[48, 52] in agreement with our results. A recent study of a-Si modeled using the Tersoff potential found $k_{pr} \approx k_{AF}$.[62] Estimates based on experimental measurements have found k_{pr} to be as low as 20%[51, 52] and as high as 80% of k_{vib} . [54, 55]

If an ω^{-4} lifetime scaling is assumed for a-Si, the thermal conductivity diverges at low frequency. We bound the thermal conductivity by assuming the sample to be a thin film of thickness t_f and modify the lifetimes using the Matthiessen rule,[20]

$$\frac{1}{\tau_{eff}} = \frac{1}{\tau_{bulk}} + \frac{2v_s}{t_f}. \quad (4.26)$$

Using the largest film thickness from the experimental literature ($80 \mu\text{m}$)[54] gives a propagating contribution to thermal conductivity of 3.0 ± 0.4 W/m-K, which is significantly larger than GK-predicted value. Using the ω^{-2} scaling and this film thickness gives a propagating contribution of 0.6 W/m-K (i.e., there is no change from the bulk value). While predictions for k_{pr} for a-Si vary based on the assumed scaling of the low-frequency vibrational lifetimes [48, 51, 52, 54, 55, 62]

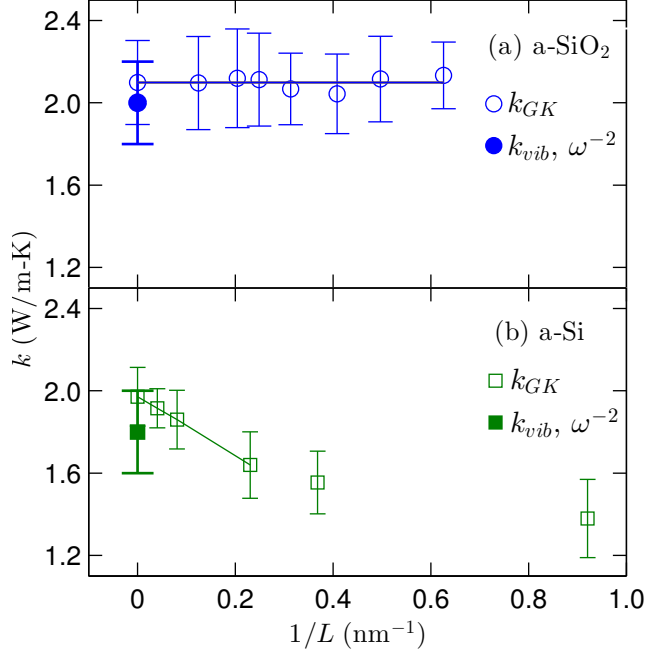


Figure 4.7: Thermal conductivities of a-SiO₂ and a-Si predicted using the GK method and Eq. (4.1). For a-SiO₂, the GK-predicted thermal conductivity is size-independent, indicating that there is not an important contribution from propagating modes. For a-Si, there is a clear size dependence, indicating the importance of propagating modes.

all evidence supports that k_{pr} is a significant fraction of the total thermal conductivity. [15, 48, 51, 52, 54, 55, 62]

In Section 4.2, we approximated the specific heat of the propagating and non-propagating modes by the classical, harmonic-limit value of k_B . At a temperature of 300 K, the quantum heat capacity [Eq. (4.4)] at the largest cutoff frequency for either a-SiO₂ or a-Si is $0.98k_B$, justifying the use of the classical specific heat in the propagating term in Eq. (4.2). For the AF contribution, however, the effect of the quantum specific heat is important. At the highest frequency in each of a-SiO₂ and a-Si, the specific heat is $0.073k_B$ and $0.47k_B$. Using Eq. (4.4) in Eq. (4.9) gives AF thermal conductivities of 1.4 ± 0.1 and 1.0 ± 0.1 W/m-K for a-SiO₂ and a-Si (Table 4.2). This correction brings the estimate of k_{vib} for a-SiO₂ into good agreement with experimental measurements. [2, 15, 70, 71] For a-Si, the modified k_{AF} is 20% lower than the classical-limit value.

Table 4.2: Thermal conductivities for bulk a-SiO₂ and a-Si predicted by the GK method (k_{GK}) and Eqs. (4.1) (k_{vib}), (4.2) (k_{pr}), and (4.9) (k_{AF}). For the non-propagating contribution, classical and quantum specific heats are considered.

Thermal Conductivity (W/m-K)	a-SiO ₂	a-Si
k_{GK}	2.1 ± 0.2	2.0 ± 0.2
k_{vib} (classical)	2.0 ± 0.1	1.8 ± 0.2
k_{pr}	0.10 ± 0.05	0.6 ± 0.2
k_{AF} (classical)	1.9 ± 0.1	1.2 ± 0.1
k_{AF} (quantum)	1.4 ± 0.1	1.0 ± 0.1
k_{vib} (quantum)	1.5 ± 0.1	1.6 ± 0.2

4.5.2 Accumulation Function

In their broadband frequency domain thermoreflectance measurements, Regner et al.,[15] adopting the convention of Koh and Cahill,[162] interpret the measured thermal conductivity at a given thermal penetration depth to be representative of the thermal conductivity accumulation function at a MFP equal to the thermal penetration depth. [163, 165] Their results are plotted in Fig. 4.8(a) for a 1000 nm thick film of a-SiO₂ and in Fig. 4.8(b) for 500 nm and 2000 nm thick films of a-Si. The vertical coordinate of any point on the accumulation function represents the thermal conductivity that comes from phonons with MFPs less than the horizontal coordinate at that point. Also plotted in Figs. 4.8(a) and 4.8(b) are experimental measurements of thin film thermal conductivities. For a-Si, the experimental measurements are broadly grouped by sample preparation technique: (A) chemical vapor deposition [54, 55, 67] and (B) sputtering. [51, 65, 66]

Based on the results in Section 4.4.5, we build thermal conductivity accumulation functions for a-SiO₂ and a-Si from

$$k(\Lambda^*) = k_{AF} + \int_{\Lambda_{cut}}^{\Lambda^*} k(\Lambda) d\Lambda, \quad (4.27)$$

where Λ_{cut} is the MFP at the cut-off frequency, Λ^* is the maximum MFP considered in the thermal conductivity accumulation, $k(\Lambda)$ is the thermal conductivity as a function of MFP,[165] and

the propagating mode MFPs are calculated using lifetimes from Eq. (4.26). The non-propagating contribution k_{AF} is evaluated using the quantum specific heat (see Section 4.5.1). The results are plotted for a-SiO₂ in Fig. 4.8(a) using an infinite film thickness and for a-Si in Fig. 4.8(b) using a film thickness of 80 μm . [‡]

The predicted thermal conductivity accumulation function for a-SiO₂ saturates at a MFP of 10 nm, which is on the order of the finite size of our model. This result is in good quantitative agreement with the thermal penetration depth-independent thermal conductivity measurements using broadband frequency domain thermoreflectance[15] and experimental measurements that show minimal film-thickness dependance. [70, 71]

For a-Si, the low-MFP plateau of thermal conductivity in the measurements of Regner et al. is consistent with our predicted k_{AF} . The propagating contribution to the accumulation is predicted using ω^{-2} and ω^{-4} lifetime scalings, which have both been inferred from thin film experiments. [46, 48, 51, 52, 54, 55, 56] Predictions for both the ω^{-2} and ω^{-4} scalings pass reasonably through the thin film thermal conductivity measurements, particularly for thicknesses in the 50-2000 nm range. The measurements of Regner et al. show sharper accumulations than either the ω^{-2} or ω^{-4} scalings, particularly for the 2000 nm film. For the ω^{-2} scaling, which best matches our model [see Fig. 4.4(b)], the thermal conductivity accumulation saturates at 1 μm , in good agreement with where the measurements of Regner et al. saturate for their 500 nm film. The 2000 nm film accumulation shows no sign of saturation.

[‡]We note that building the accumulation function ignores modes that propagate in a direction that is not perpendicular to the cross-plane film direction that have MFPs larger than the film thickness. Furthermore, Eq. (4.26) reduces the MFP of modes with $\Lambda \sim t_f$ such that plotting MFP and film thickness on the same horizontal axis is an approximation. Since we consider infinite (a-SiO₂) and 80 μm (a-Si) film thickness in evaluating Eq. (4.26), these effects are not important for the range of film thickness and MFPs shown in Figs. 4.8(a) and 4.8(b).

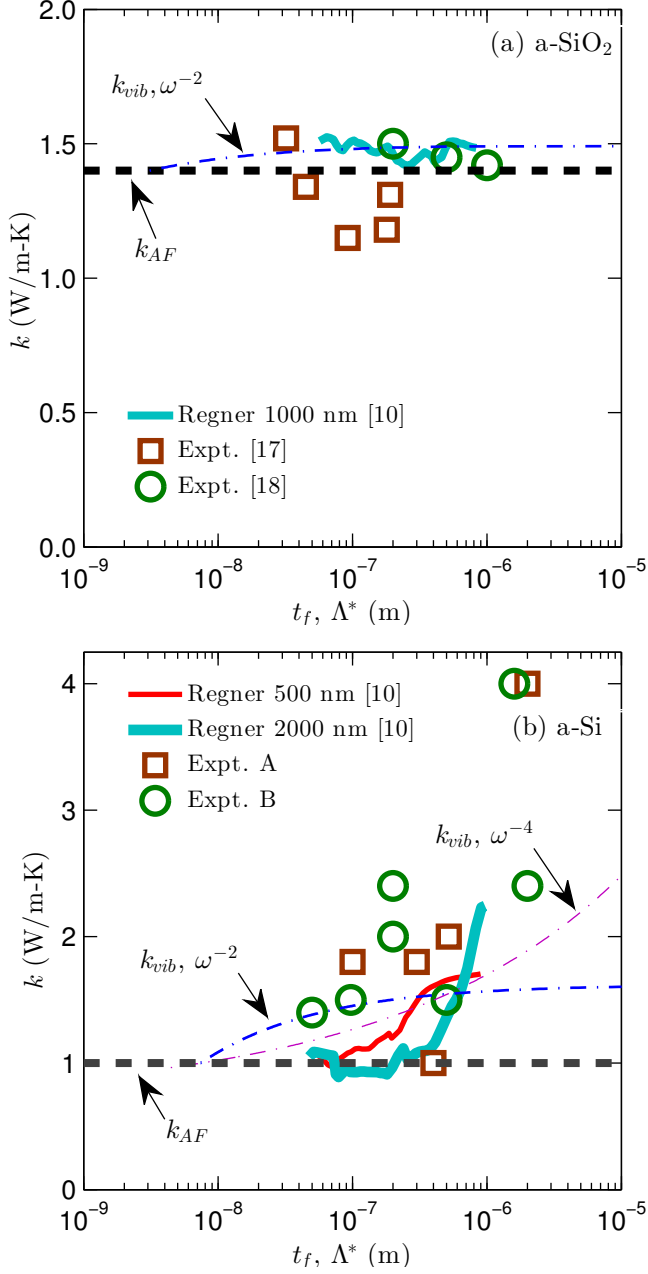


Figure 4.8: (a) Predicted thermal conductivity accumulation function [Eq. (4.27)] for a-SiO₂ compared with experimental broadband frequency domain reflectance measurements by Regner et al.[15] and thin film measurements from Refs. 70 and 71. The predicted thermal conductivity accumulation demonstrates that the propagating contribution is negligible in our model, which is in accord with the experimental measurements. (b) Predicted thermal conductivity accumulation function for a-Si compared with experimental measurements by Regner et al. and thin films fabricated by sputtering (Expt. A) [51, 65, 66] and chemical vapor deposition (Expt. B). [54, 55, 64, 67] The predicted thermal conductivity accumulation demonstrates that the propagating contribution is significant for a-Si. We note that thermal conductivities as high as 6 W/m-K (not plotted) have been measured for a-Si thin films deposited using hot-wire chemical vapor deposition. [55]

4.6 Summary

We investigated the contributions of propagating (k_{pr}) and non-propagating (k_{AF}) modes to the total vibrational thermal conductivity (k_{vib}) of a-SiO₂ and a-Si using the NMD method (Section 4.4.4), AF theory (Section 4.4.5), and the GK method (Section 4.5.1). The atomic structures of a-SiO₂ and a-Si play an important role in determining the mode-level properties needed to predict the propagating and non-propagating contributions. The propagating regime ends at a lower frequency for a-SiO₂, which is evident from the DOS (Fig. 4.2) and the effective dispersion extracted from the structure factors [Fig. 4.3(a)]. This smaller maximum frequency of propagating modes is due, in part, to the weak bonding that exists between the SiO₄ tetrahedra in a-SiO₂, [82, 182, 183, 184] while a-Si is formed by a network of strongly-bonded tetrahedra. [73, 131, 186, 193] The structural differences are also apparent in the low-frequency scalings of the mode lifetimes (Fig. 4.4) which show a clear ω^{-2} dependance (i.e., phonon-like) for a-Si, but not for a-SiO₂. The combined effect of all the mode-level properties results in a significant difference in the propagating and non-propagating contributions to thermal conductivity for a-SiO₂ and a-Si (Table 4.2).

For our model of a-SiO₂, the contribution from propagating modes is negligible ($\sim 6\%$). Our predictions align with experimental measurements of the film thickness-independence of thermal conductivity [70, 71] and thermal penetration depth-independence in the measurements of Regner et al.[15] While the finite size of our model makes it difficult to identify a clear scaling of the low-frequency lifetime scaling, experiments show that both ω^{-2} and ω^{-4} scalings exist in a-SiO₂.[58, 59, 61] In all cases, the propagating contribution to thermal conductivity is negligible.[50, 53, 70, 71]

For our model of a-Si, the thermal conductivity has a significant ($\sim 35\%$) contribution from propagating modes that are best described by a lifetime scaling of ω^{-2} . Our predicted non-propagating thermal conductivity contribution is in good agreement with the plateau at low-MFP for both films studied by Regner et al. For both films, the thermal conductivities accumu-

late much faster than our predictions. The large range of thermal conductivity measurements on a-Si thin films suggest that a comprehensive experimental study using recently developed thermoreflectance techniques[15, 162, 164, 209] on varying film thicknesses and preparation techniques is necessary. It may be particularly helpful to perform the experiments at temperatures less than 10 K, where the propagating contribution dominates for both a-SiO₂ and a-Si and the low-frequency lifetime scaling, which is still under debate, can be better resolved.

[1, 2, 46, 48, 49, 50, 51, 52, 53, 54, 55, 56, 59, 60, 61, 69]

Chapter 5

Conclusion

The vision for the remainder of this thesis is to incorporate as much linked information as necessary, wherever possible. The content contained on the Internet it is growing at an exponential pace. Despite such a rapid rate of progress, the accuracy and quality of the content has managed to remain high on resources such as Wikipedia and Google Scholar. This content is typically available to anyone, anywhere on the planet, making the Internet the ideal platform to present and exchange research. From this point on, hyperlinks to external references and documents will be used with the Latex/hyperlinks package. Printed versions of this document will not contain these hyperlinks, so please refer to the digital version whenever possible.

5.1 Overview and Contributions

5.1.1 Molecular Dynamics-based Methods for Predicting Lifetimes

In Chapter 2, two MD-based methods for predicting phonon properties and thermal conductivity were compared. The Φ method, which is the NMD method in the frequency-domain, was properly derived starting with anharmonic lattice dynamics theory (see Appendix A.1). The meaning of the proposed spectral method, Φ' , was clarified and related to the dynamic structure factor

(see Appendix A.2). While the Φ' method does not accurately predict the mode lifetimes, the advantage of the Φ' versus the Φ method is that it does not require an eigenvalue solution for the mode eigenvectors. The dynamic structure factor, closely related to the Φ' method (see Appendix A.2), can predict frequency-dependent timescales from MD simulations for systems with a larger number of atoms than those studied in this work using the NMD method (see Section 5.2.2).

5.1.2 Thermal Transport in Alloys and the High-scatter Limit

In Chapter 3, thermal transport in two model alloys was investigated. The work provides several original insight into the physics of thermal transport in disordered lattices (i.e., isotopic solids and alloys). The first rigorous test of the virtual crystal (VC) approximation was presented. The VC-ALD technique has been used in a number of recent studies [30, 32, 37, 38, 39], but its limits had not been assessed until this study. The limits of the VC-ALD approach were determined using computationally-inexpensive empirical potentials and self-consistently treating the disorder explicitly and as a perturbation. The results indicate that while VC-ALD is generally an accurate method for materials whose thermal conductivity is dominated by low-frequency vibrational modes, care must be taken when modeling alloys with low thermal conductivities, where significant underprediction of thermal conductivity is likely.

The following calculations that were performed are novel additions to the literature:

- Use of the VC-NMD method to model disordered lattices explicitly. The novel contribution is the use of NMD to predict the lifetimes of a disordered lattice using the normal modes of the virtual crystal (see Section 3.3.3.1 and Appendix A.4).
- To model the disorder explicitly, the AF Theory calculations were performed on a disordered lattice (Section 3.3.4). This theory has only previously been applied to amorphous phases [48, 52, 62, 157]. The AF theory predictions showed that the lower-limit of diffusivity of high-frequency modes in a disordered lattice is the high-scatter limit, in contrast to the VC-NMD and VC-ALD methods, which incorrectly predict that the limiting value

is zero. Identification of this high-scatter limit of mode diffusivity was essential for identifying the breakdown in the VC methods. The high-scatter limit of diffusivity is usually assumed, without theoretical justification, in phenomenological models for disordered and amorphous materials [1, 2, 72]. This study gives self-consistent justification for its use.

- Calculation of the structure factor of disordered lattices to predict effective dispersion (Section 3.3.2). The structure factor was calculated for modes in a model disordered lattice, which has previously been calculated for modes in amorphous materials [48, 52, 73, 75, 152, 153, 169, 170, 173, 175, 177, 178, 180, 193, 194, 195, 196, 197]. The structure factor predictions help to demonstrate that the VC-predicted group velocities are an underprediction of the representative velocity scale for mode diffusivities in the disordered lattice. While previous studies have attempted to predict the group velocity of modes in disordered systems, there is no theoretical justification for the methods used [62, 84, 85, 102, 149, 151].

By using all four methods discussed in Section 1.3, a self-consistent study of the VC approximation identified important connections between the modeling of disordered lattices and amorphous materials. By using three phases of LJ argon (perfect crystal, disordered lattice, and amorphous phase), the applicability of the different methods for predicting the thermal conductivity and mode-properties was demonstrated:

- MD-based GK method: suitable for modeling all three phases, but does not predict the mode properties.
- Phonon-based VC-ALD and VC-NMD: suitable for the perfect crystal and disordered lattices with the high-scatter limit correction.
- The AF theory of diffusons: suitable for the high-frequency modes of the disordered lattice and all modes of the amorphous phase of LJ argon.

5.1.3 Mean Free Paths of Propagating Modes in Amorphous Materials

In Chapter 4, a clear theoretical and modeling framework for amorphous materials was presented, which can form the basis for studying a range of disordered materials. This modeling framework grew as a natural extension of the work and results from Chapter 3. The NMD-predicted lifetimes, along with the material's sound speed, can be used with the AF theory diffusivities to determine the transition from propagating to non-propagating modes (Section 4.4.5). The challenge is that in disordered materials, the group velocities are not well-defined and there is no theoretical basis to predict them [62, 84, 85, 102, 149, 151]. Instead, the mode diffusivities are the fundamental quantities, and the predictions from both the NMD and AF theory methods must be considered simultaneously.

The following calculations that were performed are novel additions to the literature:

- Identified the effects of metastability in amorphous materials on predicting lifetimes using the NMD method (see Section 4.3.1 and Appendix A.5). Metastability is likely to affect the application of the NMD method in other ordered and disordered systems with weak atomic bonding (see Section 5.2.1).
- Identified differences in the structural properties of a-SiO₂ and a-Si that lead to a substantial difference in the propagating contributions to thermal conductivity in each.
- Predicted the effective dispersion from the static structure factor to estimate mode group velocities (Section 4.4.2). While effective dispersions have been predicted from the structure factors for models amorphous materials previously, they had not been used to help predict the thermal conductivity. The effective dispersions justify the use of the sound speed at low frequencies.
- Using the justified sound speeds, it was demonstrated that the NMD-predicted diffusivities are more reliable than those predicted by the AF theory at low frequencies (Section 4.4.5).
- By comparing predictions from the NMD, AF, and GK methods, it was demonstrated that

an ω^{-2} scaling of the low-frequency mode lifetimes best describes the model of bulk amorphous silicon (Section 4.5.1). Comparisons of the predicted thermal conductivity accumulations with experimental measurements demonstrated that further experimentation is necessary to resolve the low-frequency scaling of the mode lifetimes.

5.1.4 Predictive Ability versus Computational Cost

With the results from all of the studies presented in this work, a new ranking of the predictive capabilities for the four methods discussed in Section 1.3 is made in Table 5.1.

The GK method played an important role in verifying the mode properties predicted by all methods. In Chapter 2, the GK method provided a common comparison for the Φ and Φ' methods, which helped to confirm the disagreement between the two methods. In Chapter 3, the GK method provided a comparison for predictions from the VC-NMD and VC-ALD methods, which helped to identify the validity of the high-scatter limit of the diffuson mode diffusivities in disordered lattices. Finally, in Chapter 4, the GK method helped to confirm the scaling of the low-frequency contribution of the finite models of a-Si (Section 4.5.1). The GK method will be a valuable modeling tool for future work on disordered systems.

The VC-ALD method was shown to be limited to low frequency modes and best suited to high-thermal conductivity materials. High thermal conductivity materials are typically dominated by the contribution from low-frequency modes that are well-modeled by VC-ALD. VC-ALD may not be well-suited for low thermal conductivity (full spectrum) materials, where the perturbation theory is not valid. The AF theory models accurately the mid- and high-frequency modes in disordered materials (Section 3.3.4), but it does not properly model the low-frequency modes for disordered lattices. It also does not definitively model the low-frequency modes in amorphous materials (Section 4.4.5).

The VC-ALD method and AF theory can be supplemented by predictions from the NMD method, but additional assumptions are also required. The VC-NMD method is able to accu-

rately predict the lifetimes of all vibrons in disordered lattices (Section 3.3.3.1). However, the effective group velocities are still assumed to be those of the VC, which limits the NMD method's predictive ability (Section 3.4). Propagating modes in a-Si can be identified definitively by NMD-predicted lifetimes (see Section 4.4.4), but an assumption about the effective mode group velocities must be made (Section 4.4.5). Clearly, predicting group velocities for modes in disordered materials is a major challenge that deserves further investigation [62, 84, 85, 102, 149, 151].

With these findings, the predictive methods are re-ranked in order of their capabilities in Table 5.1. The NMD method, while the most computationally demanding of the four predictive methods (Table 1.1), is ranked first in mode- and second in system-level predictive capability. The reasons for these rankings are:

- The NMD method (Φ) is derived correctly from anharmonic lattice dynamics theory and accurately predicts the mode lifetimes and thermal conductivities compared to the Φ' method.
- The VC-NMD method accurately predicts the mode lifetimes for disordered lattices compared to the VC-ALD method. This leads to better agreement with the GK method, which is the most accurate system-level method.
- The NMD method accurately predicts the low-frequency lifetimes for a-Si, while the AF theory predictions have large fluctuations that depend on the broadening factor. The scaling from the NMD lifetimes is used to extrapolate a bulk thermal conductivity which is in good agreement with the system-level GK method.

The ALD and AF theory are considered to be equivalent at predicting mode-level and system-level properties because, for disordered lattices, the VC-ALD method fails to accurately predict the mode lifetimes for high frequencies, while the AF theory is not valid for low frequencies. Either method could be considered superior depending on whether the material being studied is a disordered lattice that is low-frequency dominated or full-spectrum. The AF theory is superior if the material is amorphous, although there have been ALD predictions[207] of the mode lifetimes

Table 5.1: Ranking of the predictive ability from low to high (left to right) of theoretical techniques for mode-level and system-level thermal properties for disordered systems.

System-level	CH Theory	ALD	AF Theory	NMD	GK
Mode-level	CH Theory	GK	AF Theory	ALD	NMD

in a-Si that are in good agreement with NMD predictions[96, 97] in the literature.

5.2 Future Work

5.2.1 Large Unit Cell Materials

Large unit cell (LUC) materials are an important class of crystalline materials with a wide range of thermal transport applications [82, 87, 210, 211, 212]. LUCs have an ordered (crystalline) structure, but the unit cell of the crystal has a large number of distinct atoms. LUCs are effectively disordered over length scales on the order of the atomic spacing and their thermal conductivities can be as low as a glass [213]. One key advantage of LUC materials is that they are still ordered from the standpoint of electrons, which results in good thermoelectric performance [214, 215, 216].

Some LUC materials, such as SiO₂-based zeolites, have been well-studied [82]. Others, such as C₆₀[217] or PCBM, are currently being investigated for their thermal properties [11]. While experimental measurements of PCBM demonstrates that propagating modes contribute negligibly, the mechanisms for its exceptionally-low conductivity are still not understood. Modeling could provide the necessary insights.

From a modeling perspective, LUC materials pose a number of challenges, theoretically and computationally, as compared to small unit cell (SUC) materials:

- Predicting model-level properties using ALD is challenging because the computational time scales as n^4 (Section 1.4).

- LUC are crystalline, but are often organic or organic/inorganic hybrid materials. The structure of LUC materials is often poly- or quasi-crystalline, with less long-range order than SUC materials [212, 218].
- The presence of weak bonding in organic/inorganic materials [212, 219, 220] can lead to metastability (Appendix A.5), which makes it challenging to perform the NMD method.
- MD simulations of LUC materials also face challenges. While many LUC materials have complex bonding environments, DFT calculations are too computationally expensive to perform MD simulations to predict thermal properties [29, 36, 107, 108, 109, 110, 221]. Even empirical interatomic potentials are often computationally-expensive because of the complex bonding terms required [222, 223, 224, 225].

Based on the results in this work, there are several modeling strategies that can be used to study LUC materials:

- Identify signs of propagating modes from experimental measurements, if available [11, 226].
- Based on the results for alloys (Section 3.3.4), the AF diffuson theory may have application for LUC materials, particularly at high frequencies and for those LUC materials which are only quasi-crystalline, such as C₆₀ [218].
- The high-scatter limit for thermal conductivity [Eq. (3.3)] can be used to establish a plausible lower-bound for LUC materials [213]. Similarly, the high-scatter limit for mode diffusivity can establish lower-bounds on the mode-level properties.
- Perform calculations using computationally-inexpensive classical interatomic potentials to assess if DFT calculations are necessary.

5.2.2 Lifetimes from Larger MD Simulations

5.2.2.1 Exact Normal Modes

The NMD method used throughout this work is limited by its computational demands, which require a larger number (~ 100) of parallel processors to perform the analysis in a reasonable amount of time (less than 24 hours, see Appendix B.2.4). While the NMD method is trivially-parallelizable over the normal modes, the eigenvalue solution of the normal modes themselves is more computationally demanding. The eigenvalue solutions can be performed in parallel using the suggestions given in Section 5.2.3.

While parallel eigenvalue solution can increase the system sizes accessible with NMD, the method is ultimately limited by the poor scaling of the run time and memory requirements (Section 1.4). Additional computational cost can be saved by computing only a small subset of the normal modes for a system. A previous study used the Lanczos algorithm[227] to compute a small subset of the normal modes for a 32,000 atom system [206]. The same 32,000 system was subsequently studied using MD simulations and the dynamic structure factor [171], which is discussed in the next section.

5.2.2.2 Dynamic Structure Factor

MD simulations are computationally efficient. Systems sizes of nearly 10^6 atoms have been studied in this work, which were bulk systems with equal simulation side lengths in all three spatial dimensions. The dynamic structure factor, described in Section A.2, can predict vibrational timescales and does not need the eigenvectors of the exact normal modes to perform the mapping of the atomic trajectories. This method, combined with appropriately shaped supercells, could probe the timescales of vibrational modes up to wavelengths between 24 and 100 nm using similar computational resources to those used in this work. This presents an opportunity to compare with experimental measurements of spectral linewidths at frequencies below 1 THz, which have

been recently reported for a-SiO₂ [58, 59, 61, 228] but are lacking for a-Si [57]. The current correlation function, closely related to the dynamic structure factor [173], can even be used to study the spectral character of motions in a fluid [229].

5.2.3 Comprehensive Package for Thermal Transport Calculations

Four different predictive methods were used in this work (Section 1.3). Packages exist for performing some of the calculations necessary for these methods. However, no one package can perform all necessary calculations, particularly both the mode-level and system-level thermal transport properties. LAMMPS, for example, contains both the GK and direct methods for predicting the system-level thermal conductivity. A package to predict the mode-level properties is needed. Ideally, the mode-level properties could be predicted alongside the system-level calculations, as is necessary to perform the NMD and spectral techniques described in Section 2.2.1.

The Python language is an ideal environment for “gluing” together the available codes and extending their functionality in dynamic ways. For example, while the NMD method is trivially-parallelizable over the normal modes, the eigenvalue solution of the normal modes themselves is more computationally demanding. Standard routines for eigenvalue solutions of the dynamical matrix can calculate the exact normal modes for systems up to 8000 atoms in less than 24 hours using current computational resources [134]. These eigenvalue solution routines typically run on single processors. The eigenvalue solutions can be performed using the Portable, Extensible Toolkit for Scientific Computation (PETSc), which has routines for performing eigenvalue solutions in parallel. The PETSc package has Python bindings contained in the `petsc4py` package, which allows for easy interface with the existing lattice dynamics package GULP[134] and MD package LAMMPS [136]. LAMMPS already contains a Python interface, and such an interface could be created for GULP using the `f2py` package.

Appendix A

Computational Details

A.1 Derivation of Phonon Spectral Energy Density, Φ

To derive the correct expression for the phonon SED, Φ , we begin with harmonic lattice dynamics theory [17, 19]. In reciprocal space, the system Hamiltonian, H , is

$$\begin{aligned} H &= \frac{1}{2} \sum_{\kappa, \nu}^{N, 3n} [\dot{q}^*(\kappa; t) \dot{q}(\kappa; t) + \omega_0^2(\kappa) q^*(\kappa; t) q(\kappa; t)] \\ &= \sum_{\kappa, \nu}^{N, 3n} [T(\kappa; t) + V(\kappa; t)], \end{aligned} \tag{A.1}$$

where t is time, $\omega_0(\kappa)$ is the frequency of the phonon mode denoted by wave vector κ and dispersion branch ν , and N and n are the total number of unit cells and the number of atoms in the unit cell. The Hamiltonian is the total system energy and is the sum of the mode- and time-dependent kinetic and potential energies, $T(\kappa; t)$ and $V(\kappa; t)$. The phonon normal mode coordinate, $q(\kappa; t)$ and its time derivative, $\dot{q}(\kappa; t)$, are given by

$$q(\kappa; t) = \sum_{\alpha, b, l}^{3, n, N} \sqrt{\frac{m_b}{N}} u_\alpha(l; t) e^*(\kappa \cdot \alpha) \exp[i\kappa \cdot \mathbf{r}_0(l)] \tag{A.2}$$

and

$$\dot{q}(\boldsymbol{\kappa}; t) = \sum_{\alpha, b, l}^{3, n, N} \sqrt{\frac{m_b}{N}} \dot{u}_\alpha(l; t) e^*(\boldsymbol{\kappa}_\alpha^b) \exp[i\boldsymbol{\kappa} \cdot \mathbf{r}_0(l)], \quad (\text{A.3})$$

where m_b is the mass of the b^{th} atom in the unit cell and $\mathbf{r}_0(l)$ is the equilibrium position vector of the l^{th} unit cell. The α -component of the displacement from equilibrium, $u_\alpha(l; t)$, and velocity, $\dot{u}_\alpha(l; t)$, of the b^{th} atom in the l^{th} unit cell are time-dependent and are related to the phonon mode coordinates through the time-independent eigenvector that has components $e(\boldsymbol{\kappa}_\alpha^b)$.

The potential and kinetic energies of the normal mode are

$$V(\boldsymbol{\kappa}; t) = \frac{1}{2} \omega_0^2(\boldsymbol{\kappa}) q^*(\boldsymbol{\kappa}; t) q(\boldsymbol{\kappa}; t) \quad (\text{A.4})$$

and

$$T(\boldsymbol{\kappa}; t) = \frac{1}{2} \dot{q}^*(\boldsymbol{\kappa}; t) \dot{q}(\boldsymbol{\kappa}; t), \quad (\text{A.5})$$

such that the total energy of the normal mode is

$$E(\boldsymbol{\kappa}; t) = T(\boldsymbol{\kappa}; t) + V(\boldsymbol{\kappa}; t). \quad (\text{A.6})$$

In an anharmonic system, the phonon populations fluctuate about the equilibrium distribution function.[16, 17, 18] The phonon mode coordinate for the mode described by $(\boldsymbol{\kappa}, \nu)$ and its time derivative can be written as

$$q(\boldsymbol{\kappa}; t) = q_{SS}(\boldsymbol{\kappa}; t) + q_T(\boldsymbol{\kappa}; t) \quad (\text{A.7})$$

and

$$\dot{q}(\kappa; t) = \dot{q}_{SS}(\kappa; t) + \dot{q}_T(\kappa; t). \quad (\text{A.8})$$

The steady-state (SS) and transient (T) parts and their time derivatives are given by

$$q_{SS}(\kappa; t) = C_1(\kappa) \exp[i\omega_0(\kappa) t] + C_2(\kappa) \exp[-i\omega_0(\kappa) t], \quad (\text{A.9})$$

$$q_T(\kappa; t) = \exp[-\Gamma(\kappa) |t|] \{ C_3(\kappa) \exp[i\omega_0(\kappa) t] - C_4(\kappa) \exp[-i\omega_0(\kappa) t] \}, \quad (\text{A.10})$$

$$\dot{q}_{SS}(\kappa; t) = i\omega_0 \{ C_1(\kappa) \exp[i\omega_0(\kappa) t] - C_2(\kappa) \exp[-i\omega_0(\kappa) t] \}, \quad (\text{A.11})$$

and

$$\begin{aligned} \dot{q}_T(\kappa; t) = & \exp[-\Gamma(\kappa) |t|] \{ C_3(\kappa) [i\omega_0(\kappa) - \Gamma(\kappa)] \exp[i\omega_0(\kappa) t] \\ & - C_4(\kappa) [i\omega_0(\kappa) + \Gamma(\kappa)] \exp[-i\omega_0(\kappa) t] \}, \end{aligned} \quad (\text{A.12})$$

where the C s are constants and $\omega_0(\kappa)$ and $\Gamma(\kappa)$ are the phonon mode frequency and linewidth. The transient part describes the creation of an excess in the population of a phonon mode for $t < 0$ and its decay back to equilibrium for $t > 0$.

Phonon population fluctuations are commonly modeled using the excitation and decay of a single phonon mode (i.e., the single mode relaxation time approximation). [20] In a real system, there will be multiple phonons in each mode that simultaneously grow or decay with time. Thus,

dealing only with \dot{q} , we let

$$\begin{aligned}\dot{q}(\boldsymbol{\nu}; t) = & \sum_j i \exp[-\Gamma(\boldsymbol{\nu}) |t - t_j|] \times \{ A_j(\boldsymbol{\nu}) [\omega_0(\boldsymbol{\nu}) + i\Gamma(\boldsymbol{\nu})] \exp[i\omega_0(\boldsymbol{\nu})(t - t_j)] \\ & - B_j(\boldsymbol{\nu}) [\omega_0(\boldsymbol{\nu}) - i\Gamma(\boldsymbol{\nu})] \exp[-i\omega_0(\boldsymbol{\nu})(t - t_j)] \},\end{aligned}\quad (\text{A.13})$$

where many phonons in each mode, indexed by j , are simultaneously being created and destroyed. The phonons grow for $t < t_j$, decay for $t > t_j$, and A_j and B_j are constants. We are not concerned with the values of t_j , A_j , and B_j , though they should satisfy the long-time average $\langle \dot{q}^*(\boldsymbol{\nu}; t) \dot{q}(\boldsymbol{\nu}; t) \rangle = \langle \dot{q}_{SS}^*(\boldsymbol{\nu}; t) \dot{q}_{SS}(\boldsymbol{\nu}; t) \rangle$.

The expectation value of the kinetic energy of the normal mode in the time domain is

$$\langle T(\boldsymbol{\nu}) \rangle = \frac{1}{2} \lim_{\tau_0 \rightarrow \infty} \frac{1}{\tau_0} \int_0^{\tau_0} \dot{q}^*(\boldsymbol{\nu}; t) \dot{q}(\boldsymbol{\nu}; t) dt. \quad (\text{A.14})$$

The expectation value of the kinetic energy of the normal mode can be transformed from the time domain to the frequency domain by Parseval's theorem [133], giving

$$T(\boldsymbol{\nu}; \omega) = \lim_{\tau_0 \rightarrow \infty} \frac{1}{2\tau_0} \left| \frac{1}{\sqrt{2\pi}} \int_0^{\tau_0} \dot{q}(\boldsymbol{\nu}; t) \exp(-i\omega t) dt \right|^2. \quad (\text{A.15})$$

By substituting Eq. (A.13) into Eq. (A.15) and performing the time integration we find

$$\begin{aligned}T(\boldsymbol{\nu}; \omega) = & \frac{1}{16\pi\tau_0} \left| \sum_j \exp[-i\omega t_j] \left\{ A_j(\boldsymbol{\nu}) \frac{\omega_0(\boldsymbol{\nu}) + i\Gamma(\boldsymbol{\nu})}{\omega_0(\boldsymbol{\nu}) - \omega + i\Gamma(\boldsymbol{\nu})} \right. \right. \\ & \left. \left. + B_j(\boldsymbol{\nu}) \frac{\omega_0(\boldsymbol{\nu}) - i\Gamma(\boldsymbol{\nu})}{\omega_0(\boldsymbol{\nu}) + \omega - i\Gamma(\boldsymbol{\nu})} \right\} \right|^2.\end{aligned}\quad (\text{A.16})$$

We are primarily interested in values of ω where $\omega \approx \omega_0$ when $\Gamma \ll \omega_0$. When $\omega \approx \omega_0$, the term involving A_j becomes large and the term involving B_j can be neglected (alternatively, we

could ignore the term involving A_j when $\omega \approx -\omega_0$). Hence, we find

$$T(\boldsymbol{\nu}; \omega) = \frac{1}{16\pi\tau_0} \sum_j \sum_{j'} \cos [\omega(t_{j'} - t_j)] A_j(\boldsymbol{\nu}) A_{j'}(\boldsymbol{\nu}) \\ \times \frac{\omega_0^2(\boldsymbol{\nu}) + \Gamma^2(\boldsymbol{\nu})}{\Gamma(\boldsymbol{\nu})} \frac{\Gamma(\boldsymbol{\nu})}{[\omega_0(\boldsymbol{\nu}) - \omega]^2 + \Gamma^2(\boldsymbol{\nu})}. \quad (\text{A.17})$$

We arrive at the expression for the phonon spectral energy density for the wavevector $\boldsymbol{\kappa}$ by summing Eq. (A.17) over the different polarizations ν ,

$$\Phi(\boldsymbol{\kappa}, \omega) = 2 \sum_{\nu}^{3n} T(\boldsymbol{\nu}; \omega) = \sum_{\nu}^{3n} C_0(\boldsymbol{\nu}) \frac{\Gamma(\boldsymbol{\nu}) / \pi}{[\omega_0(\boldsymbol{\nu}) - \omega]^2 + \Gamma^2(\boldsymbol{\nu})}, \quad (\text{A.18})$$

where the factor of two comes from equipartition of kinetic and potential energy (valid for a harmonic classical system, see Section 2.3.3), and

$$C_0(\boldsymbol{\nu}) = \sum_j \sum_{j'} \cos [\omega(t_{j'} - t_j)] A_j(\boldsymbol{\nu}) A_{j'}(\boldsymbol{\nu}) \frac{\omega_0^2(\boldsymbol{\nu}) + \Gamma^2(\boldsymbol{\nu})}{8\tau_0\Gamma(\boldsymbol{\nu})}. \quad (\text{A.19})$$

Thus, the phonon spectral energy density $\Phi(\boldsymbol{\kappa}, \omega)$ is a superposition of $3n$ Lorentzian functions with centers at $\omega_0(\boldsymbol{\nu})$ (one for each polarization) with a linewidth (half-width at half-maximum) of $\Gamma(\boldsymbol{\nu})$. Φ is a spectral energy density since its integral over all wavevectors and frequencies is the total crystal energy, i.e., the Hamiltonian is

$$H = \int_{V_{BZ}} \int_0^{\infty} \Phi(\boldsymbol{\kappa}, \omega) d\omega d\boldsymbol{\kappa}, \quad (\text{A.20})$$

where V_{BZ} is the volume of the first Brillouin zone. Like the frequency broadening, there is also a broadening of the SED in wavevector [111]. For a finite sampling of the first Brillouin zone, the Hamiltonian can be approximated by

$$H \approx 2 \sum_{\boldsymbol{\kappa}, \nu}^{N, 3n} \langle T(\boldsymbol{\nu}; t) \rangle = \sum_{\boldsymbol{\kappa}}^N \int_0^{\infty} \Phi(\omega, \boldsymbol{\kappa}) d\omega. \quad (\text{A.21})$$

A.2 Interpretation of Φ'

As demonstrated in Section 2.4.1, Φ' is not the phonon spectral energy density, Φ , defined by Eq. (2.3). Our findings and those of others [36, 107, 112, 125, 128], however, suggest that Φ' does contain accurate information about the phonon frequencies. To understand this expression, we start with the real-space atomic velocities as represented by the normal mode velocities, $\dot{q}(\kappa'_\nu; t)$ [19],

$$\dot{u}_\alpha(l_b; t) = \sum_{\kappa'_\nu, \nu}^{N, 3n} \frac{1}{\sqrt{m_b N}} \exp[i\kappa' \cdot \mathbf{r}_0(l_b)] e^*(\kappa'_\nu) \dot{q}(\kappa'_\nu; t). \quad (\text{A.22})$$

Fourier transforming both sides of Equation (A.22) in time and space, taking the complex modulus, and summing over the atoms in the unit cell and the Cartesian directions yields

$$\begin{aligned} & \lim_{\tau_0 \rightarrow \infty} \frac{1}{4\pi\tau_0} \sum_\alpha^3 \sum_b^n \frac{m_b}{N} \left| \sum_l^N \int_0^{\tau_0} \dot{u}_\alpha(l_b; t) \exp[\Theta] dt \right|^2 = \\ & \lim_{\tau_0 \rightarrow \infty} \frac{1}{4\pi\tau_0} \sum_\alpha^3 \sum_b^n \left| \frac{m_b^{3/2}}{\sqrt{N}} \sum_l^N \sum_{\nu}^{3n} e^*(\kappa'_\nu) \int_0^{\tau_0} \dot{q}(\kappa'_\nu; t) \exp[\Theta] dt \right|^2, \end{aligned} \quad (\text{A.23})$$

where the sum over κ' on the right-hand-side is reduced to a single wavevector by the orthogonality of the allowed wavevectors over the periodic domain. Equation (2.8) is the finite integration of the left-hand-side of Eq. (A.23).

Under the harmonic approximation, the phonons are non-interacting and have no transient response beyond a harmonic oscillation [see Appendix A.1, Eqs. (A.8) and (A.12)],

$$\dot{q}(\kappa_\nu; t) = \dot{q}_{SS}(\kappa_\nu; t) = i\omega_0(\kappa_\nu) \{ C_1(\kappa_\nu) \exp[i\omega_0(\kappa_\nu) t] - C_2(\kappa_\nu) \exp[-i\omega_0(\kappa_\nu) t] \}. \quad (\text{A.24})$$

Inserting Eq. (A.24) into the right hand side of Eq. (A.23) gives

$$\begin{aligned} \sum_{\alpha}^3 \sum_b^n m_b \left| \sum_l^N \int_{-\infty}^{\infty} \dot{u}_{\alpha}(l; t) \exp[i\boldsymbol{\kappa} \cdot \mathbf{r}_0(l) - i\omega t] dt \right|^2 = \\ \sum_{\alpha}^3 \sum_b^n \left| \frac{m_b^{3/2}}{\sqrt{N}} \sum_l^N \sum_{\nu}^{3n} D(\boldsymbol{\kappa}^b_{\nu}) \exp[i\boldsymbol{\kappa} \cdot \mathbf{r}_0(l)] \delta[\omega_0(\nu) - \omega] \right|^2, \end{aligned} \quad (\text{A.25})$$

where $D(\boldsymbol{\kappa}^b_{\nu}) = i\sqrt{2\pi}\omega_0(\nu)C_1(\boldsymbol{\kappa})e^*(\boldsymbol{\kappa}^b_{\nu})$, δ is the Dirac function, and values of $\omega \leq 0$ are ignored. Thus, at zero temperature Eq. (2.8) is a superposition of Dirac functions at the phonon frequencies $\omega_0(\nu)$.

Equation (2.8) is similar to the definition of the displacement structure factor [152, 153, 173, 177, 194]

$$S_D(\boldsymbol{\kappa}, \omega) = \frac{1}{4\pi\tau_0} \left| \sum_{\alpha}^3 \sum_b^n \frac{m_b}{N} \sum_l^N \int_0^{\tau_0} \dot{u}_{\alpha}(l; t) \exp[\Theta] dt \right|^2, \quad (\text{A.26})$$

which is related to the static structure factor [48, 52, 73, 75, 152, 169, 175, 178, 180, 193, 195, 196, 197] (see Sections 3.3.2 and 4.4.2). [152]. The difference between Eqs. (2.8) and (A.26) is that the summations over α and b occur inside the square modulus for Eq. (A.26). With the summations inside the square modulus, the orthonormality of the mode eigenvectors can be used to show that the static and dynamic structure factors are equivalent under the harmonic approximation [152].

A.3 Unit Cell and Supercell Representations

A.3.1 Unit Cell Choice

Harmonic lattice dynamics is a framework for determining the frequencies and mode shapes of a linear mass-spring system. For a periodic system, the unit cell (i.e., the basis) and lattice vectors

are first specified based on the atomic structure. This specification is not unique. For example, as shown in Table A.1, one can choose a one atom-basis and a face-centered cubic lattice (the primitive unit cell) or a four-atom basis and the simple cubic lattice (the conventional unit cell) to describe the same structure. The unit cell choice may be related to theoretical or computational complexity, but will not affect the bulk properties (e.g., heat capacity or thermal conductivity).

The selection of the unit cell defines the shape of the Brillouin zone and the reciprocal points that will be accessible inside it (i.e., the allowed wave vectors, κ). A supercell can be constructed from either the primitive or conventional unit cell. A supercell constructed using the conventional unit cell with $N_0 = 4$ is shown in Table A.1, where N_0 is the number of unit cells tiled along all three lattice vectors (Section 2.3.1). For a unit cell that is the supercell, the only allowed wavevector is $\kappa = 0$ (i.e., the Gamma point). For a supercell constructed using the conventional unit cell, the allowed wave vectors can be labeled using either the conventional or primitive unit cell description. For a supercell built using the primitive unit cell, however, all wave vectors cannot be labeled using the conventional unit cell description. The number of allowed wavevectors are given in Table A.1.

Here is a matlab code that lists the allowed wavevectors of a supercell constructed from the conventional unit cell according to both primitive and conventional unit cell representations. The code maps the wavevectors onto the first Brillouin zone of the primitive cell. The code works by recognizing that the reciprocal space for an face centered cubic lattice is a body centered cubic lattice. Note that this script can be run using the open-source package octave.

For a supercell with N_a atoms, there are $3N$ normal modes. If the unit cell has one atom, there will be N allowed wave vectors, each with three polarizations (i.e., dispersion branches, which we will denote by ν). For a four-atom unit cell, there will be $N/4$ allowed wave vectors, each with 12 polarizations. In general, the choice of an n -atom unit cell will lead to N/n allowed wave vectors, each with $3n$ polarizations. As such, there are always $3N$ normal modes.

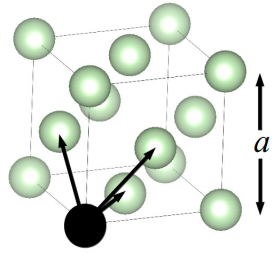
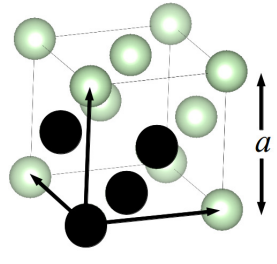
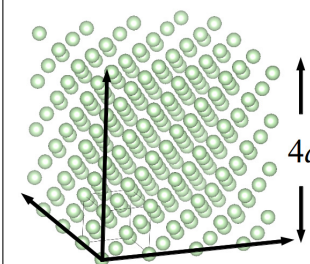
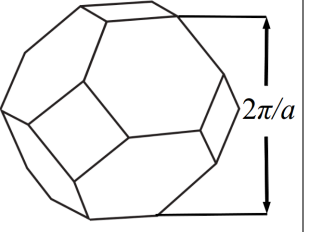
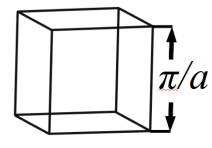
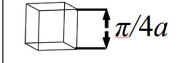
Unit Cell	Primitive	Conventional	Gamma (Supercell)
			
Basis	1 atom	4 atoms	256 atoms
Lattice Vectors	$(a/2, a/2, 0),$ $(a/2, 0, a/2),$ $(0, a/2, a/2)$	$(a, 0, 0),$ $(0, a, 0),$ $(0, 0, a)$	$(4a, 0, 0),$ $(0, 4a, 0),$ $(0, 0, 4a)$
Brillouin Zone	Truncated Octahedron 	Cube 	Cube 
Number of Wave Vectors	256	64	1
Polarizations/Wave Vector	3	12	768

Table A.1: The unit cell for a face-centered cubic crystal with 256 atoms can be chosen in different ways.

A.3.2 Crystal Symmetries

Symmetry operations reduce the information necessary to describe the atomic configuration of crystalline materials. The symmetry operations apply to any vector or tensor property of the crystal. [130] The `spglib` package contains a library of routines for utilizing the symmetry operations of crystals, with good discussion and examples. *Ab initio* codes, such as ABINIT and Quantum Espresso, print the symmetry operations during an electron structure calculation.

For the crystalline LJ argon and SW silicon systems studied in this work, the wavevectors are averaged over according to their symmetries, which reduces the list of wavevectors to the first octant of the cubic Brillouin zone [87]. This reduction is equivalent to applying rotations of

the SO(3) Group, or the group of 90 degree rotations in Euclidean (3-dimensional) space. Any successive combination of 90 degree rotations is also a symmetry operation. This property leads to the identity

$$\boldsymbol{\kappa} = -\boldsymbol{\kappa}, \quad (\text{A.27})$$

which is the application of two 90 degree rotations and is a general property of any crystal. Here is a matlab function that compares two vectors and checks if they are related by any number of orthogonal rotations.

For the face centered cubic crystals studied in this work, further reduction of the wavevectors within the first octant is possible by using all symmetry rotation operations of the face centered cubic lattice. Additional translational symmetry operations may exist. For example, the cubic conventional cell of LJ argon has a four atom basis where every atom is equivalent. Translational symmetry operations ensure that all four atoms in the unit cell are equivalent. Thus, the conventional cell has more total symmetries (rotational plus translational) than the primitive cell, which is due to the redundant information contained within it (Section A.3.3).

A.3.3 Unit Cell Representations using Normal Mode Decomposition

From the same simulation cell and atomic data, one can perform the NMD method on either the primitive, conventional, or Gamma (i.e., supercell) unit cells. The allowed wave vectors are defined by the basis and the supercell used to perform the MD simulations.

The [100] and [111] dispersion curves and density of states obtained from harmonic lattice dynamics calculations are plotted for the primitive and conventional unit cells in Figs. A.1 (a) and A.1 (b). While the dispersion curves in each direction show similarities, they are necessarily different due to the allowed wave vectors and shape of the Brillouin zone (see Table A.1). The density of states, however, are identical, as expected and required. Note that the conventional

unit cell description leads to what appear to be optical modes. These modes are a result of zone folding and can be mapped directly to acoustic modes in the primitive unit cell description.

The lifetimes predicted from the frequency-domain analysis (Φ) for the primitive and conventional unit cell representations of the $N_0 = 10$ system are plotted in Fig. A.2(a). The difference between the lifetimes is less than 5%, which is within the uncertainty of the fitting. A $1/\omega^2$ scaling, predicted from theory for phonon-phonon scattering at low frequencies [21], is plotted and is in good agreement with the trend in the data at low frequencies. Also plotted is the Ioffe-Regel (IR) limit [75], which corresponds to when the phonon lifetime is equal to its period. All the modes in the perfect system have lifetimes well above this limit. It is interesting to note that the phonon lifetimes do not decrease monotonically with increasing frequency, with a maximum observed near $\omega = 18$. Such a maximum is also observed in silicon lifetimes obtained from the SW potential [230] and from DFT calculations [29].

In performing the normal mode decomposition, one is not limited to the primitive or conventional unit cells. As needed for disordered systems (see Sections 3 and 4) one can define the simulation cell as the unit cell, such that all normal modes have $\kappa = 0$ (i.e., they are all at the Gamma-point). In Gamma-point analysis, all normal modes have zero group velocity and it is not possible to predict mean free paths or thermal conductivity. The lifetimes for Gamma-point analysis for the same MD data used to generate the lifetimes in Fig.A.2(a) are plotted in Fig.A.2(b). The trends for the Gamma-point analysis are the same as for the primitive and conventional unit cells. There is more scatter in the Gamma-point data as wave vector symmetry averaging is no longer possible.

For the perfect LJ crystal, there is no clear advantage of performing the analysis in the time or frequency domains or for the primitive or conventional unit cells. Challenges may emerge for high thermal conductivity materials like silicon or carbon nanotubes, where the time-domain decay may not be well described by an exponential and the peaks in frequency space get narrow or are not well-fit by a Lorentzian. The failure of the fitting for a perfect crystal is an indication

that the relaxation time approximation may not be appropriate and that care should be taken when interpreting the results. In general, new materials should be investigated on a case-by-case basis to determine the approach that minimizes the uncertainty.

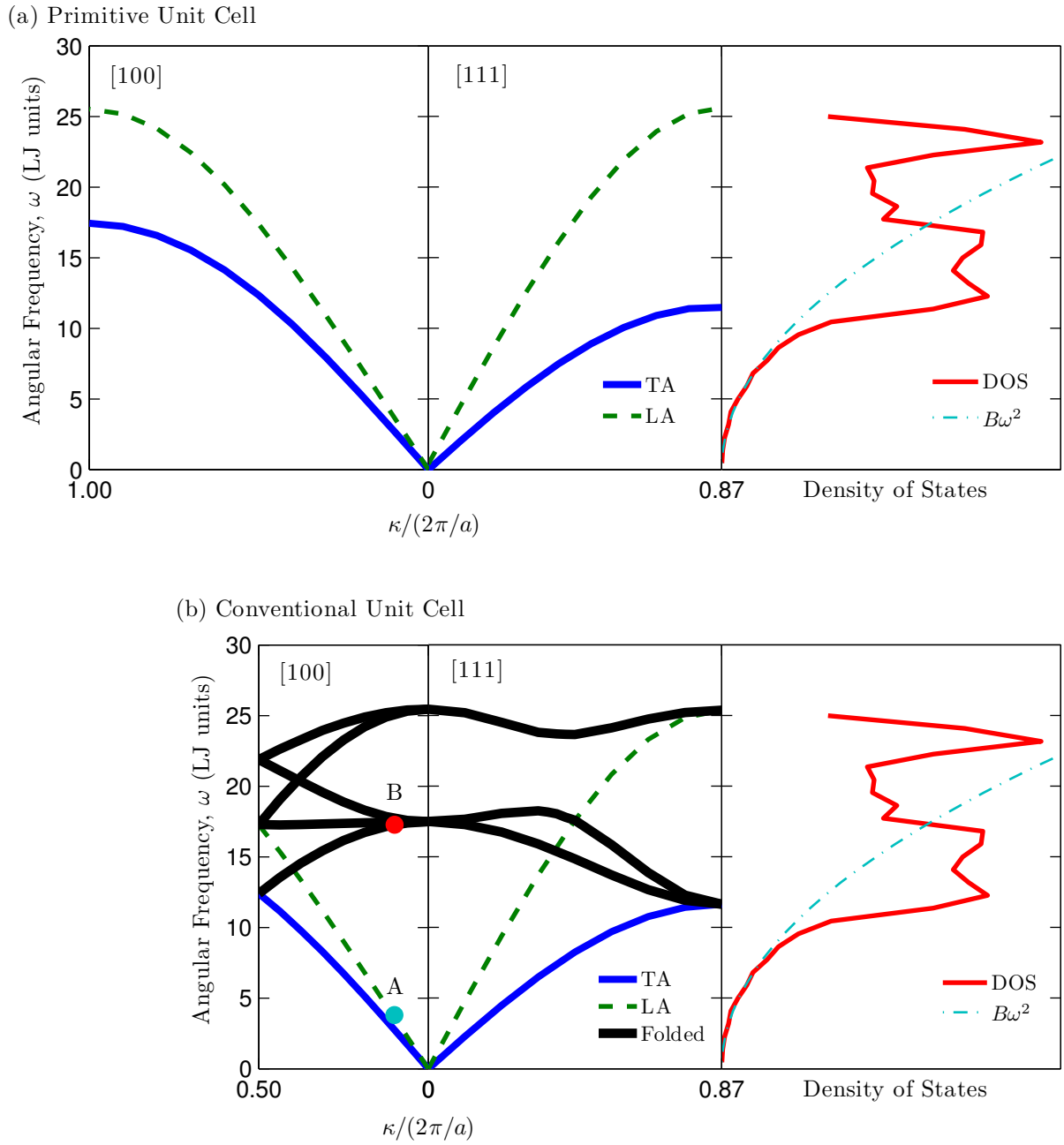


Figure A.1: Dispersion curves and full Brillouin zone density of states for a LJ crystal at a temperature of 10 K. (a) [100] and [111] dispersion curves and density of states based on the primitive (i.e., one atom) unit cell. (b) [100] and [111] dispersion curves and density of states based on the conventional (i.e., four atom) unit cell. The harmonic lattice dynamics calculations are performed using a resolution of sixteen wave vectors along the reciprocal lattice vectors of the conventional unit cell. The red and blue dots in (b) are the modes considered in Fig. A.3.

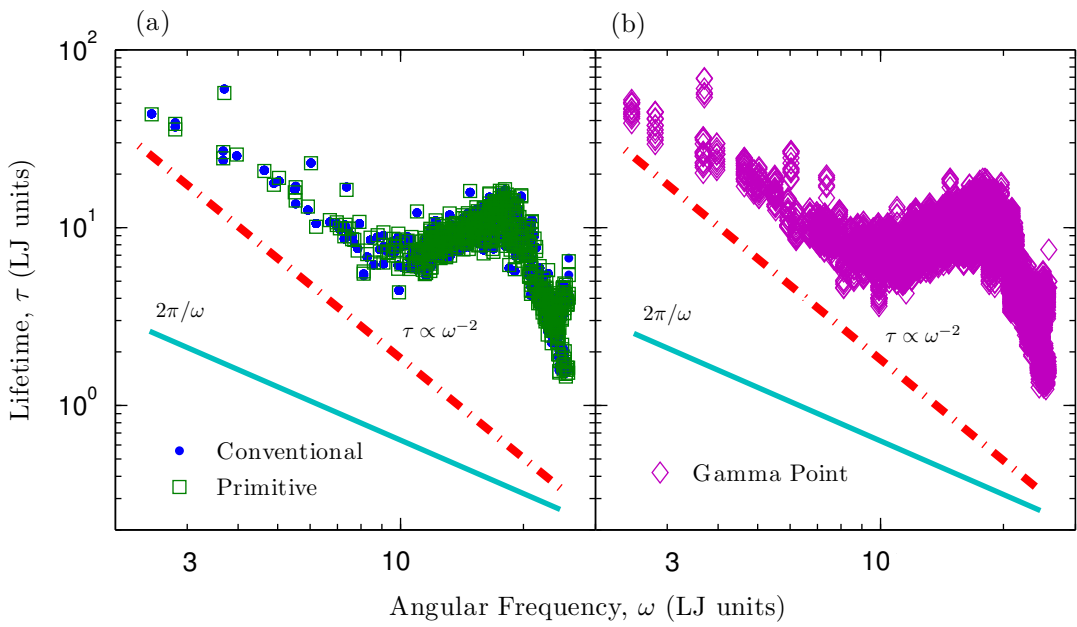


Figure A.2: Lennard-Jones lifetimes from a $N_0 = 10$ system at a temperature of 10 K predicted from the NMD method on (a) the primitive and conventional unit cells, and (b) treating the simulation cell as the unit cell (i.e., Gamma-point analysis). All lifetimes extracted from frequency-domain analysis (Φ).

A.4 Normal Mode Decomposition using Non-Exact Normal Modes

In Chapter 2, it was shown how NMD is applied to a perfect crystal. In reality, any crystal will have some deviation from perfect periodicity, which may be caused by a point defect, a dislocation, a grain boundary, or a free surface. In extreme cases, these deviations from periodicity will lead to the emergence of modified normal modes. For small perturbations, however, it is reasonable to assume that the frequencies and mode shapes of the normal modes will be unchanged and that the effect of the perturbation will be on the lifetimes. Under this assumption, one can still project the atomic positions and velocities onto the normal modes of the unperturbed system.

While one could perform the NMD for an alloy by projecting the atomic positions and velocities onto the modes of the unperturbed system, it is more appropriate to use the virtual crystal approximation (Section 3.3.3.1). Under the virtual crystal approximation, the system is replaced by one where all atoms have the same mass, equal to the average of the atomic masses in the system of interest. This system will have the same mode shapes as the original system, but the frequencies are modified due to the change in the average atomic mass.

Results for the time- and frequency domain approaches to NMD are shown for two modes for crystalline and alloyed LJ argon in Figs. A.3(a)-(d). These two modes are equivalent to those shown in the perfect crystal in Figs. A.1(b), 2.1(a), and 2.1(b). For a concentration, c , of 0.05, both peaks in the frequency domain are well-formed and a lifetime can be extracted by fitting the data to a Lorentzian function. This behavior is typical of all modes at a concentration of 0.05. The downward frequency shift is related to the increased average atomic mass.

For an alloy concentration of 0.5, the lower frequency mode still has a well-formed peak. The higher-frequency mode does not, however, such that a lifetime cannot be extracted by fitting to a Lorentzian function. Such behavior is typical of the higher-frequency modes at high alloy concentrations. This change in behavior is also seen in the time domain, where the decay of

the autocorrelation of the total mode energy is no longer a smooth exponential function. This behavior indicates that the virtual crystal normal mode is not a good description of the true normal mode. Equation (2.7) can be used to approximate a lifetime, as shown in Figs. A.3(c) and A.3(d).

These artifacts observed using the NMD method with the virtual crystal approximation are not surprising given two considerations: (i) the MD simulations contain explicit disorder that influences the atomic trajectories, and (ii) the VC-normal modes are not the exact normal modes of the explicitly-disordered lattice supercells. An effective lifetime can be predicted using Eq. (2.7) because the VC total mode energy autocorrelations still decay to zero in a finite time. This result is to be expected given that the atomic trajectories contain information about the lattice energy, which from general statistical physics principles will have exponential relaxation behavior in an equilibrium ensemble [18, 231, 232].

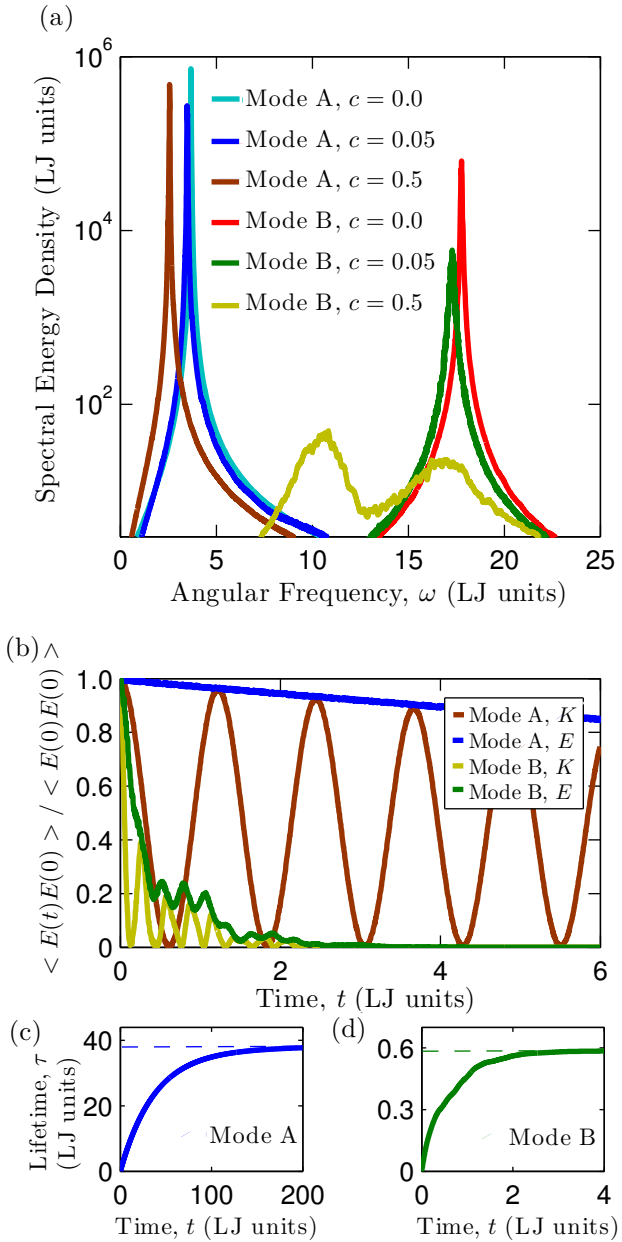


Figure A.3: Virtual crystal (a) frequency-domain and (b) time-domain NMD analysis for two modes in LJ alloys with concentrations of 0.05 and 0.5 at a temperature of 10 K. For modes that are not well-approximated by the virtual crystal modes, the lifetime can be approximated using Eq. (2.7), as shown in (d).

A.5 Effect of Metastability on Normal Mode Decomposition

Amorphous materials may have many different atomic configurations with nearly equivalent potential energies, leading to potential metastability during MD simulations [52, 62, 187, 188, 189]. This meta-stability can cause errors when predicting vibrational lifetimes using NMD, which is demonstrated below.

This case study is performed on an amorphous LJ system with 2048 atoms at a temperature of 5 K. The amorphous solid is generated by liquefying the crystal, instantaneously removing all kinetic energy, and then relaxing the structure (i.e., a melt-quench, Sections 4.3 and 4.3.1). The MD simulation parameters are the same as for the LJ crystal and alloy (Section 4.3). The LJ amorphous phase is metastable at this temperature and intermittently moves between very similar low-energy states. Evidence for the metastability can be found by analyzing the time-histories of the atomic displacements. As such, NMD, which requires the average atomic positions, will be an approximation.

The time- and frequency-domain approaches to NMD are shown for two mode in the amorphous system in Figs. A.4(a) and A.4(b). Because the analysis is performed at the Gamma-point, the peaks are well formed, but they are not Lorentzian. The oscillations in the total energy correlation for the low frequency mode is a consequence of the metastability of the amorphous phase. As such, the lifetimes are extracted by using Eq. (2.7), as shown in the inset to Fig. A.4(b). The lifetimes for the amorphous system are plotted in Fig. A.5. Compared to the crystal, the lifetimes show little frequency dependence and a significant number at low frequencies fall below the IR limit [Eq. (3.12)]. This result seems to be a consequence of the metastability, since this behavior is not observed for the NMD-predicted lifetimes for a-SiO₂ and a-Si (Fig. 4.4, Section 4.4.4), which were both annealed carefully to remove metastability (Section 4.3.1). Annealing the amorphous LJ system at the temperature studied does not remove metastability and leads to re-crystallization if performed for a long enough time (> 5 ns).

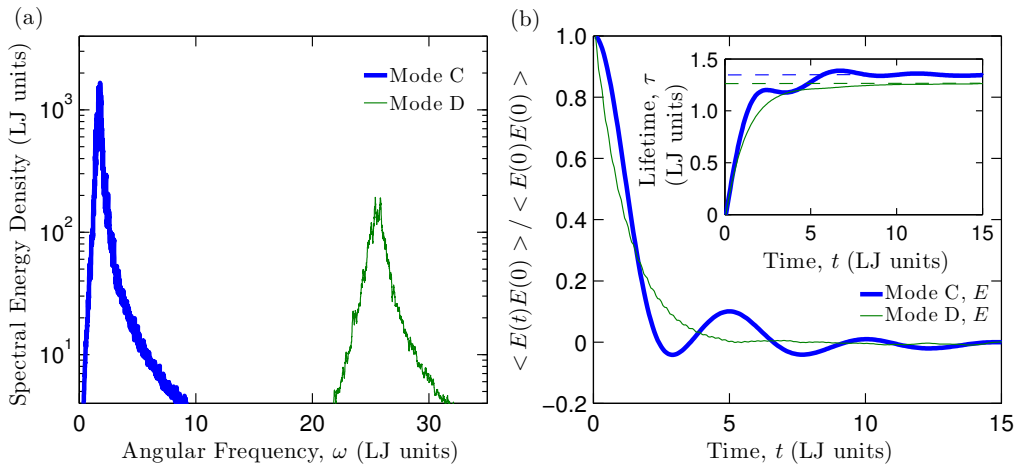


Figure A.4: (a) Time-domain and (b) frequency domain NMD analysis for two modes in an amorphous LJ solid at a temperature of 10 K.

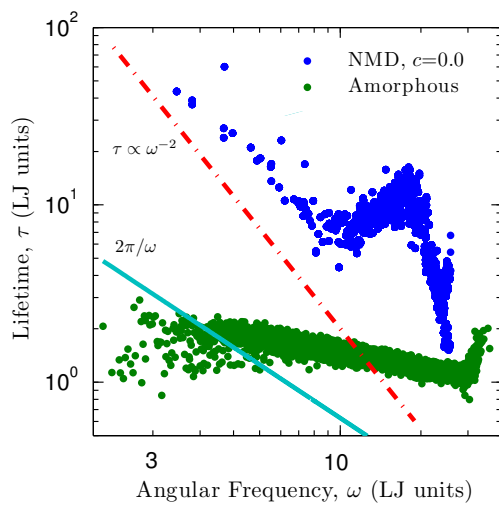


Figure A.5: Lifetimes predicted by normal mode decomposition for an amorphous LJ phase at a temperature of 5 K. The lifetimes for the crystal at a temperature of 10 K are provided for comparison.

A.6 Finite Simulation-Size Scaling for Thermal Conductivity

The thermal conductivities predicted by the NMD (Φ), Φ' , VC-NMD, VC-ALD, and GK methods are system size-dependent [i.e., $k = k(N_0)$] for all lattices and amorphous materials except perfect LJ argon from GK [81] and a-SiO₂ (Section 4.5.1). To predict a bulk thermal conductivity, k_{bulk} , a linear extrapolation procedure is used, whereby

$$\frac{k(N_0)}{k_{bulk}} = 1 - \frac{c_0}{N_0}, \quad (\text{A.28})$$

where c_0 is a constant [12, 29, 36, 85]. This procedure is necessary because the first Brillouin zone is only sampled at a finite number of points for a finite simulation size, with no contribution from the volume at its center. To predict a bulk thermal conductivity, it is important to sample points near the Brillouin zone center, where the modes can have large lifetimes and group velocities [12, 123].

The thermal conductivity is predicted for varying system sizes and the bulk thermal conductivity is obtained by fitting Eq. (A.28) to the data. For the NMD (Φ), Φ' , VC-NMD, and VC-ALD methods, the validity of Eq. (A.28) requires that the low-frequency modes be dominated by phonon-phonon scattering (i.e., $\tau \propto \omega^{-2}$) and follow the Debye approximation with respect to the group velocity and DOS [29, 36].

For the LJ argon alloys, the requirements for Eq. (A.28) are satisfied for modest system sizes (for $N_0 = 6$ to 12). For bulk and alloyed SW silicon, the thermal conductivity is dominated by low-frequency modes, so that large system-sizes are needed to satisfy the extrapolation requirements and only GK and VC-ALD can be used to predict a bulk value from Eq. (A.28). The thermal conductivities of SW silicon and alloys for varying system sizes (N_0) predicted by the VC-ALD, GK, and VC-NMD methods are plotted in Fig. A.6. For the perfect crystal, there is no system size dependence for VC-ALD, and no dependence for GK for $N_0 > 22$. The VC-NMD method can only predict thermal conductivities for small systems ($N_0 = 8$), and the predictions

are in reasonable agreement with the VC-ALD and GK predictions.

For the SW silicon alloys, there is a strong system size dependence of the thermal conductivity up to $N_0 = 38$ for both VC-ALD and GK predictions. This dependence is due to the scaling of the low-frequency lifetimes for the alloys, which are plotted in Fig. A.7 (a). The VC-NMD and VC-ALD predictions are in good agreement up to $N_0 = 8$. For system sizes with $N_0 < 38$, the low-frequency lifetimes scale as $\tau \propto \omega^{-4}$, which leads to a diverging thermal conductivity in the zero-frequency limit. The thermal conductivity as a function of frequency is plotted in Fig. A.7 (b). For the lowest frequencies of $N_0 = 38$, the lifetimes transition to a scaling $\tau \propto \omega^{-\alpha}$ with $\alpha \leq 2$, allowing Eq. (3.21) to be used for $N_0 \geq 38$. A lifetime scaling of $\tau \propto \omega^{-1}$ is predicted at the lowest frequencies, which results from three phonon processes involving transverse acoustic phonons [233, 234]. The alloy thermal conductivities predicted by VC-ALD are 20% larger than those from GK. This overprediction by VC-ALD compared to GK is close to the overprediction (15%) of VC-ALD using DFT calculations of SiGe alloys compared to experiment without including disorder explicitly [39].

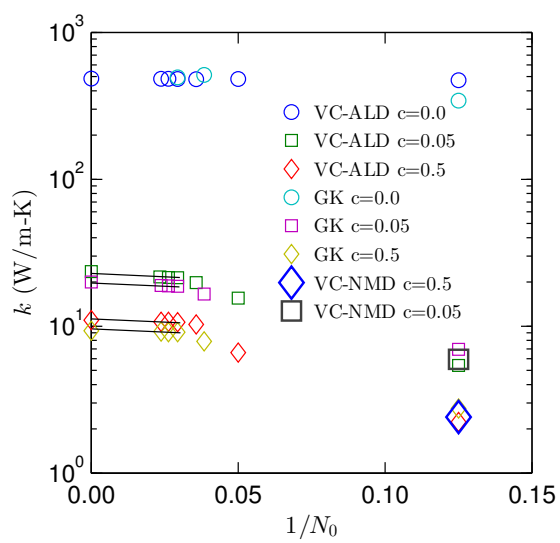


Figure A.6: Stillinger-Weber silicon thermal conductivities for varying system sizes (N_0) predicted by the VC-NMD, VC-ALD, and GK methods. There is a strong system-size dependence up to $N_0 = 38$ for the VC-ALD and GK methods.

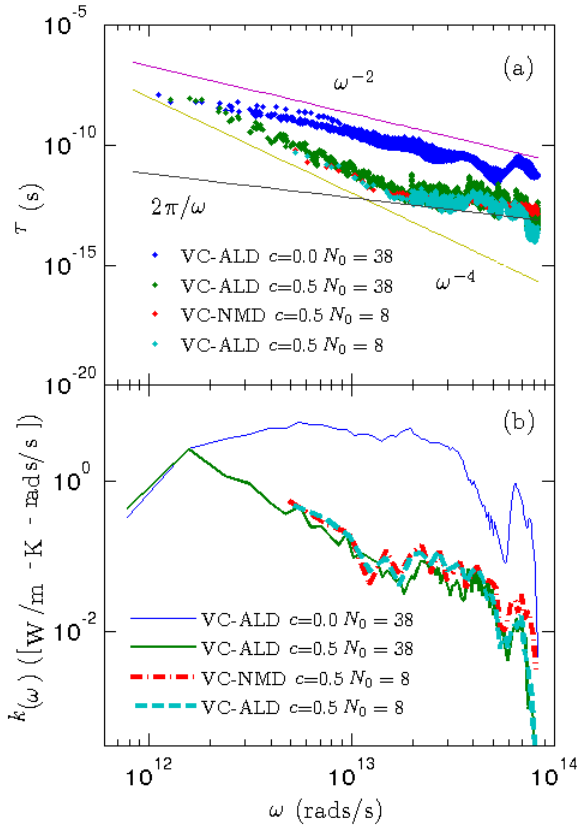


Figure A.7: (a) Lifetimes predicted by the VC-ALD method for Stillinger-Weber silicon and alloys for a system size $N_0 = 38$. The mid-range lifetimes scale as $\tau \propto \omega^{-4}$, which leads to a diverging thermal conductivity. (b) Predicted thermal conductivity as a function of frequency, which demonstrates the saturation at low frequency when the lifetimes transition to a scaling $\tau \propto \omega^{-\alpha}$ with $\alpha \leq 2$.

A.7 Allen-Feldman Theory Calculations

For the AF theory, modes couple by spatial and energetic overlap under the harmonic approximation. The strength of the overlap is determined by how close the mode energies (frequencies) are and how much the eigenvectors spatially overlap [Eq. (4.10)]. The eigenvectors of the two highest frequency modes of the LJ alloy at a concentration of 0.5 (Section 4.3) are shown in Fig. A.8. Only the two dimensional (x and y components) of the eigenvectors are plotted and the mode frequencies are $\omega_{max-1} = 24.0$ and $\omega_{max} = 24.1$ in LJ units. These modes are both locons, which is indicated by the spatial localization of their eigenvector components. While the modes have similar frequencies, the lack of spatial overlap prevents them from coupling thermally according to the AF theory [47, 48].

To calculate the diffusivities using the AF theory [Eq. (4.10)], Allen and Feldman suggest using a broadening that is larger than the average frequency spacing, $\delta\omega_{avg}$ [47, 48]. The frequency spacing as a function of frequency is plotted in Figs. A.9(a) and A.9(b) for the LJ alloy with a concentration of 0.5 and the amorphous phase. For both systems there is a large variation of the frequency spacing, particularly at low and high frequencies, which are up to two orders of magnitude larger than the average frequency spacing $\delta\omega_{avg}$. The role of frequency-dependent broadening deserves further investigation, which could help to explain the difference in the AF- and NMD-predicted diffusivities for a-Si (Fig. 4.5).

For the LJ amorphous phase, a frequency dependent broadening does not seem necessary for accurately predicting the thermal conductivity from the AF theory when compared to the GK prediction (Section 3.4). However, the value of the AF-predicted total thermal conductivity is dependent on the average broadening value used. The predictions for LJ alloys and the amorphous phase are plotted in Fig. A.10. There is a near-linear relation between the predicted thermal conductivity and the average broadening used, given in increments of the average frequency spacing $\beta\delta\omega_{avg}$. MD simulations could be helpful in determining what frequency-dependence of the broadening is required by the AF theory calculations.

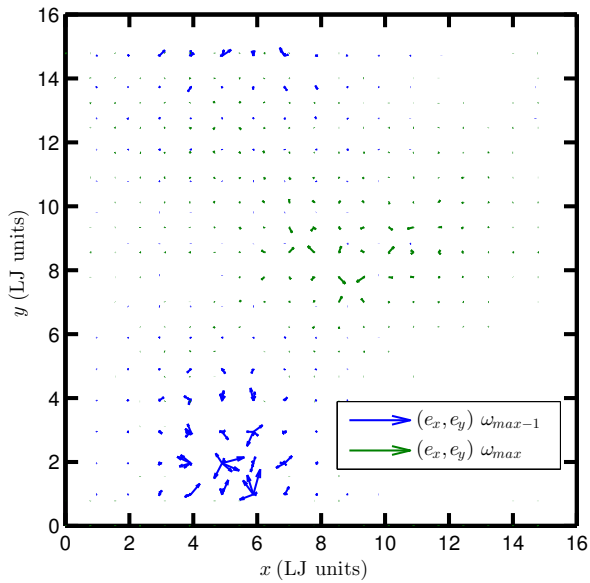


Figure A.8: Two-dimensional spatial components of the eigenvectors of the two highest frequency modes in a LJ alloy with $c = 0.5$. Both modes are locons as evidenced by their spatial localization.

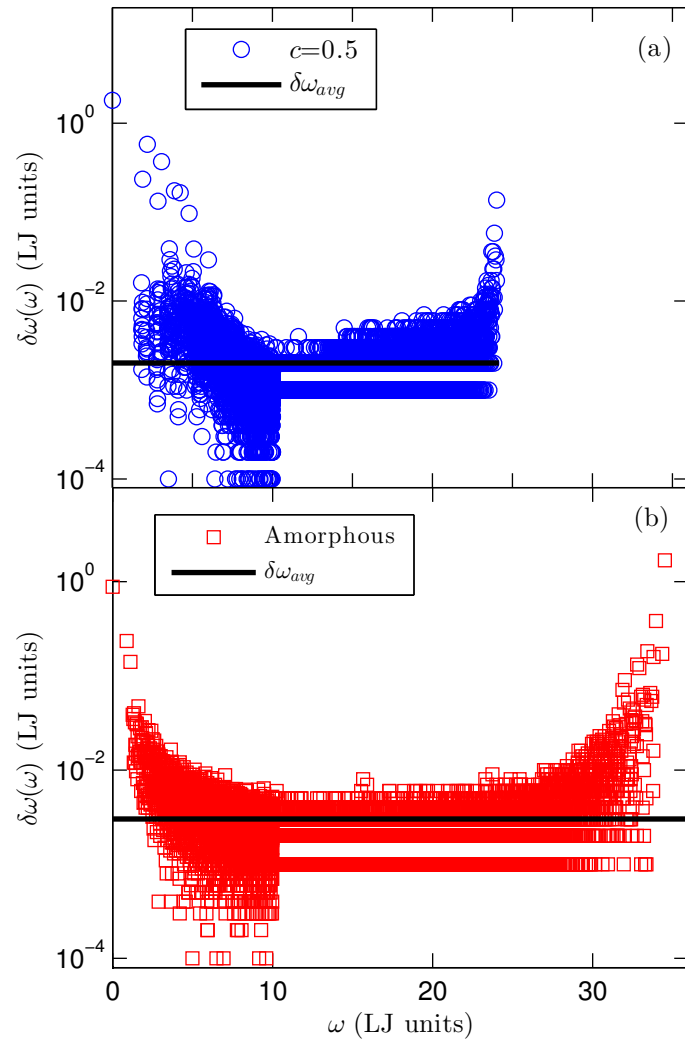


Figure A.9: The frequency spacing as a function of frequency for (a) the LJ alloy with a concentration of 0.5 and (b) the amorphous phase. For both systems there is a large variation of the frequency spacing, particularly at low and high frequencies where the spacings are up to two order of magnitude larger than the average frequency spacing $\delta\omega_{avg}$.

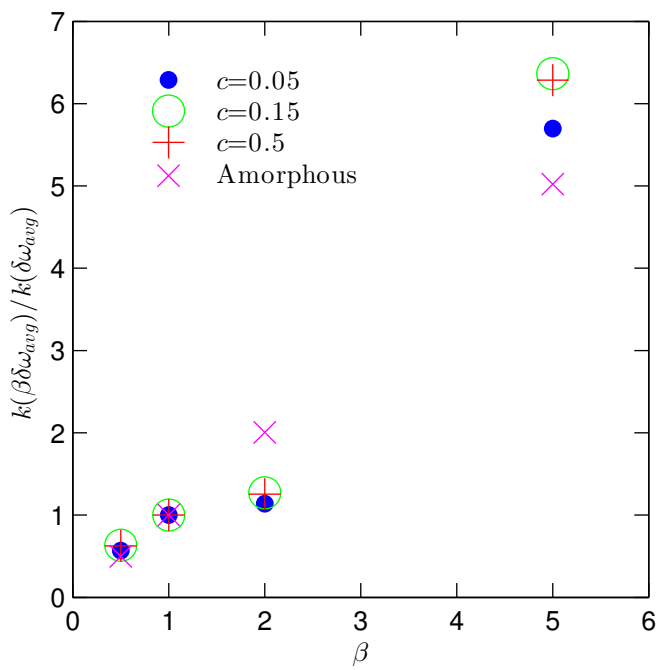


Figure A.10: The AF-predicted total thermal conductivity of LJ alloys and the amorphous phase as a function of the average broadening factor, given in increments of the average frequency spacing.

A.8 Spectral Density of Disordered Modes

There is not an accepted method to predict the group velocity of a vibrational mode in a disordered system, although there have been attempts [2, 62, 85, 102, 149, 151]. Calculating the structure factors of the supercell Gamma modes is a method to test for their propagating (i.e., plane-wave) character at a particular wavevector and polarization. This approach has been previously used to predict effective dispersion curves of disordered and amorphous materials experimentally [45, 53, 59, 61, 154, 168, 171, 172, 191, 192] and numerically [48, 52, 73, 75, 152, 153, 169, 170, 173, 175, 177, 178, 180, 193, 194, 195, 196, 197].

While the structure factor gives the frequency spectrum needed to construct a propagating state with pure wavevector κ , the individual mode spectra $E^T(\nu)$ and $E^L(\nu)$ [Eqs.(4.13) and (4.14)] predict the plane-wave character of each mode [73, 193]. It is not generally possible to assign a unique wavevector to individual modes, even at low frequency [73, 193], which makes predicting their group velocities challenging. The mode spectra E^L for three modes of the LJ alloy for a concentration of 0.5 are plotted in Fig. A.11, which demonstrates that it is not generally possible to assign a unique wavevector to individual modes in disordered systems. However, the mode spectra can be a useful tool for studying the plane-wave character of modes in ordered and disordered systems.

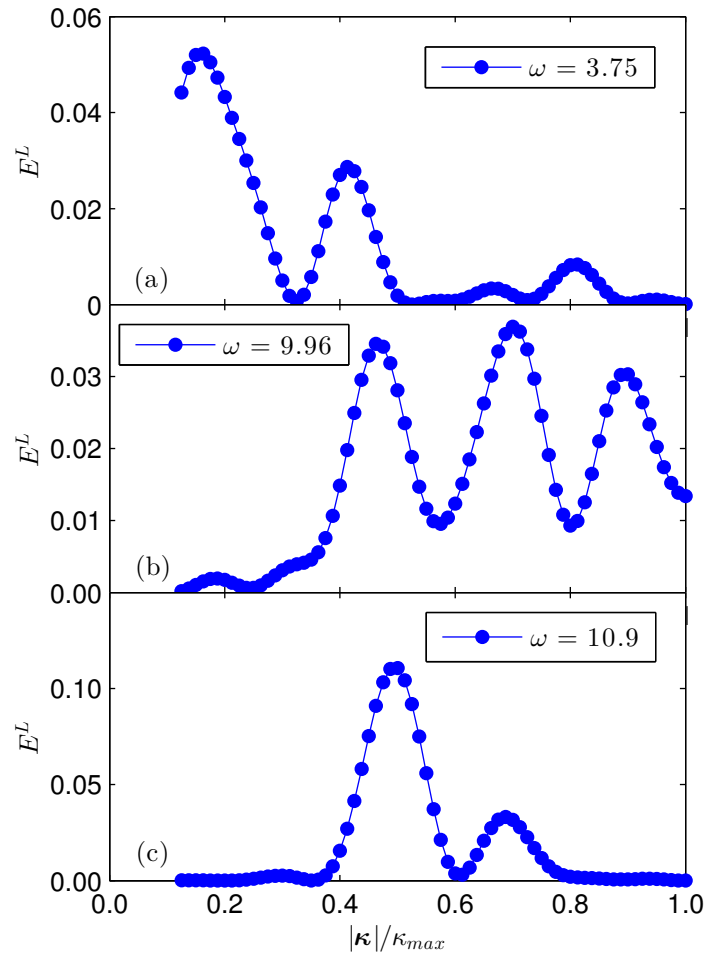


Figure A.11: Mode spectral densities E^L [Eq. (4.13)] for the LJ alloy with a concentration of $c = 0.5$. The wavevector is in the [100] direction (Fig. 3.3). The frequencies are in LJ units.

A.9 Accumulation Functions in Alloys

The thermal conductivity accumulation functions for the LJ argon and SW silicon alloys (Chapter 3) are predicted using Eq. (4.27) with $k_{AF} = 0$ and are plotted in Figs. A.12 and A.13. For both LJ and SW alloys, the thermal conductivity accumulations occur over a broader range of MFPs than the perfect crystals. This is due to the strong scaling of the phonon lifetimes with frequency of $\tau \propto \omega^{-4}$ (and even faster, Figs. 3.4 and 3.5) at low frequencies. This result suggests that nanostructuring may decrease the thermal conductivity of alloyed materials due to boundary scattering more significantly than perfect crystals, which has been investigated in other modeling work [37, 151]. The thermal conductivity accumulation for low-frequency dominated materials, such as SW silicon and its alloys, will be more sensitive to nanostructuring than full-spectrum materials, such as LJ argon and its alloys.

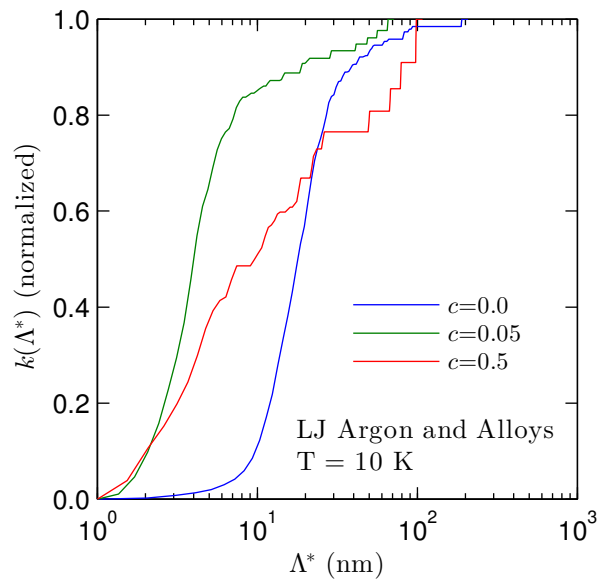


Figure A.12: Thermal conductivity accumulation functions for LJ argon and its alloys.

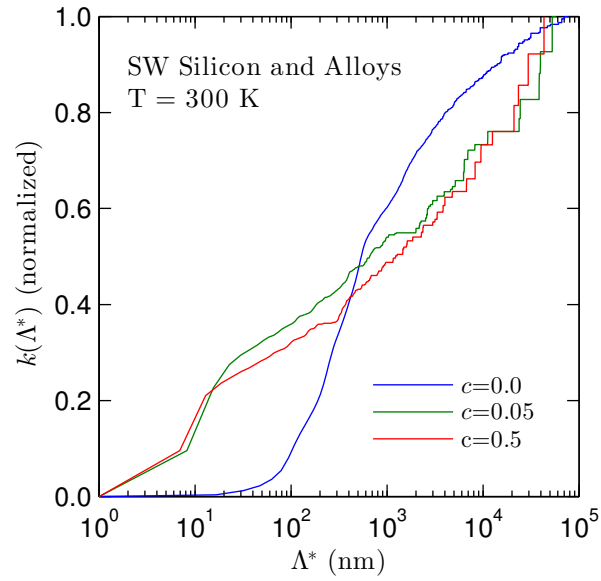


Figure A.13: Thermal conductivity accumulation functions for SW silicon and its alloys.

Appendix B

Research using High Performance Computing

B.1 Setting Up Computing Environment

B.1.1 Hardware and Operating System Choice

The choice of computing hardware determines which operating system(s) can be used. The three main choices for operating system are Windows, Apple OS, and Linux. Each operating system has limitations depending on the hardware it operates on. For example, Apple OS is primarily used on Apple hardware.

The Linux operating system is based on unix, which is the world's most widely used software. Linux runs on systems ranging from cell phones to the world's largest supercomputers. For personal computing use, the most widely used Linux version is Ubuntu. It is well-documented with a large community-based discussion system. Apple OS is an adequate substitute as it is unix-like.

There are many options for installing Ubuntu and the instructions can be found at ubuntu.com. Ubuntu is certified on PC's from many computer companies. One company, system 76, builds computers with Ubuntu pre-installed. I used the Pangolin Performance for over a year of my Ph.D. However, I recommend using the most-portable (i.e., lightest) and longest-battery life notebook available such as the Samsung Series 9 or Macbook Air. You will typically be using this notebook to access large computing clusters remotely, so there is a benefit of having portability and long battery life over computational power.

B.1.2 Terminal, Commands, and Environment Variables

These instructions work best for the Ubuntu operating system, and will work well for other versions of Linux. Systems commands are executed by the system terminal. The following Linux system commands have been used extensively throughout this work: sudo, cd, pwd, ls, export, echo, grep, sed, vi, cat, scp, ssh, which, nohup. There are many more Linux commands that are useful. More information can be obtained simply by google searching, i.e. google: linux sed

Environment variables, such as PATH, can store the paths to installed programs and files.

Here is how to determine what PATH is set to:

```
1 $ echo $PATH  
2 /opt/Datathief:/opt/VESTA-x86_64:/home/jason/phonopy/phonopy-1.1/bin:...
```

Permanent changes to environment variables can be made in the user's .bashrc file, which is typically located in the /home/user/ directory. The .bashrc file is a hidden file noted by its name starting with ". ". Here is an example .bashrc from Kevin Parrish. This file modifies environment variables such as PATH when a bash terminal session is launched. Changes to environment variables are made when a new terminal session is started.

Shell scripts are relatively low-level sets of system commands which can manipulate environment variables and the Linux operating system. Here is a simple tutorial on writing shell scripts. Running Linux system commands in Python can be an effective way of generating and manipulating many files with one script. Python is a more robust language than lower-level shell scripting. Here is an example that generates a series of shell scripts used to submit jobs on cluster resources (see next section). The Python script finds dummy variable names (SHELL_NAME and PROC_NAME) and replaces them with a different string.

B.1.3 Working on Remote Resources

At some point during research you will need to execute code on remote resources that are typically large computing clusters (> 100 central processing units). You will be provided with a terminal session similar to the session provided by Ubuntu with most of the same system commands. While I recommend Filezilla for handling the transfer of data and files, the functionality of Filezilla is contained in several shell commands: ssh and scp. Files can be transferred using the following command

```
1 $ scp -r user@gilgamesh.cheme.cmu.edu:/home/user/directory/ ./
```

which will place the “directory” and its contents into the pwd (./) of the local terminal session.

There are many variants of the operating systems used for remote computing clusters, but the differences are usually small. During my work I regularly used the gilgamesh computing cluster maintained by John Kitchin. Gilgamesh’s documentation is a good resource for learning how to run calculations on a computing cluster.

B.2 Installing, Writing and Executing Programs

B.2.1 Installing Available Packages

Before writing any of your own code, it is best to use any useful code that may already exist. Most Linux operating systems have automatic software installation. For Ubuntu, program management is achieved using the apt-get system command:

```
1 $ sudo apt-get install gfortran  
2 [sudo] password for jason:  
3 Reading package lists... Done  
4 ...
```

To check that the package has been installed, use:

```
1 $ which gfortran  
2 /usr/bin/gfortran
```

This shows that gfortran program is installed in the /usr/bin/ folder, a common location where automatically installed programs are located. Because the folder /usr/bin is in the PATH environment variable, the program gfortran is always available no matter where you are in the system terminal.

To get more information about the gfortran, use:

```
1 $ ls -l /usr/bin/gfortran  
2 lrwxrwxrwx 1 root root 12 Apr 22 03:44 /usr/bin/gfortran -> gfortran-4.7
```

where we see that /usr/bin/gfortran "points" to gfortran-4.7. This is called a symbolic link.

B.2.2 Available Packages for Thermal Transport Modeling

Available programs represent opportunities to perform research quickly and easily. I suggest reading their documentation carefully and trying the tutorials and examples, which are typically computationally inexpensive.

Most of the existing packages listed below cannot be installed using Ubuntu's apt-get command, although this feature does exist for LAMMPS and more packages are likely to be added in the future. It is important to read the installation documentation carefully. It is also helpful to contact any system Linux/Unix system administration staff or other researchers who are experienced with installing packages. These people can usually be found at campus or local computing centers, or in your own research group!

For a first-time user, I recommend trying to install the LAMMPS package as it is one of the easiest and most versatile. It has standard installation files for systems ranging from your personal computer up to a massively-parallel supercomputer. Installation instructions can be found [here](#).

Here is a partial list of the packages I have found useful in this work:

- LAMMPS, including the particularly useful mailing list and python interface: parallel molecular dynamics using empirical interatomic potentials.
- DL_POLY: parallel molecular dynamics using empirical interatomic potentials.
- GULP: harmonic lattice dynamics using empirical interatomic potentials.
- phonopy: harmonic lattice dynamics with interface for *ab initio* package.
- PHON: harmonic lattice dynamics with interface for *ab initio* package.
- ABINIT: *ab initio* package.
- Quantum Espresso: *ab initio* package.
- VASP: *ab initio* package.

- SIESTA: *ab initio* package.
- GAMESS: *ab initio* package.
- CP2K: *ab initio* package.
- BOLTZTRAP
- VMD (with topotools): structure and visualization.
- VESTA: structure and visualization.

I recommend trying this install.sh created by Kevin Parrish which installs many programs and packages, including LAMMPS for parallel computing with OpenMPI.

B.2.3 Writing Programs: Compiled versus Interpreted

If no package exists to perform the calculation you are interested in, there is a good chance you are doing something interesting! The next step is to implement the algorithm for the calculation you want to perform. There are two choices for doing this:

- Write your own code.
- Build off an existing package.

As outlined in the previous section, there are many pre-existing packages with many functionalities. The many packages that can perform nanoscale transport calculations use compiled and interpreted languages, often with a mixture of the two. The most commonly used compiled languages are C/C++ (e.g., Linux, LAMMPS) and Fortran (e.g., GULP, Quantum Espresso, VASP). Here is a good discussion on the strengths of C++ versus Fortran. Here are excellent tutorials of programming in C++ and Fortran. Learning these languages is essential to adding to existing packages.

Interpreted languages allow for fast code development and debugging. The two interpreted languages you are likely to use are Matlab and Python. The key to maximizing the potential of

interpreted languages is by using the built-in “vector” functions and operations provided by the Matlab and Python programming libraries. Matlab has an excellent built-in guide and google searches will typically yield useful results. An open-source substitute for Matlab is Octave, which is capable to running most Matlab scripts.

The following three case studies are performed on my local Samsung series 9 notebook. The specifications of the computer can be accessed by using:

```
1 $ cat /proc/cpuinfo
2 processor : 0
3 vendor_id : GenuineIntel
4 cpu family : 6
5 model    : 58
6 model name : Intel(R) Core(TM) i5-3317U CPU @ 1.70GHz
7 stepping : 9
8 microcode : 0x17
9 cpu MHz   : 782.000
10 cache size : 3072 KB
11 physical id : 0
12 siblings   : 4
13 core id    : 0
14 cpu cores  : 2
15 apicid     : 0
16 initial apicid : 0
```

B.2.3.1 Case-study (a): Optimizing Compiled Codes

The first case study is a single C code to perform molecular dynamics on LJ argon. The code uses simple subroutines and operates using a single (serial) processor. The arrays in this code are built statically. Arrays can be created dynamically, which allows for the input of systems with varying number of atoms. Additionally, vectors can be created and destroyed dynamically and have some advantages over arrays.

The code is compiled using the GNU project's C++ compiler, g++:

```
1 $ g++ ArgonMD.cpp -o ArgonMD_O_g++
```

The code can be run and the output can be directed using a useful shell operation called piping, which is demonstrated below:

```
1 $ ArgonMD_O_g++ > ./ArgonMD_O/output.txt
```

The code can be compiled using optimization flags, such as -O and -O3:

```
1 $ g++ -O3 ArgonMD.cpp -o ArgonMD_O3_g++
```

which greatly decreases the run time of this particular code. The total run time can be displayed by using the shell command grep, which shows for no optimization:

```
1 $ grep -A 1 "Total Time" ./ArgonMD/output.txt
```

```
2 Total Time: 38.42 (s)
```

for -O optimization:

```
1 $ grep -A 1 "Total Time" ./ArgonMD_O/output.txt
```

```
2 Total Time: 18.06 (s)
```

and for -O3 optimization:

```
1 $ grep -A 1 "Total Time" ./ArgonMD_O3/output.txt
```

```
2 Total Time: 11.74 (s)
```

A useful shell command is vi, a shell-based text editor, which can display the output within a shell terminal:

```
1 $ vi ./ArgonMD/output.txt  
2 0      1      5.61358 2.01864 5.26596  
3 ...
```

To compare with the above results, the LAMMPS code is compiled in serial using no , -O, and -O3 optimizations. The results are contained in folders beginning with “lmp”. A useful shell function is tab-twice, where tapping the tab key twice will display files and folders which begin with the same characters:

```
1 $ grep -A 1 "Loop time" ./lmp  
2 lmp.in.lj~      lmp_serial/      lmp_serial_O/  lmp_serial_O3/
```

The tab key can also be used for command-line completion to complete directory and file names.

The run time for no optimization is:

```
1 $ grep -A 1 "Loop time" ./lmp_serial/log.lammps  
2 Loop time of 0.718188 on 1 procs for 1000 steps with 256 atoms  
3 --  
4 Loop time of 3.4892 on 1 procs for 5000 steps with 256 atoms
```

for -O optimization:

```
1 $ grep -A 1 "Loop time" ./lmp_serial_O/log.lammps  
2 Loop time of 0.19842 on 1 procs for 1000 steps with 256 atoms  
3 --  
4 Loop time of 0.917175 on 1 procs for 5000 steps with 256 atoms
```

and for -O3 optimization:

```
1 $ grep -A 1 "Loop time" ./lmp_serial_O3/log.lammps
```

```

2 Loop time of 0.164066 on 1 procs for 1000 steps with 256 atoms
3 --
4 Loop time of 0.786311 on 1 procs for 5000 steps with 256 atoms

```

There is a decrease in run time with increasing optimization for LAMMPS and my code. However, for every optimization the LAMMPS code is approximately an order of magnitude faster. This result is due to a several factors, the most important being the implementation of neighbor lists as discussed in the LAMMPS documentation. The interested reader is encouraged to investigate the LAMMPS code further for useful C++ coding practices.

B.2.3.2 Case-study (b): Computational Cost of Interpreted Code

With interpreted languages, the traditional programming practice of using loops (for/do/while, etc) will slow the code execution. To illustrate this behavior, the case study compares codes to perform harmonic lattice dynamics calculations. One code is written in Matlab using mixture of loops and vectorized functions, which slows the code execution. The other code is written in Fortran (i.e., the GULP package).

From within a Matlab session in a terminal, the Matlab code can be executed as follows:

```

1 tic
2 [ freq , eigVsor ted , velocity ] = m_lj_1d_prim(1.5636*[1 1 1],[0.5 0.0 0.0])
3 toc
4 Elapsed time is 0.047081 seconds .

```

for the primitive, and

```

1 tic
2 [ freq , eigVsor ted , velocity ] = m_lj_1d_conv(1.5636*[1 1 1],[0.5 0.0 0.0])
3 toc
4 Elapsed time is 0.260508 seconds .

```

for the conventional unit cells. Note that the increased run time is not proportional to the increased number of atoms in the unit cell (i.e., the calculation does not scale linearly). Also note that the two codes both use for loops. This usage slows down code execution because Matlab is an interpreted language.

Now we run the same calculation using the Fortran-based GULP package, for the primitive:

```

1 $ grep -A 6 "Timing analysis" gulp_disp_lj_prim.gout
2 Timing analysis for GULP :
3
4
5 Task / Subroutine                                Time (Seconds)
6
7
8 Total CPU time                                  0.0030

```

and conventional unit cells:

```

1 $ grep -A 6 "Timing analysis" gulp_disp_lj_conv.gout
2 Timing analysis for GULP :
3
4 Task / Subroutine                                Time (Seconds)
5
6
7 Total CPU time                                  0.0160

```

First, the scaling of the calculation is non-linear. Second, the timing for both calculations is over an order of magnitude less than the Matlab versions. Matlab code can be optimized by using the built in vector operations and functions, which is demonstrated in the next section.

B.2.3.3 Case-study (c): Optimizing Interpreted Code

This case study demonstrates that Matlab (or other interpreted languages) can be optimized using the built-in vector functions and operations. This Matlab code performs the AF theory calculations on a LJ amorphous phase of 256 atoms. The code can be run from within a Matlab terminal using:

```
1 >> m_af_template  
2 ans =  
3 1.5075 (s)
```

which calls several subroutines, most notably `m_af_lj.m`, which uses all vectorized functions.

Comparing this result with the same calculation in GULP:

```
1 $ gulp x0_256  
2 $ grep -A 10 "Timing analysis" x0_256.gout  
3 Timing analysis for GULP :  
4  
5 Task / Subroutine                                Time (Seconds)  
6  
7 Calculation of real space energy and derivatives    0.0520  
8 Calculation of phonons                            18.5720  
9 Calculation of scattering                         0.0000  
10  
11 Total CPU time                                 19.3920  
12
```

The relevant subroutine in GULP to compare with the Matlab version is `thermalconductivity.f90`. The GULP timing is considerably larger than the Matlab code. This is due to the use of the default unoptimized BLAS and LAPACK libraries for linear algebra that were used to compile

GULP. During the installation, Matlab optimizes its linear algebra library, resulting in improved performance.

B.2.4 Scaling Calculations

The majority of the methods used in this work scale poorly with the number of atoms, N_a^α , with $\alpha > 1$. The scaling cost for eigenvalue solution is N_a^3 . The cost of performing this calculation for the largest system size, $cost_{large}$, and every successive system which is half the size of the largest is given by the geometric series with common ratio $r = 1/8$

$$cost_{total} = cost_{large} \frac{1}{1 - r} = 1.143 N_{a,large}. \quad (\text{B.1})$$

It costs a minimal amount ($\approx 14\%$) to study every system that is smaller than the largest system considered. Even a linear scaling has (with $r = 1/2$) a total cost $cost_{total} = 2cost_{large}$. As such, I recommend starting calculations with the smallest system of interest (i.e., the Minimum Working Example method). Journal article draft manuscripts can be developed quickly by performing computationally-inexpensive calculations first, documenting the results, and then iterating to more computationally-expensive calculations. This scheme for performing calculations can follow these time-scales for calculation costs:

- 1 second: exploratory work, debugging.
- 1 minute/1 hour: testing the scaling of algorithms, precision
- 1 day: publication-quality calculations
- 1 week: publication-quality calculations, but should be limited to when necessary.

I have performed countless calculations costing around one second, and very few which cost more than one week. Publication quality results will typically cost between one hour and one week.

B.3 Preparing Journal Articles and Thesis

The job of the student is to prepare, submit, and publish peer-reviewed journal articles. There are many journals suitable for nanoscale transport topics. All of them accept Latex prepared manuscripts. I recommend the Latex editor Kile, while the simple gedit works well and comes pre-installed with Ubuntu. Here is a simple latex example and how to generate a portable document format (PDF) from the latex document.

I recommend editing a written research document at least once every week. The exchange of such a document with the advisor can be facilitated using Dropbox or Github. Github offers advantages over Dropbox, such as version control and a built-in online wiki. Such a research document can turn into journal articles, which then turn into the thesis.

To maintain the reference library I recommend zotero. Here is an example reference.bib file which is exported automatically by zotero. The references are generated from the latex document using bibtex, which compiles the contents of the reference.bib.

Here is an example of the latex file used to create an article published from this work. This file uses revtex, which is an article class used by *Physical Review*, *Journal of Applied Physics*, and others. Here is a Carnegie Mellon thesis template, which was used to create this thesis document.

B.4 Technical Advice

In addition to your advisor and close mentors, I recommend communicating with experts in the field as much as possible (without being annoying). How often to communicate depends on the situation. It is best to let the expert dictate the pace of the conversation. Here is a list of experts I used as resources for this work. They will typically answer emails within 24-48 hours:

- Wissam Al-Saidi

- Davide Donadio
- John Duda
- Keivan Esfarjani
- Joseph Feldman
- Julian Gale, (GULP author)
- Jivtesh Garg
- Ankit Jain
- John Kitchin
- Axel Kolhmeyer via the LAMMPS mailing list and email
- Jason Larkin
- Jon Malen
- Craig Maloney
- Alan McGaughey
- Normand Mousseau
- Steve Plimpton via the LAMMPS mailing list
- Guido Raos
- Dan Sellan
- Junchiyo Shiomi
- Atz Togo, creator of phonopy

Bibliography

- [1] J. E. Graebner, B. Golding, and L. C. Allen. Phonon localization in glasses. *Phys. Rev. B*, 34(8):56965701, October 1986. 1, 2, 3, 36, 68, 72, 73, 74, 103, 107
- [2] D.G. Cahill and RO Pohl. Lattice vibrations and heat transport in crystals and glasses. *Annual Review of Physical Chemistry*, 39(1):93121, 1988. 1, 2, 3, 36, 39, 41, 45, 57, 68, 72, 73, 90, 96, 98, 103, 107, 142
- [3] X. Lu, M. C. Arduini-Schuster, J. Kuhn, O. Nilsson, J. Fricke, and R. W. Pekala. Thermal conductivity of monolithic organic aerogels. *Science*, 255(5047):971972, 1992. 1, 36
- [4] G Chen, M S Dresselhaus, G Dresselhaus, J Fleurial, and T Caillat. Recent developments in thermoelectric materials. *International Materials Reviews*, 48(1):4566, 2003. 1, 2, 36
- [5] David R. Clarke and Simon R. Phillipot. Thermal barrier coating materials. *Materials Today*, 8(6):22–29, June 2005. 1, 36
- [6] G. J. Snyder and E. S. Toberer. Complex thermoelectric materials. *Nature Materials*, 7:105114, 2008. 1, 2, 36
- [7] A. J. Minnich, M. S. Dresselhaus, Z. F. Ren, and G. Chen. Bulk nanostructured thermoelectric materials: current research and future prospects. *Energy Environ. Sci.*, 2(5):, 2009. 1, 36
- [8] Eric S. Toberer, Alex Zevalkink, and G. Jeffrey Snyder. Phonon engineering through crystal chemistry. *J. Mater. Chem.*, 21(40), 2011. 1, 2, 36

- [9] M. Zebarjadi, K. Esfarjani, M. S. Dresselhaus, Z. F. Ren, and G. Chen. Perspectives on thermoelectrics: from fundamentals to device applications. *Energy Environ. Sci.*, 5(1):51475162, 2012. 1, 2, 36
- [10] Scott N. Schiffres, Kyu Hun Kim, Lin Hu, Alan J. H. McGaughey, Mohammad F. Islam, and Jonathan A. Malen. Gas diffusion, energy transport, and thermal accommodation in single-walled carbon nanotube aerogels. *Advanced Functional Materials*, page DOI:10.1002/adfm.201201285, 2012. 1, 36
- [11] John C. Duda, Patrick E. Hopkins, Yang Shen, and Mool C. Gupta. Exceptionally low thermal conductivities of films of the fullerene derivative PCBM. *Phys. Rev. Lett.*, 110(1):015902, January 2013. 1, 111, 112
- [12] J. E. Turney, E. S. Landry, A. J. H. McGaughey, and C. H. Amon. Predicting phonon properties and thermal conductivity from anharmonic lattice dynamics calculations and molecular dynamics simulations. *Physical Review B*, 79:064301, 2009. xxi, 1, 5, 6, 7, 9, 13, 14, 15, 17, 20, 25, 26, 29, 30, 41, 50, 52, 60, 88, 134
- [13] A. J. H. McGaughey, E. S. Landry, D. P. Sellan, and C. H. Amon. Size-dependent model for thin film and nanowire thermal conductivity. *Applied Physics Letters*, 99:131904, 2011. 1, 14, 33
- [14] Alan J. H. McGaughey and Ankit Jain. Nanostructure thermal conductivity prediction by monte carlo sampling of phonon free paths. *Applied Physics Letters*, 100(6):061911, 2012. 1
- [15] Keith T. Regner, Daniel P. Sellan, Zonghui Su, Cristina H. Amon, Alan J. H. McGaughey, and Jonathan A. Malen. Broadband phonon mean free path contributions to thermal conductivity measured using frequency domain thermoreflectance. *Nat Commun*, 4:1640, March 2013. xviii, 1, 2, 3, 12, 71, 72, 96, 98, 99, 100, 101, 102, 103
- [16] A. A. Maradudin. Dynamical properties of solids, volume 1. In G. K. Horton and A. A.

Maradudin, editors, *Dynamical Properties of Solids, Volume 1*, page 182. Elsevier, New York, 1974. 1, 2, 6, 14, 16, 116

- [17] D. C. Wallace. *Thermodynamics of Crystals*. Cambridge Univ. Press, Cambridge, UK, 1972. 1, 2, 6, 14, 16, 115, 116
- [18] G. P. Srivastava. *The Physics of Phonons*. Adam Hilger, Bristol, 1990. 1, 6, 14, 16, 116, 130
- [19] M. T. Dove. *Introduction to Lattice Dynamics*. Cambridge, Cambridge, 1993. 1, 14, 16, 19, 20, 21, 48, 74, 82, 88, 115, 120
- [20] J. M. Ziman. *Electrons and Phonons*. Oxford, New York, 2001. 1, 3, 21, 36, 38, 52, 74, 75, 76, 97, 117
- [21] J. Callaway. Model for lattice thermal conductivity at low temperatures. *Physical Review*, 113:1046, 1959. 1, 6, 14, 40, 51, 76, 125
- [22] M. G. Holland. Analysis of lattice thermal conductivity. *Physical Review*, 132:2461, 1963. 1, 6, 14
- [23] P. G. Klemens. The scattering of low-frequency lattice waves by static imperfections. *Proceedings of the Physical Society. Section A*, 68(1113), 1955. 1, 2, 6, 40, 41, 51, 54, 76
- [24] Glen A. Slack. The thermal conductivity of nonmetallic crystals. volume 34 of *Solid State Physics*, page 1–71. Academic Press, 1979. 1, 3, 6
- [25] J. D. Chung, A. J. H. McGaughey, and M. Kaviany. Role of phonon dispersion in lattice thermal conductivity analysis. *Journal of Heat Transfer*, 126:376380, 2004. 2, 6
- [26] D. A. Broido, M. Maloney, G. Birner, N. Mingo, and D. Stewart. Intrinsic lattice thermal conductivity of semiconductors from first principles. *Applied Physics Letters*, 91:231922, 2007. 2, 6, 14, 36, 38
- [27] A. Ward, D. A. Broido, Derek A. Stewart, and G. Deinzer. Ab initio theory of the lattice

thermal conductivity in diamond. *Phys. Rev. B*, 80(12):125203, September 2009. 2, 6, 37, 39

- [28] A. Ward and D. A. Broido. Intrinsic phonon relaxation times from first-principles studies of the thermal conductivities of si and ge. *Phys. Rev. B*, 81(8):085205, February 2010. 2, 6, 36, 38, 68
- [29] Keivan Esfarjani, Gang Chen, and Harold T. Stokes. Heat transport in silicon from first-principles calculations. *Physical Review B*, 84(8):085204, August 2011. 2, 5, 6, 9, 14, 36, 41, 60, 64, 68, 96, 112, 125, 134
- [30] L. Lindsay, D. A. Broido, and T. L. Reinecke. Thermal conductivity and large isotope effect in GaN from first principles. *Phys. Rev. Lett.*, 109(9):095901, August 2012. 2, 6, 36, 37, 39, 40, 41, 64, 68, 106
- [31] Takuma Shiga, Junichiro Shiomi, Jie Ma, Olivier Delaire, Tomasz Radzynski, Andrzej Lusakowski, Keivan Esfarjani, and Gang Chen. Microscopic mechanism of low thermal conductivity in lead telluride. *Phys. Rev. B*, 85(15):155203, April 2012. 2, 36, 41, 68
- [32] Maria N. Luckyanova, Jivtesh Garg, Keivan Esfarjani, Adam Jndl, Mayank T. Bulsara, Aaron J. Schmidt, Austin J. Minnich, Shuo Chen, Mildred S. Dresselhaus, Zhifeng Ren, Eugene A. Fitzgerald, and Gang Chen. Coherent phonon heat conduction in superlattices. *Science*, 338(6109):936939, 2012. 2, 7, 36, 41, 68, 106
- [33] L. Lindsay, D. A. Broido, and T. L. Reinecke. First-principles determination of ultrahigh thermal conductivity of boron arsenide: A competitor for diamond? *Phys. Rev. Lett.*, 111(2):025901, July 2013. 2, 6
- [34] B. Abeles. Lattice thermal conductivity of disordered semiconductor alloys at high temperatures. *Physical Review*, 131(5):19061911, September 1963. 2, 36, 37, 40, 41, 68
- [35] Shin-ichiro Tamura. Isotope scattering of dispersive phonons in ge. *Phys. Rev. B*, 27(2):858866, January 1983. 2, 6, 36, 37, 41, 51, 54, 55, 65

- [36] Junichiro Shiomi, Keivan Esfarjani, and Gang Chen. Thermal conductivity of half-heusler compounds from first-principles calculations. *Physical Review B*, 84(10):125209, 2011. 2, 5, 7, 9, 15, 17, 18, 24, 33, 36, 60, 68, 96, 112, 120, 134
- [37] Zhiting Tian, Jivtesh Garg, Keivan Esfarjani, Takuma Shiga, Junichiro Shiomi, and Gang Chen. Phonon conduction in PbSe, PbTe, and PbTe_{1-x}Se_x from first-principles calculations. *Phys. Rev. B*, 85(18):184303, May 2012. 2, 7, 36, 37, 40, 41, 52, 55, 64, 68, 106, 144
- [38] Wu Li, L. Lindsay, D. A. Broido, Derek A. Stewart, and Natalio Mingo. Thermal conductivity of bulk and nanowire Mg₂Si_xSn_{1-x} alloys from first principles. *Phys. Rev. B*, 86(17):174307, November 2012. 2, 6, 36, 37, 41, 55, 68, 106
- [39] Jivtesh Garg, Nicola Bonini, Boris Kozinsky, and Nicola Marzari. Role of disorder and anharmonicity in the thermal conductivity of silicon-germanium alloys: A first-principles study. *Phys. Rev. Lett.*, 106(4):045901, January 2011. 2, 6, 36, 37, 38, 40, 41, 44, 52, 55, 64, 65, 68, 106, 135
- [40] A. Kundu, N. Mingo, D. A. Broido, and D. A. Stewart. Role of light and heavy embedded nanoparticles on the thermal conductivity of SiGe alloys. *Phys. Rev. B*, 84(12):125426, September 2011. 2, 7
- [41] Zhiting Tian, Keivan Esfarjani, and Gang Chen. Enhancing phonon transmission across a Si/Ge interface by atomic roughness: First-principles study with the green's function method. *Phys. Rev. B*, 86(23):235304, December 2012. 2, 7, 40
- [42] Walter Schirmacher, Gregor Diezemann, and Carl Ganter. Harmonic vibrational excitations in disordered solids and the Boson peak. *Phys. Rev. Lett.*, 81(1):136139, July 1998. 2
- [43] W. Schirmacher, G. Ruocco, and T. Scopigno. Acoustic attenuation in glasses and its relation with the boson peak. *Phys. Rev. Lett.*, 98(2):025501, January 2007. 2, 76

- [44] A. I. Chumakov, G. Monaco, A. Monaco, W. A. Crichton, A. Bosak, R. Rffer, A. Meyer, F. Kargl, L. Comez, D. Fioretto, H. Giefers, S. Roitsch, G. Wortmann, M. H. Manghnani, A. Hushur, Q. Williams, J. Balogh, K. Parlifmmode \acutent\else\fiski, P. Jochym, and P. Piekarz. Equivalence of the boson peak in glasses to the transverse acoustic van hove singularity in crystals. *Phys. Rev. Lett.*, 106(22):225501, May 2011. 2
- [45] Francesco Sette, Michael H. Krisch, Claudio Masciovecchio, Giancarlo Ruocco, and Giulio Monaco. Dynamics of glasses and glass-forming liquids studied by inelastic x-ray scattering. *Science*, 280(5369):1550–1555, 1998. 2, 82, 142
- [46] B. L. Zink, R. Islam, David J. Smith, and F. Hellman. Excess modes and enhanced scattering in rare-earth-doped amorphous silicon thin films. *Phys. Rev. B*, 74(20):205209, November 2006. 2, 73, 100, 103
- [47] Philip B. Allen and Joseph L. Feldman. Thermal conductivity of disordered harmonic solids. *Physical Review B*, 48(17):1258112588, November 1993. 2, 3, 4, 7, 39, 57, 58, 68, 72, 73, 77, 138
- [48] Joseph L. Feldman, Mark D. Kluge, Philip B. Allen, and Frederick Wooten. Thermal conductivity and localization in glasses: Numerical study of a model of amorphous silicon. *Physical Review B*, 48(17):1258912602, November 1993. 2, 3, 7, 36, 39, 48, 55, 58, 72, 73, 74, 75, 76, 77, 80, 82, 83, 89, 90, 92, 93, 97, 98, 100, 103, 106, 107, 121, 138, 142
- [49] J. J. Freeman and A. C. Anderson. Thermal conductivity of amorphous solids. *Phys. Rev. B*, 34(8):56845690, October 1986. 2, 3, 72, 73, 74, 103
- [50] M. S. Love and A. C. Anderson. Estimate of phonon thermal transport in amorphous materials above 50 k. *Phys. Rev. B*, 42(3):18451847, July 1990. 2, 72, 73, 74, 75, 97, 102, 103
- [51] David G. Cahill, M. Katiyar, and J. R. Abelson. Thermal conductivity of *a* -Si:H thin films. *Phys. Rev. B*, 50(9):60776081, September 1994. xviii, 2, 72, 73, 74, 75, 76, 92, 97,

98, 99, 100, 101, 103

- [52] Joseph L. Feldman, Philip B. Allen, and Scott R. Bickham. Numerical study of low-frequency vibrations in amorphous silicon. *Phys. Rev. B*, 59(5):35513559, February 1999. 2, 3, 7, 39, 45, 47, 48, 58, 72, 73, 74, 75, 76, 77, 78, 80, 82, 83, 89, 93, 97, 98, 100, 103, 106, 107, 121, 132, 142
- [53] G. Baldi, V. M. Giordano, G. Monaco, F. Sette, E. Fabiani, A. Fontana, and G. Ruocco. Thermal conductivity and terahertz vibrational dynamics of vitreous silica. *Phys. Rev. B*, 77(21):214309, June 2008. 2, 3, 72, 73, 74, 75, 82, 83, 90, 97, 102, 103, 142
- [54] Xiao Liu, J. L. Feldman, D. G. Cahill, R. S. Crandall, N. Bernstein, D. M. Photiadis, M. J. Mehl, and D. A. Papaconstantopoulos. High thermal conductivity of a hydrogenated amorphous silicon film. *Phys. Rev. Lett.*, 102(3):035901, January 2009. xviii, 2, 3, 72, 73, 74, 75, 76, 86, 97, 98, 99, 100, 101, 103
- [55] Ho-Soon Yang, David G. Cahill, X. Liu, J. L. Feldman, R. S. Crandall, B. A. Sperling, and J. R. Abelson. Anomalously high thermal conductivity of amorphous si deposited by hot-wire chemical vapor deposition. *Phys. Rev. B*, 81(10):104203, March 2010. xviii, 2, 3, 72, 73, 74, 75, 76, 97, 98, 99, 100, 101, 103
- [56] B L Zink, R Pietri, and F Hellman. Thermal conductivity and specific heat of thin-film amorphous silicon. *Physical Review Letters*, 96(5):055902, 2006. 2, 73, 100, 103
- [57] D. B. Hondongwa, B. C. Daly, T. B. Norris, B. Yan, J. Yang, and S. Guha. Ultrasonic attenuation in amorphous silicon at 50 and 100 GHz. *Phys. Rev. B*, 83(12):121303, March 2011. 2, 73, 92, 114
- [58] C. Masciovecchio, G. Baldi, S. Caponi, L. Comez, S. Di Fonzo, D. Fioretto, A. Fontana, A. Gessini, S. C. Santucci, F. Sette, G. Viliani, P. Vilmercati, and G. Ruocco. Evidence for a crossover in the frequency dependence of the acoustic attenuation in vitreous silica. *Phys. Rev. Lett.*, 97(3):035501, July 2006. 2, 3, 73, 76, 92, 102, 114

- [59] G. Baldi, V. M. Giordano, G. Monaco, and B. Ruta. Sound attenuation at terahertz frequencies and the boson peak of vitreous silica. *Phys. Rev. Lett.*, 104(19):195501, May 2010. 3, 73, 76, 82, 83, 92, 102, 103, 114, 142
- [60] Giacomo Baldi, Valentina M. Giordano, and Giulio Monaco. Elastic anomalies at terahertz frequencies and excess density of vibrational states in silica glass. *Phys. Rev. B*, 83(17):174203, May 2011. 3, 73, 76, 92, 103
- [61] G. Baldi, M. Zanatta, E. Gilioli, V. Milman, K. Refson, B. Wehinger, B. Winkler, A. Fontana, and G. Monaco. Emergence of crystal-like atomic dynamics in glasses at the nanometer scale. *Phys. Rev. Lett.*, 110(18):185503, May 2013. 3, 73, 76, 82, 83, 92, 102, 103, 114, 142
- [62] Yuping He, Davide Donadio, and Giulia Galli. Heat transport in amorphous silicon: Interplay between morphology and disorder. *Applied Physics Letters*, 98(14):144101, 2011. 3, 5, 7, 9, 45, 50, 72, 73, 74, 76, 78, 84, 88, 89, 90, 93, 96, 97, 98, 106, 107, 108, 110, 132, 142
- [63] G. Pompe and E. Hegenbarth. Thermal conductivity of amorphous si at low temperatures. *physica status solidi (b)*, 147(1):103–108, May 1988. 3, 73
- [64] L. Wieczorek, H.J. Goldsmid, and G.L. Paul. Thermal conductivity of amorphous films. In D.P.H. Hasselman and Jr. Thomas, J.R., editors, *Thermal Conductivity 20*, pages 235–241. Springer US, 1989. xviii, 3, 73, 101
- [65] B. S. W. Kuo, J. C. M. Li, and A. W. Schmid. Thermal conductivity and interface thermal resistance of si film on si substrate determined by photothermal displacement interferometry. *Applied Physics A: Materials Science & Processing*, 55(3):289296, 1992. 10.1007/BF00348399. xviii, 3, 73, 99, 101
- [66] Hiroshi Wada and Takeshi Kamijoh. Thermal conductivity of amorphous silicon. *Japanese Journal of Applied Physics*, 35(Part 2, No. 5B):L648L650, 1996. xviii, 3, 73,

99, 101

- [67] Seungjae Moon, Mutsuko Hatano, Minghong Lee, and Costas P. Grigoropoulos. Thermal conductivity of amorphous silicon thin films. *International Journal of Heat and Mass Transfer*, 45(12):2439–2447, 2002. xviii, 3, 73, 99, 101
- [68] R. C. Zeller and R. O. Pohl. Thermal conductivity and specific heat of noncrystalline solids. *Phys. Rev. B*, 4(6):20292041, September 1971. 3, 73
- [69] David G. Cahill and R. O. Pohl. Heat flow and lattice vibrations in glasses. *Solid State Communications*, 70(10):927–930, 1989. 3, 73, 103
- [70] S.-M. Lee and D. G. Cahill. Heat transport in thin dielectric films. *Journal of Applied Physics*, 81:25902595, 1997. xviii, 3, 14, 72, 96, 98, 100, 101, 102
- [71] Tsuneyuki Yamane, Naoto Nagai, Shin-ichiro Katayama, and Minoru Todoki. Measurement of thermal conductivity of silicon dioxide thin films using a 3 omega method. *Journal of Applied Physics*, 91(12):97729776, 2002. xviii, 3, 72, 96, 98, 100, 101, 102
- [72] C. Kittel. Interpretation of the thermal conductivity of glasses. *Physical Review*, 75:974, 1949. 3, 68, 107
- [73] P. B. Allen, J. L. Feldman, J. Fabian, and F. Wooten. Diffusons, locons, and propagons: character of atomic vibrations in amorphous si. *Philosophical Magazine B*, 79:17151731, 1999. xiii, 3, 4, 36, 47, 48, 68, 72, 80, 82, 83, 84, 89, 94, 102, 107, 121, 142
- [74] Rubina Sultan, A. D. Avery, J. M. Underwood, S. J. Mason, D. Bassett, and B. L. Zink. Heat transport by long mean free path vibrations in amorphous silicon nitride near room temperature. *Phys. Rev. B*, 87(21):214305, June 2013. 3, 72
- [75] S. N. Taraskin and S. R. Elliott. Determination of the ioffe-regel limit for vibrational excitations in disordered materials. *Philosophical Magazine Part B*, 79(11-12):17471754, 1999. xv, 4, 51, 53, 68, 76, 82, 83, 89, 107, 121, 125, 142
- [76] Ashton Skye and Patrick K. Schelling. Thermal resistivity of SiGe alloys by molecular-

- dynamics simulation. *Journal of Applied Physics*, 103(11):113524, 2008. 5, 40
- [77] E. S. Landry, M. I. Hussein, and A. J. H. McGaughey. Complex superlattice unit cell designs for reduced thermal conductivity. *Physical Review B*, 77:184302, 2008. 5, 14, 60
- [78] E. S. Landry and A. J. H. McGaughey. Effect of interfacial species mixing on phonon transport in semiconductor superlattices. *Physical Review B*, 79:075316, 2009. 5, 14
- [79] E. S. Landry. *Thermal transport by phonons across semiconductor interfaces, thin films, and superlattices*. PhD thesis, Carnegie Mellon University, Pittsburgh, PA, 2009. 5, 14, 40
- [80] J. A. Thomas, R. M. Iutzi, and A. J. H. McGaughey. Thermal conductivity and phonon transport in empty and water-filled carbon nanotubes. *Physical Review B*, 81:045413, 2010. 5
- [81] A. J. H. McGaughey and M. Kaviany. Quantitative validation of the boltzmann transport equation phonon thermal conductivity model under the single-mode relaxation time approximation. *Physical Review B*, 69:094303, 2004. 5, 7, 9, 14, 17, 20, 22, 23, 29, 39, 48, 60, 75, 88, 134
- [82] A. J. H. McGaughey and M. Kaviany. Thermal conductivity decomposition and analysis using molecular dynamics simulations. part II. complex silica structures. *International Journal of Heat and Mass Transfer*, 47:17991816, 2004. xvi, 5, 77, 80, 81, 83, 96, 102, 111
- [83] Yuping He, Ivana Savic, Davide Donadio, and Giulia Galli. Lattice thermal conductivity of semiconducting bulk materials: atomistic simulations. *Phys. Chem. Chem. Phys.*, 14(47):16209–16222, 2012. 5, 7, 9, 43, 50, 60, 88, 89
- [84] Yuping He, Davide Donadio, and Giulia Galli. Morphology and temperature dependence of the thermal conductivity of nanoporous SiGe. *Nano Letters*, 11(9):3608–3611, August 2011. 5, 7, 9, 50, 64, 84, 88, 93, 107, 108, 110

- [85] Yuping He, Davide Donadio, Joo-Hyoung Lee, Jeffrey C. Grossman, and Giulia Galli. Thermal transport in nanoporous silicon: Interplay between disorder at mesoscopic and atomic scales. *ACS Nano*, 5(3):18391844, 2011. xxi, 5, 7, 9, 14, 17, 30, 45, 60, 84, 88, 93, 107, 108, 110, 134, 142
- [86] D. A. McQuarrie. *Statistical Mechanics*. University Science Books, Sausalito, 2000. 5, 22, 25, 29, 30, 31, 39, 75, 79
- [87] Alan J. H. McGaughey. *Phonon transport in molecular dynamics simulations: Formulation and thermal conductivity prediction*. PhD thesis, University of Michigan, Ann Arbor, MI, 2004. 5, 8, 26, 30, 43, 52, 111, 123
- [88] J. E. Turney, A. J. H. McGaughey, and C. H. Amon. Assessing the applicability of quantum corrections to classical thermal conductivity predictions. *Physical Review B*, 79:224305, 2009. 5, 7, 14
- [89] Richard M Martin. *Electronic structure: basic theory and practical methods*. Cambridge university press, 2004. 5
- [90] P. G. Klemens. Thermal resistance due to isotopic mass variation. *Proceedings of the Physical Society. Section A*, 70(11):833, 1957. 6, 40, 41, 51, 54
- [91] Daniel Charles Mattis. Phonon free path in an isotopic mixture. *Phys. Rev.*, 107(6):17361736, September 1957. 6, 40, 41, 51, 54
- [92] K. Esfarjani and H. T. Stokes. Method to extract anharmonic force constants from first principles calculations. *Physical Review B*, 77:144112, 2008. 6, 64
- [93] Ping Sheng and Minyao Zhou. Heat conductivity of amorphous solids: Simulation results on model structures. *Science*, 253(5019):539542, 1991. 7, 59, 68, 89, 92
- [94] Ping Sheng. *Introduction to Wave Scattering: Localization and Mesoscopic Phenomena*. Springer, April 2006. 7, 58
- [95] Vincenzo Vitelli, Ning Xu, Matthieu Wyart, Andrea J. Liu, and Sidney R. Nagel. Heat

- transport in model jammed solids. *Phys. Rev. E*, 81(2):021301, February 2010. 7, 58, 59, 68, 76, 92
- [96] S. R. Bickham and J. L. Feldman. Calculation of vibrational lifetimes in amorphous silicon using molecular dynamics simulations. *Phys. Rev. B*, 57(19):1223412238, May 1998. 7, 89, 90, 111
- [97] S. R. Bickham. Numerical calculation of relaxation rates in amorphous silicon. *Phys. Rev. B*, 59(7):48944897, February 1999. 7, 89, 90, 111
- [98] Jaroslav Fabian, Joseph L. Feldman, C. Stephen Hellberg, and S. M. Nakhmanson. Numerical study of anharmonic vibrational decay in amorphous and paracrystalline silicon. *Phys. Rev. B*, 67(22):224302, June 2003. 7, 89, 90
- [99] A. J. C. Ladd, B. Moran, and W. G. Hoover. Lattice thermal conductivity: A comparison of molecular dynamics and anharmonic lattice dynamics. *Physical Review B*, 34:50585064, 1986. 7, 9, 14, 15, 17, 48, 51, 88
- [100] Davide Donadio and Giulia Galli. Thermal conductivity of isolated and interacting carbon nanotubes: Comparing results from molecular dynamics and the boltzmann transport equation. *Phys. Rev. Lett.*, 99(25):255502, December 2007. 7, 9
- [101] A. S. Henry and G. Chen. Spectral phonon transport properties of silicon based on molecular dynamics simulations and lattice dynamics. *Journal of Computational and Theoretical Nanoscience*, 5:112, 2008. 7, 9, 14, 17, 88
- [102] Davide Donadio and Giulia Galli. Atomistic simulations of heat transport in silicon nanowires. *Phys. Rev. Lett.*, 102(19):195901, May 2009. 7, 9, 45, 50, 80, 84, 107, 108, 110, 142
- [103] J. V. Goicochea, M. Madrid, and C. H. Amon. Thermal properties for bulk silicon based on the determination of relaxation times using molecular dynamics. *Journal of Heat Transfer*, 132:012401, 2010. 7, 9, 14, 17, 22, 39, 43

- [104] Gabriele C. Sosso, Davide Donadio, Sebastiano Caravati, Jrg Behler, and Marco Bernasconi. Thermal transport in phase-change materials from atomistic simulations. *Phys. Rev. B*, 86(10):104301, September 2012. 7, 9, 37
- [105] Bo Qiu, Hua Bao, Gengqiang Zhang, Yue Wu, and Xiulin Ruan. Molecular dynamics simulations of lattice thermal conductivity and spectral phonon mean free path of PbTe: bulk and nanostructures. *Computational Materials Science*, 53(1):278–285, 2012. 7, 9
- [106] Yaguo Wang, Bo Qiu, Alan J. H. McGaughey, Xiulin Ruan, and Xianfan Xu. Mode-wise thermal conductivity of bismuth telluride. *Journal of Heat Transfer*, 135(9):091102–091102, July 2013. 7, 9
- [107] N. de Koker. Thermal conductivity of MgO periclase from equilibrium first principles molecular dynamics. *Physical Review Letters*, 103:125902, 2009. 9, 15, 33, 112, 120
- [108] Baoling Huang and Massoud Kaviany. Filler-reduced phonon conductivity of thermoelectric skutterudites: Ab initio calculations and molecular dynamics simulations. *Acta Materialia*, 58(13):4516–4526, 2010. 9, 112
- [109] Bao-Ling Huang and Massoud Kaviany. Ab initio and molecular dynamics predictions for electron and phonon transport in bismuth telluride. *Physical Review B (Condensed Matter and Materials Physics)*, 77(12):125209, 2008. 9, 112
- [110] T. Luo and J. R. Lloyd. Molecular dynamics study of thermal transport in GaAs-self-assembly monolayer-GaAs junctions with ab initio characterization of thiol-GaAs bonds. *Journal of Applied Physics*, 109:034301, 2011. 9, 112
- [111] J. E. Turney. *Predicting phonon properties and thermal conductivity using anharmonic lattice dynamics calculations*. PhD thesis, Carnegie Mellon University, Pittsburgh, PA, 2009. 9, 48, 51, 52, 55, 119
- [112] J. A. Thomas, J. E. Turney, R. M. Iutzi, C. H. Amon, and A. J. H. McGaughey. Predicting phonon dispersion relations and lifetimes from the spectral energy density. *Physical*

Review B, 81:081411(R), 2010. 13, 15, 18, 20, 31, 32, 33, 120

- [113] D. G. Cahill, W. K. Ford, K. E. Goodson, G. D. Mahan, A. Majumdar, H. J. Maris, R. Merlin, and S. R. Phillpot. Nanoscale thermal transport. *Journal of Applied Physics*, 93:793818, 2003. 14
- [114] A. D. McConnell and K. E. Goodson. Thermal conduction in silicon micro and nanostructures. *Annual Review of Heat Transfer*, 14:129168, 2005. 14
- [115] M. Asheghi, Y. K. Leung, S. S. Wong, and K. E. Goodson. Phonon-boundary scattering in thin silicon layers. *Applied Physics Letters*, 71:17981800, 1997. 14
- [116] Alexander Balandin and Kang L. Wang. Significant decrease of the lattice thermal conductivity due to phonon confinement in a free-standing semiconductor quantum well. *Physical Review B*, 58(3):15441549, July 1998. 14
- [117] Zhitong Tian, Keivan Esfarjani, Junichiro Shiomi, Asegun S. Henry, and Gang Chen. On the importance of optical phonons to thermal conductivity in nanostructures. *Applied Physics Letters*, 99(5):053122, 2011. 14
- [118] A. I. Hochbaum, R. Chen, R. D. Delgado, W. Liang, E. C. Garnett, M. Najarian, A. Majumdar, and P. Yang. Enhanced thermoelectric performance of rough silicon nanowires. *Nature*, 451:163167, 2008. 14
- [119] P. Martin, Z. Aksamija, E. Pop, and U. Ravaioli. Impact of phonon-surface roughness scattering on thermal conductivity of thin si nanowires. *Physical Review Letters*, 102:125503, 2009. 14
- [120] Patrick E. Hopkins, Charles M. Reinke, Mehmet F. Su, Roy H. Olsson, Eric A. Shaner, Zayd C. Leseman, Justin R. Serrano, Leslie M. Phinney, and Ihab El-Kady. Reduction in the thermal conductivity of single crystalline silicon by phononic crystal patterning. *Nano Letters*, 11(1):107112, 2011. 14
- [121] E. S. Landry and A. J. H. McGaughey. Effect of film thickness on the thermal resistance

of confined semiconductor thin films. *Journal of Applied Physics*, 107:013521, 2010. xvi, 14, 81

- [130] N. W. Ashcroft and N. D. Mermin. *Solid State Physics*. Saunders, Fort Worth, 1976. 15, 19, 37, 44, 51, 74, 75, 123
- [131] F. H. Stillinger and T. A. Weber. Computer simulation of local order in condensed phases of silicon. *Physical Review B*, 31:52625271, 1985. xvi, 15, 29, 37, 52, 78, 83, 85, 102
- [132] D. W. Brenner, O. A. Shenderova, J. A. Harrison, S. J. Stuart, B. Ni, and S. B. Sinnott. A second-generation reactive empirical bond order (REBO) potential energy expression for hydrocarbons. *Journal of Physics: Condensed Matter*, 14:783802, 2002. 15, 31
- [133] W. Rudin. *Real and Complex Analysis*. McGraw-Hill, New York, 1987. 17, 118
- [134] J. D. Gale and A. L. Rohl. The general utility lattice program. *Molecular Simulation*, 29:291, 2003. 20, 23, 25, 30, 44, 45, 57, 80, 84, 86, 114
- [135] A. J. H. McGaughey and M. Kaviany. Phonon transport in molecular dynamics simulations: Formulation and thermal conductivity prediction. In G. A. Greene, Y. I. Cho, J. P. Hartnett, and A. Bar-Cohen, editors, *Advances in Heat Transfer, Volume 39*, page 169255. Elsevier, 2006. 20, 26, 45
- [136] Steve Plimpton. Fast parallel algorithms for short-range molecular dynamics. *Journal of Computational Physics*, 117(1):1–19, 1995. 23, 25, 29, 43, 78, 114
- [137] Paul F. Dubois, Konrad Hinsen, and James Hugunin. Numerical python. *Computers in Physics*, 10(3), June 1996. 23
- [138] J. A. Thomas. *water flow and thermal transport through carbon nanotubes*. PhD thesis, Carnegie Mellon University, Pittsburgh, PA, 2010. 24
- [139] B. Abeles, D. S. Beers, G. D. Cody, and J. P. Dismukes. Thermal conductivity of ge-si alloys at high temperatures. *Phys. Rev.*, 125(1):4446, January 1962. 36, 68
- [140] Hua Bao, Bo Qiu, Yu Zhang, and Xiulin Ruan. A first-principles molecular dynamics

approach for predicting optical phonon lifetimes and far-infrared reflectance of polar materials. *Journal of Quantitative Spectroscopy and Radiative Transfer*, 113(13):1683–1688, 2012. 37

- [141] W. A. Kamitakahara and B. N. Brockhouse. Vibrations of a mixed crystal: Neutron scattering from $\text{Ni}_{0.55}\text{Pd}_{0.45}$. *Phys. Rev. B*, 10(4):12001212, August 1974. 40, 41, 68
- [142] David G. Cahill and Fumiya Watanabe. Thermal conductivity of isotopically pure and ge-doped si epitaxial layers from \$300. *Phys. Rev. B*, 70(23):235322, December 2004. 40, 41, 68
- [143] David G. Cahill, Fumiya Watanabe, Angus Rockett, and Cronin B. Vining. Thermal conductivity of epitaxial layers of dilute SiGe alloys. *Phys. Rev. B*, 71(23):235202, June 2005. 40, 41, 68
- [144] I. Kudman. Thermoelectric properties of p-type PbTe-PbSe alloys. *Journal of Materials Science*, 7(9):10271029, 1972. 41
- [145] Yanzhong Pei, Xiaoya Shi, Aaron LaLonde, Heng Wang, Lidong Chen, and G. Jeffrey Snyder. Convergence of electronic bands for high performance bulk thermoelectrics. *Nature*, 473(7345):6669, May 2011. 41
- [146] Koichi Momma and Fujio Izumi. VESTA: a three-dimensional visualization system for electronic and structural analysis. *Journal of Applied Crystallography*, 41(3):653–658, June 2008. xiv, xvi, 42, 79
- [147] D. P. Sellan, J. E. Turney, A. J. H. McGaughey, and C. H. Amon. Cross-plane phonon transport in thin films. *Journal of Applied Physics*, 108:113524, 2010. 43, 64
- [148] A. M. Bouchard, R. Biswas, W. A. Kamitakahara, G. S. Grest, and C. M. Soukoulis.

Vibrational properties of amorphous silicon-germanium alloys and superlattices. *Phys. Rev. B*, 38(15):1049910506, November 1988. 44

- [149] John C. Duda, Timothy S. English, Donald A. Jordan, Pamela M. Norris, and William A. Soffa. Reducing thermal conductivity of binary alloys below the alloy limit via chemical ordering. *Journal of Physics: Condensed Matter*, 23(20):205401, 2011. 45, 84, 93, 107, 108, 110, 142
- [150] Qian-Jin Chu and Zhao-Qing Zhang. Effect of correlations on the localization properties of electrons and phonons in the long-wavelength limit. *Phys. Rev. B*, 39(10):71207131, April 1989. 45
- [151] Takuma Hori, Takuma Shiga, and Junichiro Shiomi. Phonon transport analysis of silicon germanium alloys using molecular dynamics simulations. *Journal of Applied Physics*, 113(20):203514, 2013. 45, 50, 84, 88, 93, 107, 108, 110, 142, 144
- [152] Y. M. Beltukov, V. I. Kozub, and D. A. Parshin. Ioffe-regel criterion and diffusion of vibrations in random lattices. *Phys. Rev. B*, 87(13):134203, April 2013. 45, 47, 59, 68, 82, 83, 92, 107, 121, 142
- [153] Sebastian G. Volz and Gang Chen. Molecular-dynamics simulation of thermal conductivity of silicon crystals. *Phys. Rev. B*, 61(4):26512656, January 2000. 47, 82, 107, 121, 142
- [154] N. L. Green, D. Kaya, C. E. Maloney, and M. F. Islam. Density invariant vibrational modes in disordered colloidal crystals. *Physical Review E*, 83(5):051404, May 2011. 47, 82, 142
- [155] J. M. Larkin, J. E. Turney, A. D. Massicotte, C. H. Amon, and A. J. H. McGaughey. Comparison and evaluation of spectral energy methods for predicting phonon properties. *to appear in Journal of Computational and Theoretical Nanoscience*, 2012. 48, 50, 75, 88, 96

- [156] D. J. Ecsedy and P. G. Klemens. Thermal resistivity of dielectric crystals due to four-phonon processes and optical modes. *Phys. Rev. B*, 15(12):59575962, June 1977. 52, 55
- [157] Sergei Shenogin, Arun Bodapati, Paweł Keblinski, and Alan J. H. McGaughey. Predicting the thermal conductivity of inorganic and polymeric glasses: The role of anharmonicity. *Journal of Applied Physics*, 105(3):034906, 2009. 58, 96, 106
- [158] Ning Xu, Vincenzo Vitelli, Matthieu Wyart, Andrea J. Liu, and Sidney R. Nagel. Energy transport in jammed sphere packings. *Phys. Rev. Lett.*, 102(3):038001, January 2009. 58, 59, 68, 76, 92
- [159] Laurent Chaput, Atsushi Togo, Isao Tanaka, and Gilles Hug. Phonon-phonon interactions in transition metals. *Phys. Rev. B*, 84(9):094302, September 2011. 64
- [160] Ramez Cheaito, John C. Duda, Thomas E. Beechem, Khalid Hattar, Jon F. Ihlefeld, Douglas L. Medlin, Mark A. Rodriguez, Michael J. Campion, Edward S. Piekos, and Patrick E. Hopkins. Experimental investigation of size effects on the thermal conductivity of silicon-germanium alloy thin films. *Phys. Rev. Lett.*, 109(19):195901, November 2012. 68
- [161] David M. Leitner. Vibrational energy transfer and heat conduction in a one-dimensional glass. *Physical Review B*, 64(9):094201, August 2001. 72
- [162] Yee Kan Koh and David G. Cahill. Frequency dependence of the thermal conductivity of semiconductor alloys. *Phys. Rev. B*, 76(7):075207, August 2007. 72, 99, 103
- [163] C. Dames and G. Chen. Thermal conductivity of nanostructured thermoelectric materials. In D. M. Rowe, editor, *Thermoelectrics Handbook: Macro to Nano*, pages 421–42–11. Taylor & Francis, 2005. 72, 99
- [164] A. J. Minnich, J. A. Johnson, A. J. Schmidt, K. Esfarjani, M. S. Dresselhaus, K. A. Nelson, and G. Chen. Thermal conductivity spectroscopy technique to measure phonon mean free paths. *Phys. Rev. Lett.*, 107(9):095901, August 2011. 72, 103

- [165] Fan Yang and Chris Dames. Mean free path spectra as a tool to understand thermal conductivity in bulk and nanostructures. *Physical Review B*, 87(3):035437, January 2013. 72, 99
- [166] A. D. Christianson, M. D. Lumsden, O. Delaire, M. B. Stone, D. L. Abernathy, M. A. McGuire, A. S. Sefat, R. Jin, B. C. Sales, D. Mandrus, E. D. Mun, P. C. Canfield, J. Y. Y. Lin, M. Lucas, M. Kresch, J. B. Keith, B. Fultz, E. A. Goremychkin, and R. J. McQueeney. Phonon density of states of $\mathrm{LaFeAsO}_{1-x}\mathrm{F}_x$. *Phys. Rev. Lett.*, 101(15):157004, October 2008. 73
- [167] C. J. Morath and H. J. Maris. Phonon attenuation in amorphous solids studied by picosecond ultrasonics. *Phys. Rev. B*, 54(1):203213, July 1996. 76
- [168] P. Benassi, M. Krisch, C. Masciovecchio, V. Mazzacurati, G. Monaco, G. Ruocco, F. Sette, and R. Verbeni. Evidence of high frequency propagating modes in vitreous silica. *Phys. Rev. Lett.*, 77(18):38353838, October 1996. 76, 82, 86, 87, 142
- [169] S. N. Taraskin and S. R. Elliott. Propagation of plane-wave vibrational excitations in disordered systems. *Phys. Rev. B*, 61(18):1201712030, May 2000. 76, 82, 107, 121, 142
- [170] W. Götze and M. R. Mayr. Evolution of vibrational excitations in glassy systems. *Phys. Rev. E*, 61(1):587606, January 2000. 76, 82, 107, 142
- [171] G. Ruocco, F. Sette, R. Di Leonardo, G. Monaco, M. Sampoli, T. Scopigno, and G. Viliani. Relaxation processes in harmonic glasses? *Phys. Rev. Lett.*, 84(25):57885791, June 2000. 76, 82, 113, 142
- [172] Giancarlo Ruocco and Francesco Sette. High-frequency vibrational dynamics in glasses. *Journal of Physics: Condensed Matter*, 13(41):9141, 2001. 76, 82, 83, 86, 87, 142
- [173] J. Horbach, W. Kob, and K. Binder. High frequency sound and the boson peak in amorphous silica. *The European Physical Journal B - Condensed Matter and Complex Systems*, 19(4):531–543, 2001. 76, 82, 83, 86, 107, 114, 121, 142

- [174] A. Matic, D. Engberg, C. Masciovecchio, and L. Brjesson. Sound wave scattering in network glasses. *Phys. Rev. Lett.*, 86(17):38033806, April 2001. 76
- [175] J. L. Feldman. Calculations of the generalized dynamic structure factor for amorphous silicon. *Journal of Non-Crystalline Solids*, 307310(0):128 – 134, 2002. 76, 82, 83, 86, 107, 121, 142
- [176] B. Ruffl, M. Foret, E. Courtens, R. Vacher, and G. Monaco. Observation of the onset of strong scattering on high frequency acoustic phonons in densified silica glass. *Phys. Rev. Lett.*, 90(9):095502, March 2003. 76
- [177] J. K. Christie, S. N. Taraskin, and S. R. Elliott. Vibrational behavior of a realistic amorphous-silicon model. *Journal of Non-Crystalline Solids*, 353(2223):2272 – 2279, 2007. 76, 82, 86, 107, 121, 142
- [178] Hiroshi Shintani and Hajime Tanaka. Universal link between the boson peak and transverse phonons in glass. *Nat Mater*, 7(11):870–877, November 2008. 76, 82, 107, 121, 142
- [179] Carl Ganter and Walter Schirmacher. Rayleigh scattering, long-time tails, and the harmonic spectrum of topologically disordered systems. *Phys. Rev. B*, 82(9):094205, September 2010. 76
- [180] M. Wyart. Scaling of phononic transport with connectivity in amorphous solids. *EPL (Europhysics Letters)*, 89(6):64001, 2010. 76, 82, 107, 121, 142
- [181] S. Ayrinhac, M. Foret, A. Devos, B. Ruffl, E. Courtens, and R. Vacher. Subterahertz hypersound attenuation in silica glass studied via picosecond acoustics. *Phys. Rev. B*, 83(1):014204, January 2011. 76
- [182] B. W. H. van Beest, G. J. Kramer, and R. A. van Santen. Force fields for silicas and aluminophosphates based on ab initio calculations. *Physical Review Letters*, 64(16):19551958, April 1990. 77, 83, 102

- [183] G. J. Kramer, N. P. Farragher, B. W. H. van Beest, and R. A. van Santen. Interatomic force fields for silicas, aluminophosphates, and zeolites: Derivation based on ab initio calculations. *Physical Review B*, 43(6):50685080, February 1991. 77, 83, 102
- [184] Yves Guissani and Bertrand Guillot. A numerical investigation of the liquidvapor coexistence curve of silica. *The Journal of Chemical Physics*, 104(19):7633–7644, 1996. 77, 83, 102
- [185] D. Wolf, P. Kebinski, S. R. Phillpot, and J. Eggebrecht. Exact method for the simulation of coulombic systems by spherically truncated, pairwise r⁻¹ summation. *The Journal of Chemical Physics*, 110(17):8254–8282, 1999. 78
- [186] G. T. Barkema and Normandousseau. High-quality continuous random networks. *Phys. Rev. B*, 62(8):49854990, August 2000. 78, 83, 86, 102
- [187] U. Buchenau, H. M. Zhou, N. Nucker, K. S. Gilroy, and W. A. Phillips. Structural relaxation in vitreous silica. *Phys. Rev. Lett.*, 60(13):13181321, March 1988. 78, 132
- [188] Murat Durandurdu and D. A. Drabold. *Ab initio* simulation of pressure-induced low-energy excitations in amorphous silicon. *Phys. Rev. B*, 66(15):155205, October 2002. 78, 132
- [189] N. Bernstein, J. L. Feldman, and M. Fornari. Structural model of amorphous silicon annealed with tight binding. *Phys. Rev. B*, 74(20):205202, November 2006. 78, 132
- [190] Jie Chen, Gang Zhang, and Baowen Li. How to improve the accuracy of equilibrium molecular dynamics for computation of thermal conductivity? *Physics Letters A*, 374(23):23922396, May 2010. 79
- [191] B. Ruzicka, T. Scopigno, S. Caponi, A. Fontana, O. Pilla, P. Giura, G. Monaco, E. Pontecorvo, G. Ruocco, and F. Sette. Evidence of anomalous dispersion of the generalized sound velocity in glasses. *Phys. Rev. B*, 69(10):100201, March 2004. 82, 83, 86, 87, 142
- [192] D. Kaya, N. L. Green, C. E. Maloney, and M. F. Islam. Normal modes and density of

states of disordered colloidal solids. *Science*, 329(5992):656–658, 2010. 82, 142

- [193] R. Biswas, A. M. Bouchard, W. A. Kamitakahara, G. S. Grest, and C. M. Soukoulis. Vibrational localization in amorphous silicon. *Phys. Rev. Lett.*, 60(22):22802283, May 1988. 82, 83, 84, 102, 107, 121, 142
- [194] Victor Martin-Mayor, Marc Mezard, Giorgio Parisi, and Paolo Verrocchio. The dynamical structure factor in topologically disordered systems. *The Journal of Chemical Physics*, 114(18):8068–8081, 2001. 82, 107, 121, 142
- [195] S. Ciliberti, T. S. Grigera, V. Martin-Mayor, G. Parisi, and P. Verrocchio. Brillouin and boson peaks in glasses from vector euclidean random matrix theory. *The Journal of Chemical Physics*, 119(16):8577–8591, 2003. 82, 107, 121, 142
- [196] Jason M. Larkin and Alan J. H. McGaughey. Predicting alloy vibrational mode properties using lattice dynamics calculations, molecular dynamics simulations, and the virtual crystal approximation. *Journal of Applied Physics*, 114(2):023507, 2013. 82, 88, 89, 92, 107, 121, 142
- [197] Alessia Marruzzo, Walter Schirmacher, Andrea Fratalocchi, and Giancarlo Ruocco. Heterogeneous shear elasticity of glasses: the origin of the boson peak. *Sci. Rep.*, 3, March 2013. 82, 107, 121, 142
- [198] J.S. Cowpe, J.S. Astin, R.D. Pilkington, and A.E. Hill. Temporally resolved laser induced plasma diagnostics of single crystal silicon effects of ambient pressure. *A collection of papers presented at the Euro Mediterranean Symposium on Laser Induced Breakdown Spectroscopy (EMSLIBS 2007)*, 63(10):1066–1071, October 2008. 83
- [199] Ralph Walter Graystone Wyckoff and RWG Wyckoff. *Crystal structures*, volume 1. Interscience publishers New York, 1963. xvi, 83, 85
- [200] R. Vacher, J. Pelous, F. Plicque, and A. Zarembowitch. Ultrasonic and brillouin scattering study of the elastic properties of vitreous silica between 10 and 300 k. *Journal of Non-*

Crystalline Solids, 45(3):397–410, September 1981. 86, 87

- [201] A. Polian, Dung Vo-Thanh, and P. Richet. Elastic properties of a-SiO₂ up to 2300 k from brillouin scattering measurements. *EPL (Europhysics Letters)*, 57(3):375, 2002. 86, 87
- [202] Mark D. Kluge and John R. Ray. Elastic constants and density of states of a molecular-dynamics model of amorphous silicon. *Phys. Rev. B*, 37(8):41324136, March 1988. 86
- [203] J. L. Feldman, J. Q. Broughton, and F. Wooten. Elastic properties of amorphous si and derived debye temperatures and grneisen parameters: Model calculation. *Phys. Rev. B*, 43(3):21522158, January 1991. 86
- [204] F Wooten, K Winer, D Weaire, et al. Computer generation of structural models of amorphous si and ge. *Physical review letters*, 54(13):13921395, 1985. 86
- [205] R. Vacher, H. Sussner, and M. Schmidt. Attenuation of surface phonons in opaque materials measured by brillouin scattering. *Solid State Communications*, 34(5):279 – 281, 1980. 87
- [206] V. Mazzacurati, G. Ruocco, and M. Sampoli. Low-frequency atomic motion in a model glass. *EPL (Europhysics Letters)*, 34(9):681, 1996. 89, 113
- [207] Jaroslav Fabian and Philip B. Allen. Anharmonic decay of vibrational states in amorphous silicon. *Phys. Rev. Lett.*, 77(18):38393842, October 1996. 89, 90, 110
- [208] P. Jund and R. Jullien. Molecular-dynamics calculation of the thermal conductivity of vitreous silica. *Physical Review B*, 59:1370713711, 1999. 96
- [209] K. T. Regner, S. Majumdar, and J. A. Malen. Instrumentation of broadband frequency domain thermoreflectance for measuring thermal conductivity accumulation functions. *Review of Scientific Instruments*, 84(6):064901, 2013. 103
- [210] G. S. Nolas, J. L. Cohn, and G. A. Slack. Effect of partial void filling on the lattice thermal conductivity of skutterudites. *Phys. Rev. B*, 58(1):164170, July 1998. 111

- [211] GS Nolas, DT Morelli, and Terry M Tritt. Skutterudites: A phonon-glass-electron crystal approach to advanced thermoelectric energy conversion applications. *Annual Review of Materials Science*, 29(1):89116, 1999. 111
- [212] Wee-Liat Ong, Sara M. Rupich, Dmitri V. Talapin, Alan J. H. McGaughey, and Jonathan A. Malen. Surface chemistry mediates thermal transport in three-dimensional nanocrystal arrays. *Nat Mater*, 12(5):410–415, May 2013. 111, 112
- [213] David G. Cahill, S. K. Watson, and R. O. Pohl. Lower limit to the thermal conductivity of disordered crystals. *Phys. Rev. B*, 46(10):61316140, September 1992. 111, 112
- [214] Tao He, Jiazhong Chen, H. David Rosenfeld, and M. A. Subramanian. Thermoelectric properties of indium-filled skutterudites. *Chemistry of Materials*, 18(3):759762, 2006. 111
- [215] et al. Yang. Effect of la filling on thermoelectric properties of $\text{La}_x\text{Co}_{3.6}\text{Ni}_{0.4}\text{Sb}_{12}$ -filled skutterudite prepared by MA-HP method. *Jo. of Sol. Stat. Chem.*, 179:212216, 2006. 111
- [216] Xiao-Jun Wang, Mei-Bo Tang, Jing-Tai Zhao, Hao-Hong Chen, and Xin-Xin Yang. Thermoelectric properties and electronic structure of zintl compound $\text{BaZn}[sub\ 2]\text{Sb}[sub\ 2]$. *Applied Physics Letters*, 90(23):232107, 2007. 111
- [217] JR Olson, KA Topp, and RO Pohl. Specific heat and thermal conductivity of solid fullerenes. In *Phonon Scattering in Condensed Matter VII*, page 4243. Springer, 1993. 111
- [218] O. Andersson, A. Soldatov, and B. Sundqvist. Thermal conductivity of C_{60} at pressures up to 1 GPa and temperatures in the 50–1300 K range. *Phys. Rev. B*, 54(5):30933100, August 1996. 112
- [219] Francesco Frigerio, Mose Casalegno, Chiara Carbonera, Tommaso Nicolini, Stefano Valdo Meille, and Guido Raos. Molecular dynamics simulations of the solvent- and thermal history-dependent structure of the PCBM fullerene derivative. *J. Mater. Chem.*,

22(12):5434–5443, 2012. 112

- [220] Mose Casalegno, Stefano Zanardi, Francesco Frigerio, Riccardo Po, Chiara Carbonera, Gianluigi Marra, Tommaso Nicolini, Guido Raos, and Stefano Valdo Meille. Solvent-free phenyl-c61-butyric acid methyl ester (PCBM) from clathrates: insights for organic photovoltaics from crystal structures and molecular dynamics. *Chemical Communications*, 2013. 112
- [221] G. Kresse and J. Hafner. Ab initio molecular dynamics for liquid-metals. *Physical Review B*, 47:558561, 1993. 112
- [222] W. L. Jorgensen. Transferable intermolecular potential functions for water, alcohols, and ethers. application to liquid water. *Journal of the American Chemical Society*, 103:335340, 1981. 112
- [223] W. L. Jorgensen, J. Chandrasekhar, J. Madura, R. W. Impey, and M. L. Klein. Comparison of simple potential functions for simulating liquid water. *Journal of Chemical Physics*, 79:926935, 1983. 112
- [224] William L. Jorgensen, David S. Maxwell, and Julian Tirado-Rives. Development and testing of the OPLS all-atom force field on conformational energetics and properties of organic liquids. *Journal of the American Chemical Society*, 118(45):11225–11236, 1996. 112
- [225] K. P. Jensen and W. L. Jorgensen. Halide, ammonium, and alkali metal ion parameters for modeling aqueous solutions. *Journal of Chemical Theory and Computation*, 2:14991509, 2006. 112
- [226] Victor Efimov and Leonid Mezhov-Deglin. Phonon-defect interaction in carbon samples of different allotrophic modifications. *physica status solidi (c)*, 1(11):2987–2990, November 2004. 112
- [227] Gene H Golub and Charles F Van Loan. *Matrix computations*, volume 3. JHU Press,

- [228] G. Baldi, V.M. Giordano, G. Monaco, and B. Ruta. High frequency acoustic attenuation of vitreous silica: New insight from inelastic x-ray scattering. *6th International Discussion Meeting on Relaxation in Complex Systems*, 357(2):538–541, January 2011. 114
- [229] Jean Pierre Boom and Sideney Yip. *Molecular Hydrodynamics*. DoverPublications. com, 1980. 114
- [230] J. E. Turney, A. J. H. McGaughey, and C. H. Amon. In-plane phonon transport in thin films. *Journal of Applied Physics*, 107(2):024317, 2010. 125
- [231] L.D. Landau, E.M. Lifshitz, and L.P. Pitaevskii. *Statistical Physics, Part 2 : Volume 9*. Pt 2. Elsevier Science & Technology Books, 1980. 130
- [232] A. Rajabpour and S. Volz. Thermal boundary resistance from mode energy relaxation times: Case study of argon-like crystals by molecular dynamics. *Journal of Applied Physics*, 108:094324, 2010. 130
- [233] L.D. Landau and G. Rumer. Absorption of sound in solids. *Phys. Z. Sowjetunion*, 11(18), 1937. 135
- [234] D. H. R. Price. Acoustic attenuation in II-VI compounds at microwave frequencies. *Journal of Physics C: Solid State Physics*, 4(9):966, 1971. 135